

# **On Improving The Oxidation Resistance Of A Nickel-Based Superalloy Produced By Powder Metallurgy**

by

Donald Clark Murray

Submitted in partial fulfilment of the requirements  
for the degree of Master of Applied Science

at

Dalhousie University  
Halifax, Nova Scotia  
August 2012

© Copyright by Donald Clark Murray, 2012

DALHOUSIE UNIVERSITY

DEPARTMENT OF PROCESS ENGINEERING AND APPLIED SCIENCE

The undersigned hereby certify that they have read and recommend to the Faculty of Graduate Studies for acceptance a thesis entitled “On Improving The Oxidation Resistance Of A Nickel-Based Superalloy Produced By Powder Metallurgy” by Donald Clark Murray in partial fulfilment of the requirements for the degree Master of Applied Science.

Dated: August 9, 2012

Co-Supervisors:

---

---

---

Reader:

---

DALHOUSIE UNIVERSITY

DATE: August 9, 2012

AUTHOR: Donald Clark Murray

TITLE: On Improving The Oxidation Resistance Of A Nickel-Based Superalloy  
Produced By Powder Metallurgy

DEPARTMENT OR SCHOOL: Department of Process Engineering and Applied  
Science

DEGREE: MAsc CONVOCATION: October YEAR: 2012

Permission is herewith granted to Dalhousie University to circulate and to have copied for non-commercial purposes, at its discretion, the above title upon the request of individuals or institutions. I understand that my thesis will be electronically available to the public.

The author reserves other publication rights, and neither the thesis nor extensive extracts from it may be printed or otherwise reproduced without the author's written permission.

The author attests that permission has been obtained for the use of any copyrighted material appearing in the thesis (other than the brief excerpts requiring only proper acknowledgement in scholarly writing), and that all such use is clearly acknowledged.

---

Signature of Author

## DEDICATION PAGE

I would like to dedicate this thesis to my family as they have supported me at every stage of my scholastic career.



# TABLE OF CONTENTS

LIST OF TABLES.....	viii
LIST OF FIGURES.....	ix
ABSTRACT.....	xiii
LIST OF ABBREVIATIONS USED .....	xiv
ACKNOWLEDGEMENTS.....	xv
CHAPTER 1 INTRODUCTION .....	1
1.1 Major Phases in Superalloys .....	1
1.2 Thermomechanical Aspects of Superalloys.....	2
1.2.1 Fatigue .....	3
1.2.2 Thermal Fatigue.....	3
1.2.3 Thermomechanical Fatigue.....	4
1.2.4 Creep .....	5
1.2.5 Coatings and TMF.....	6
1.2.6 Oxidation and TMF .....	7
1.2.7 TMF Testing.....	7
1.3 Powder Metallurgy of Superalloys .....	10
1.4 Laser Particle Size Analysis .....	12
1.5 Scanning Electron Microscopy (SEM).....	13
1.6 Differential Scanning Calorimetry (DSC).....	13
1.7 Consolidation and Sintering .....	14
1.7.1 Consolidation .....	14
1.7.2 Sintering.....	15
1.7.2.1 Solid State Sintering.....	16
1.8 Porosity Reduction.....	19
1.9 Oxidation Behaviour of Nickel-Based Superalloys.....	19
1.10 Reactive Element Additions .....	23
1.10.1 Silicon Additions.....	24
1.10.2 Yttrium Additions .....	25
1.11 Modeling via JMat Pro .....	26

CHAPTER 2	RESEARCH OBJECTIVES.....	28
CHAPTER 3	MATERIALS AND METHODS.....	29
3.1	Materials.....	29
3.2	Methods.....	29
3.2.1	Powder Characterization.....	29
3.2.2	Powder Processing.....	30
3.2.3	Delubrication.....	30
3.2.4	Thermodynamic Modelling.....	31
3.2.5	Differential Scanning Calorimetry (DSC).....	31
3.2.6	Sintering.....	31
3.2.7	Density Measurements.....	32
3.2.8	Electrical Discharge Machining (EDM).....	33
3.2.9	Thermo-mechanical Deformation.....	34
3.2.10	Heat Treatment.....	35
3.2.11	Oxidation.....	36
3.2.12	Microscopy.....	38
3.2.13	X-Ray Diffraction.....	38
3.2.14	Hardness Measurements.....	38
CHAPTER 4	RESULTS AND DISCUSSION.....	39
4.1	Materials.....	39
4.1.1	Microscopy.....	39
4.1.2	Particle Size Analysis.....	42
4.2	Blending and Compaction.....	44
4.3	Delubrication and Dimensional Change.....	45
4.4	Modeling Using JMatPro.....	46
4.5	Differential Scanning Calorimetry.....	53
4.6	Sintering.....	55
4.6.1	Hardness.....	55
4.6.2	Percent Theoretical Density (Porosity).....	56
4.6.3	Dimensional Change.....	57
4.6.4	Microstructure (as sintered).....	58

4.7	Porosity Reduction .....	59
4.8	Heat Treatment .....	61
4.8.1	Microstructure .....	62
4.8.2	Hardness Tests .....	64
4.9	X Ray Diffraction (XRD).....	65
4.10	Oxidation Testing .....	66
4.10.1	Weight Gain as a Function of Time.....	66
4.10.2	Microscopy of Oxidized Samples .....	68
4.10.3	X Ray Diffraction of Oxidized Samples.....	80
CHAPTER 5	ASSESSMENT OF FINDINGS .....	81
CHAPTER 6	SUMMARY AND CONCLUSIONS .....	85
REFERENCES	.....	86
APPENDIX A	.....	89
APPENDIX B	.....	104

## LIST OF TABLES

Table 1 – Semi-quantitative EDS results for the base ternary powder. ....	41
Table 2 - Dimensional changes for the TAY, TAS and TAYS samples from green body to de-lubricated. ....	45
Table 3 – Dimensional change from green to sintered state.....	57
Table 4 - Percent $\gamma'$ and precipitate size in the as sintered and post Gleebled and heat treated conditions. ....	64
Table 5 - EDS results for the spectrum collected. ....	69
Table 6 - Depth of oxide and PFZ for TA. ....	78
Table 7 – Depth of oxide and PFZ for TAY.....	78
Table 8 – Depth of oxide and PFZ for TAS.....	78
Table 9 – Depth of oxide and PFZ for TAYS.....	79

# LIST OF FIGURES

Figure 1 -Changes made in the microstructure of nickel based Superalloys from 1940 to 1970 [3].....	2
Figure 2 - Two types of fracture mechanisms. Low temperature fracture where fracture is not time or temperature dependant (top) and the mechanisms of creep that are active at above 0.3Tm (bottom) [5].....	6
Figure 3 - Gleeble test setup showing the sample under direct heating [9].....	8
Figure 4 - Graph of the TMF lives of aluminide coated Ni-based Superalloys in the polycrystalline, coarse grained directionally solidified, and single crystal states [6]...9	9
Figure 5 - A SEM micrograph of a pre-alloyed Ni-12Cr-9Fe powder.....	11
Figure 6 - An example of a vertical gas atomizer [16].....	12
Figure 7 - A schematic of the workings of a DSC where S is the sample crucible and R is the reference crucible [18].....	14
Figure 8 – Two sphere solid state sintering model [19].....	16
Figure 9 - Examples of surface and bulk transport mechanisms [16].....	17
Figure 10 - Stages of liquid phase sintering [19].....	18
Figure 11 - The oxidation behaviour for various compositions of the Ni-Al-Cr system oxidized at 1000°C. The different regions represent: (I) - External NiO , internal Cr <sub>2</sub> O <sub>3</sub> , Al <sub>2</sub> O <sub>3</sub> and spinels, (II) - External Cr <sub>2</sub> O <sub>3</sub> , internal Al <sub>2</sub> O <sub>3</sub> , (III) – External Al <sub>2</sub> O <sub>3</sub> [24].....	21
Figure 12- Oxidation stages and layers for a Ni-15Cr-6Al Superalloy at 1000 C for:.....	22
Figure 13 - Schematic representation weight change during isothermal and cyclic oxidation of CoCrAl+(Y or Hf) and NiCrAl+Zr vs. the amount of reactive element addition [25].....	24
Figure 14 - An SEM micrograph of yttria pegs at the oxide alloy interface after the metal substrate removed [36].....	26
Figure 15 - Sintering profile used for de-lubricated TRS bars.....	32
Figure 16 - Image of the traveling wire EDM used in the present research.....	33

Figure 17 – Image of wired sample in prepared for Gleeble Thermo-mechanical deformation.....	34
Figure 18 - Sample undergoing thermo-mechanical deformation.....	35
Figure 19 - Themomechanically deformed 1 cm sample that has been prepared for ageing.....	36
Figure 20 – Test setup with samples in glazed alumina crucibles prior to oxidation.....	37
Figure 21 - Test setup crucibles in stainless steel tray prior to oxidation.....	37
Figure 22 – An example of the faces tested during hardness testing.....	38
Figure 23 – Representative SEM micrograph of the base ternary powder.....	39
Figure 24 – SEM micrograph of the base ternary powder.....	40
Figure 25 - Standardless elemental mapping of the elements found in the base ternary powder.....	41
Figure 26 - The results of the laser particle size analysis.....	42
Figure 27 – Packing density of a mixture of powder sizes [11].....	43
Figure 28 – Plot of density (green and sintered) as a function of compaction pressure for ternary + 6w/oAl + 3w/oTi samples [29].....	44
Figure 29 - Dimensional change for TAY, TAS and TAYS using "new Al" from green body to delubricated.....	46
Figure 30 - Step Calculations for ternary-6Al alloy (TA).....	47
Figure 31 - JMatPro CCT diagram for the TA alloy.....	48
Figure 32 - Step temperature calculations for the TAS composition.....	49
Figure 33 - JMatPro model of liquation of TA between 1392°C and 1408°C.....	49
Figure 34 - JMatPro model of liquation of TAS between 1372°C and 1396°C.....	50
Figure 35 – JmatPro CCT diagram for the TAS alloy.....	51
Figure 36 - SEM micrographs of the TA sample (left) and TAT (right) [29].....	51

Figure 37 - JMatPro model of the CCT diagram for the TAT alloy.....	52
Figure 38 - DSC trace for TA on heating and cooling up to 1300°C (2.5°C/min).....	54
Figure 39 - DSC trace for TAS on heating and cooling up to 1300°C (2.5°C/min).....	54
Figure 40 - Hardness values for the alloys produced.....	55
Figure 41 – Density comparison of the alloys after sintering.....	56
Figure 42 - Dimensional change for TAY, TAS and TAYS from green body to sintered state.....	57
Figure 43 - TA (left) and TAS (right) in the as sintered condition.....	58
Figure 44 - TAY (left) and TAYS (right) in the as sintered condition.....	59
Figure 45 - Solutionizing treatment for wrought Ni-based Superalloys vs. vol% gamma prime [20].....	60
Figure 46 – Percent theoretical densities for all five compositions in the as sintered (left) and post (right) Gleeble deformed conditions.....	61
Figure 47 - An SEM-EDS mapping of the Ta foil still attached to a ternary sample after a Gleeble hot forge reduction of 30%.....	62
Figure 48 - TA (left) and TAS (right) in the Gleeble hot-deformed and heat-treated condition.....	63
Figure 49 - TAY (left) and TAYS (right) in the Gleeble hot-deformed and heat-treated condition.....	63
Figure 50 – XRD spectra for the TAYS sample in the sintered (S), Gleebled (G) and Gleeble + heat treated (G + HT) conditions.....	65
Figure 51 – Mass change vs. exposure time for all oxidized samples.....	66
Figure 52 – Mass change vs. exposure time for the first 48 hours.....	67
Figure 53 – Oxidation rates of the four alloys tested.....	68
Figure 54 - TAS oxidized for 48h showing various features on the oxidized sample.....	69
Figure 55 – Micrograph of TA after 1h oxidation.....	70
Figure 56 - Micrograph of TAS after 1h oxidation.....	71

Figure 57 - Micrograph of TA after 24h oxidation.....	72
Figure 58 - Micrograph of TAS after 24h oxidation.....	72
Figure 59 - Micrograph of TA after 48h oxidation.....	73
Figure 60 - Micrograph of TAS after 48h oxidation.....	74
Figure 61 - Micrograph of TA after 144h oxidation.....	75
Figure 62 - Micrograph of TAS after 144h oxidation.....	75
Figure 63 - Micrograph of TA after 432h oxidation.....	76
Figure 64 - Micrograph of TAS after 432h oxidation.....	77



## ABSTRACT

Nickel-based Superalloys are widely used in the steam turbine power generation and aerospace industries. They possess the desirable qualities of high-temperature strength, oxidation and corrosion resistance and can operate in some of the highest temperature ranges of the structural metals. The oxidation resistance of a Superalloy is achieved primarily through the formation of a dense alumina and/or chromia oxide layer(s) including spinels. This resistance has been further improved in wrought and cast alloys through the addition of reactive elements such as silicon, yttrium and lanthanum, although the exact effects of these elements have not been well defined.

This project concentrated on a powder metallurgy ternary master alloy consisting of Ni-12Cr-9Fe (w/o) with additions of 6w/o aluminum, 0.5w/o Si, and 0.1w/o Y, in various combinations. Specifically, the primary goal was to produce and characterize a PM manufactured nickel-based Superalloy with minor additions of reactive elements and to assess the effectiveness of the Si and/or Y in improving the oxidation resistance.

JMatPro modeling software was first used to help determine temperatures at which various events would occur in the alloys such as solutionizing and liquation temperatures. Subsequently green compacts were produced by a press (uni-axially) and sinter route to create transverse rupture strength bars (TRS bars). These bars were then thermomechanically deformed using a Gleeble tester to reduce porosity followed by a heat treatment to restore a microstructure better suited for high temperature oxidation. Sectioned TRS bars were then oxidized (static) 900°C in air for times up to 1000h and the influence of the Si/Y additions on oxidation resistance was determined via a combination of weight gain data and microstructural examination.

Whereas JMatPro predicted solutionizing temperature of the compositions studied (1010°C quaternary; 1020°C quaternary + Si, respectively) these values were slightly lower than the results observed through DSC experiments (1045°C quaternary; 1065°C quaternary + Si, respectively). A w/o  $\gamma'$  of approximately 25% was predicted by the modeling tool, but values of 58.3% to 61.7% were determined using a point count method. Finally, the addition of 0.5w/o Si to the quaternary Ni-Cr-Fe-Al PM system provided a measureable improvement in the oxidation resistance both in terms of thickness of oxide layer and in overall weight gain. Conversely, 0.1w/o Y provided little benefit, and was shown to be detrimental to alloys not containing Si.

## LIST OF ABBREVIATIONS USED

316SS	316 Stainless Steel
CGDS	Course Grained Directionally Solidified Alloy
CIP	Cold Isostatic Pressing
CTE	Coefficient of Thermal Expansion
DSC	Differential Scanning Calorimetry
E-C	Evaporation-Condensation
EDM	Electrical Discharge Machining
EDS	Energy Dispersive Spectroscopy
GBD	Grain Boundary Diffusion
HIP	Hot Isostatic Pressing
IF	Isothermal Fatigue
IP	In Phase (Thermomechanical Fatigue)
LCF	Low Cycle Fatigue
LCTF	Low Cycle Thermomechanical Fatigue
LPS	Liquid Phase Sintering
MIM	Metal Injection Moulding
NM	Not Measureable
OAL	Overall Length
OP	Out of Phase (Thermomechanical Fatigue)
P/M	Powder Metallurgy
PFZ	Precipitate Free Zone
SCDS	Single Crystal Directionally Solidified Alloy
SD	Surface Diffusion
SEM	Scanning Electron Microscopy
TBC	Thermal Barrier Coating
T, TERN	Ternary alloy (Ni-12Cr-9Fe)
TA	Ternary alloy + 6 w/o Al
TAS	Ternary alloy + 6 w/o Al + 0.5 w/o Si
TAY	Ternary alloy + 6 w/o Al + 0.1 w/o Y
TAYS	Ternary alloy + 6 w/o Al + 0.5 w/o Si + 0.1 w/o Y
T <sub>m</sub>	Melting Temperature
TMF	Thermomechanical Fatigue
TRS	Transverse Rupture Strength Bar
v/o	Volume Percent
VD	Volume Diffusion
w/o	Weight Percent
XRD	X-Ray Diffraction

## ACKNOWLEDGEMENTS

The author would like to thank Dr. W.F. Caley and Dr. N.L. Richards for their unwavering support throughout this project. Many thanks go to Dr. D.P. Bishop for the use of the powder metallurgy lab at Dalhousie University. Dr. S. Corbin and Dr. G.J. Kipouros for investing their time to critique this thesis. It was the financial support of Nancy Murray and Chris Petersson who helped make this thesis a possibility. Dan Chevalier (Dalhousie University), Mike Boskwick (University of Manitoba), Neil Ball (University of Manitoba) and Don Mardis (University of Manitoba) also deserve recognition for their technical assistance with sample preparation and examination. I would also like to thank my colleagues Eric Moreau, David Heard, Chris Boland, Mathew Smith and Emmanuel Abrokwah.

# CHAPTER 1 Introduction

Superalloys have become the material of choice for many high temperature strength and corrosion resistant applications. These include industrial gas turbines, steam turbines and aerospace applications. The three basic types of Superalloys are nickel based, iron-nickel based and cobalt based; these can be used at service temperatures above 540°C. These alloys gain their strength from solid-solution hardening, work hardening, and precipitation hardening. Nickel based Superalloys can be used at a higher fraction of their melting point than almost any other commercially available alloy. High temperature oxidation resistance is crucial in achieving long service lives of these materials and the influence of minor element additions on oxidation resistance is therefore important [1]. This thesis attempts to address the effects of silicon and yttrium, singly and together, on the oxidation resistance of such an alloy, in particular, a powder metallurgy counterpart of Inconel 600.

## 1.1 Major Phases in Superalloys

There are three major phases present in nickel-based Superalloys. Gamma ( $\gamma$ ) is the principal Ni-based FCC austenitic matrix with additions of solid solution elements such as Fe, Cr, W, Mo amongst others; Gamma prime ( $\gamma'$ ), the main precipitate phase, is of the form  $A_3B$  and is commonly  $Ni_3Al$  or  $Ni_3(Al,Ti)$  in these Superalloys; and carbides of the  $M_{23}C_6$  or MC varieties. There have been several advancements in nickel based Superalloys since the development of Nimonic 80 in 1941 [1]. Progress has been made with regards to four main areas in these alloys:

1. Gamma primes ( $\gamma'$ ) volume fraction has been increased.
2. The size of the  $\gamma'$  phase increased and eventually remained steady at around 1 $\mu$ m.
3.  $\gamma'$  appeared as a secondary smaller precipitate.
4.  $\gamma'$  morphology became more cubic

Though there is some strength gained from the solid-solution hardening of substitutional atoms within the austenitic FCC matrix, the main strengthening phase within these alloys

is the  $\gamma'$  precipitate which is coherent within the  $\gamma$  matrix [1] [2]. The basic progressions made from 1940 to 1970 within the microstructure of these alloys are shown in Figure 1.

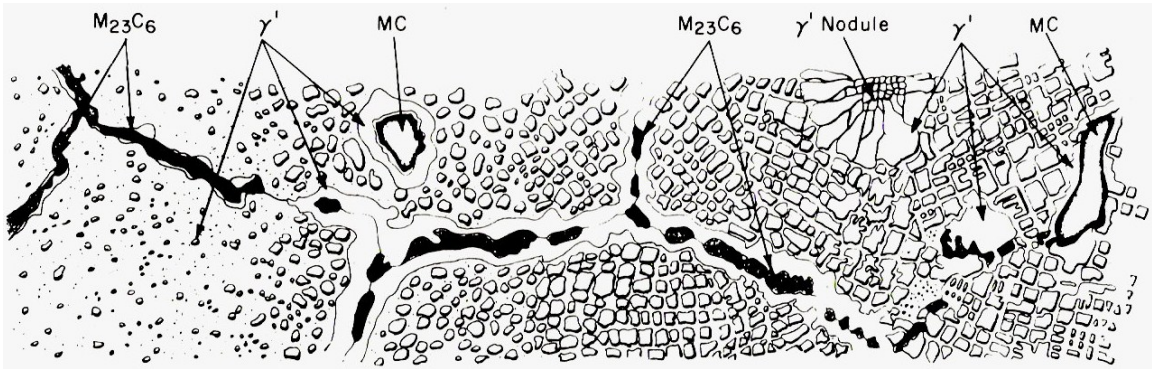


Figure 1 -Changes made in the microstructure of nickel based Superalloys from 1940 to 1970 [2].

The shape of the precipitate is determined by the lattice mismatch of the  $\gamma/\gamma'$  phases. With small mismatch (0.05% – 0.2%) the  $\gamma'$  phase appears as spheres. With increasing mismatch the  $\gamma'$  precipitates will appear in the cubic form up to 1.25% at which point they will precipitate as semi-coherent plates [2].

High temperature oxidation resistance is crucial in achieving long service lives of these materials. It has been proposed that the addition of minor reactive elements can improve the static and cyclic oxidation behaviour of these alloys. It is critical, however, that only small amounts of these reactive elements be added to these systems as they have also been found to form the deleterious phases (i.e. Laves,  $\mu$  or  $\sigma$ ) [1].

## 1.2 Thermomechanical Aspects of Superalloys

As outlined earlier, Superalloys are often used in the most demanding aerospace applications such as turbine blades in jet engines or power generation. These components in the hot working areas are subjected to not only mechanical stresses, but thermal stresses. If a material is subject to a thermal stress that is constant but the stress is varied it is said to be isothermal fatigue. If the thermo and mechanical fatigue are occurring concurrently it is deemed thermomechanical fatigue. This is a more realistic real world

situation and this can lead to more drastic and detrimental effects. This damage can reduce the life of such materials and ultimately lead to the need to replace certain hot section components or in the worst cases and not planned for or expected catastrophic failure [4].

When operating temperatures are in excess of 540°C ordinary stainless steels no longer retain their strength and will generally suffer from corrosion problems. At these temperatures and up until around 1000°C Superalloys are the material of choice, though they may be covered with a thermal barrier coating (i.e. MCrAlY) at these extreme temperatures to reduce corrosion/oxidation.

### **1.2.1 Fatigue**

Almost all Superalloys are subject to fatigue under normal operating conditions. Fatigue is a process whereby, through cyclically loading, the material gradually degrades and eventually fails even though the stress that it was under is far below yield strength and ultimate tensile strength. The fatigue life of a material is influenced by a variety of factors such as applied stress, temperature, surface roughness, microstructure, composition, residual stresses and environment. One of the most important factors in generating fatigue is the development of inelastic deformation. In elastic deformation of materials the strain in a material is recoverable as it remains below its yield stress limit and can recover, returning to its original length and relieving the stress. However if this elastic deformation is repeated several hundred, thousands or millions of times dislocations can form persistent slip bands that will eventually nucleate short cracks in the material [5]. In Superalloys fatigue is often mechanically induced, though it can also have a thermal component [4].

### **1.2.2 Thermal Fatigue**

Most structural alloys are subjected to thermal loading. Thermal cycling of this loading can create stresses within the material without the presence of external loading. This is generally termed thermal fatigue. This can be caused by a variety of factors on a component such as steep temperature gradients across the depth of a specimen, variations

in thermal expansion coefficients between a coating and its substrate or the various crystallographic orientations of grains within a material and their response to thermal loading. If one section (coating, grain orientation, depth) of a component undergoes thermal expansion yet the material beside (under) that section constrains the expansion or contraction of the strained material the surface can undergo compressive or tensile stresses. When a thermal component is present while the material is being cyclically loaded this can be referred to as thermomechanical fatigue (TMF). Thermal Fatigue testing results generally correlate well the TMF test results in terms of trends [6].

### **1.2.3 Thermomechanical Fatigue**

Both thermal and mechanical fatigue can play an important role in the lifespan of a structural material. Thermomechanical fatigue is the main life-limiting factor for many engineering components in various high-temperature applications [5]. This is especially true in the case of jet engine or aerospace components such as turbine blades [7]. These materials have one of the best combinations of high temperature strength and oxidation resistance, but failure is generally due to thermomechanical fatigue. Thermomechanical fatigue (TMF) occurs when there are simultaneous changes in temperature and mechanical strain.

Isothermal fatigue (IF) at high temperatures can be considered a special type of TMF. IF information will not help to predict what may happen during TMF, but would be useful if a structural component was heated to a consistent temperature but underwent various stresses [6].

Low cycle fatigue (LCF) describes how materials will fail or suffer after low cycle numbers which is common during TMF testing. A real world example of a low cycle thermomechanical fatigue (LCTF) would be the thermal gradients that develop in jet engines during start-up and shutdown. The total number of takeoffs and landing for a typical jet aircraft is less than 30,000 cycles over its lifetime; therefore, LCTF experiments are logical and can be completed in a reasonable amount of time [6].

During TMF there are several microstructural changes that can take place:

- a) coarsening of the precipitates or lamellae, b) there is strain ageing for solute-hardened systems, c) precipitation of a secondary particle or phase, d) phase transformation, e) oxidation/corrosion.

These mechanisms will influence the degradation of the material and ultimately help determine TMF behaviour [6].

Within TMF come the mechanisms of not only fatigue but high temperature creep and oxidation.

#### **1.2.4 Creep**

Creep strength (rupture strength) is a time dependent deformation of a material where it slowly deforms under the influence of stresses. It is more severe in materials that are subjected to heat for long periods and will increase with increasing temperatures. Three important events occur during creep that contribute to final fracture. As a material is elongated or compressed, its cross sectional area is gradually decreased or increased and the stress that is placed on this thinner cross-sectional area is gradually increased. Secondly, as a material is deformed it may undergo recrystallization or precipitates may form. The third event is that internal flaws develop and lead to high internal stress concentrations. These stress concentrations coagulate and combined with the reduced cross sectional area the material can no longer carry the load and fracture will occur. The mode of fracture will depend on if a material is strained at low temperatures (i.e. below  $0.3T_m$  in absolute temperature scale) or above  $0.3T_m$ . The two types ( $>0.3T_m$  and  $<0.3T_m$ ) are shown schematically in Figure 2 [5].



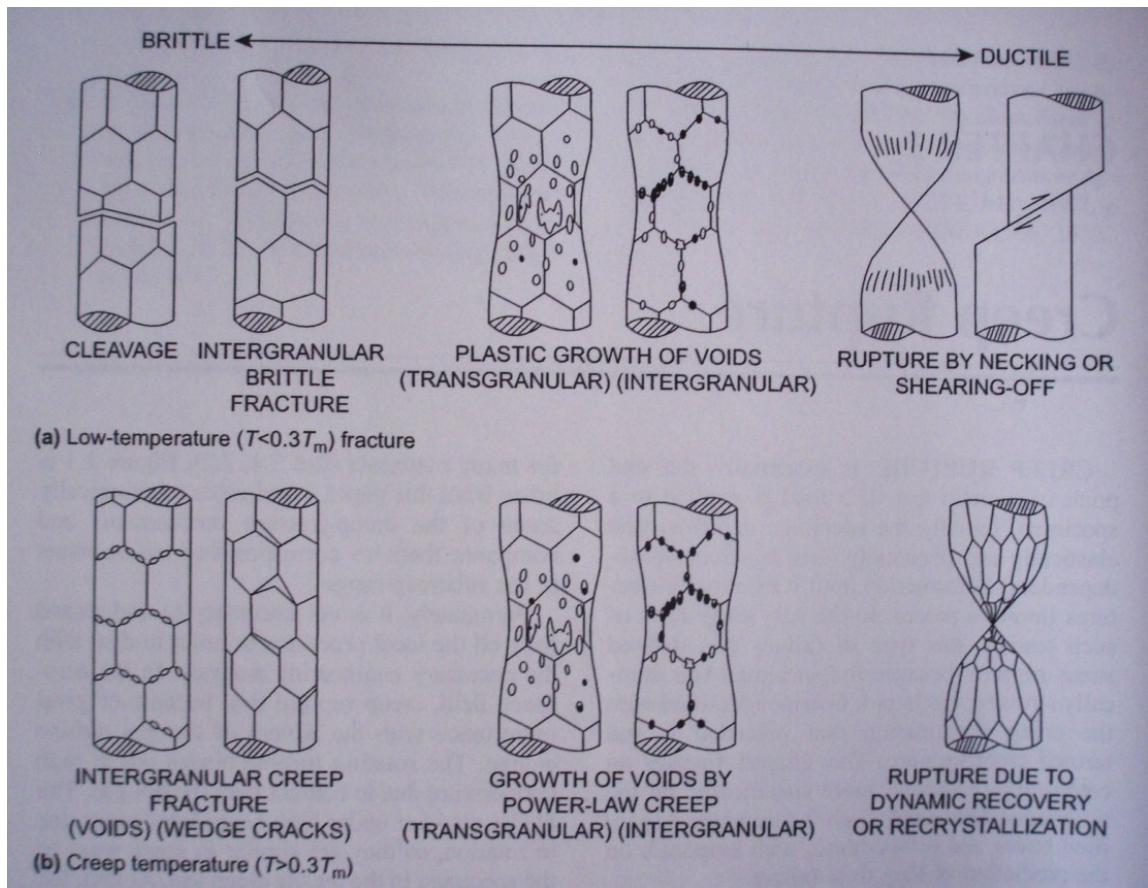


Figure 2 - Two types of fracture mechanisms. Low temperature fracture where fracture is not time or temperature dependant (top) and the mechanisms of creep that are active at above  $0.3T_m$  (bottom) [5].

### 1.2.5 Coatings and TMF

The environmental effects of corrosion on Superalloys can be reduced or prevented by the use of protective coatings. There are three primary types of protective coatings on Superalloys and they are: a) diffusion coatings b) overlay coatings and c) thermal barrier coatings (TBC). In the overlay coatings the M generally stands for nickel or cobalt. The protective alumina layer that is formed is the dominant oxide formed within all of these protective coatings, however there are also spinels that will form (i.e.  $Ni(Al,Cr)_2O_4$ ). Alumina has a very low thermal expansion coefficient compared to the underlying Superalloy substrate. When these two are heated a large thermal mismatch strain between the two encourages cracks to form within the coating as the coating cannot expand at the same rate as the substrate. This can lead to spallation of the protective oxide layer which

can be considered failure of coating and can lead to oxidation or degradation of the substrate [1]. It is therefore crucial to test the material in the environment that it will be operational in to understand how the coating and substrate will respond under these conditions.

### **1.2.6 Oxidation and TMF**

If oxygen is present in the service environment of a nickel based Superalloy, it will have a surface oxide layer. Oxidation is more rapid at higher temperatures due to increased diffusion rates and therefore the effect will be more rapid and generally oxidize to a greater depth. There are several mechanisms that have been proposed including: brittle fracture of the oxide scale resulting in enhanced crack nucleation and growth, grain-boundary oxidation resulting in intergranular cracking among others. The out of phase (OP) TMF damage (defined in 1.2.7) is greatly increased when the rate of oxide layer fracture is greater than creep damage. The oxidation damage of a material at higher temperatures will be increased with increased mismatch between the thermal expansion coefficient of the substrate and the oxide layer that develops [6]. A summary of various oxide and oxide-fatigue damage mechanisms and models and laws have been published by the ASM [6]. The majority of oxidation models state that failure of the oxide layer is due to growth stresses or changes in temperature; however the effect of mechanical strain on oxidation behaviour has not been well defined [5].

### **1.2.7 TMF Testing**

In thermomechanical fatigue experiments both the temperature and strain rate imparted on a test piece are tightly controlled. The phasing between both temperature and strain can be varied and there are two principal types, out of phase (OP) and in phase (IP). Out of phase means that the material is strained at a maximum strain at a minimum temperature where in phase is maximum strain at maximum temperature [8]. Out of phase TMF is generally considered to be the most damaging to a material due to the fact the thermal expansion of the alloy and/or coating is lower at lower temperatures leading to increased crack propagation.

Oddly the influence of creep on OP TMF life is mainly determined by IP testing experiments. This is due to the fact that the influence of creep is much greater at higher temperatures.

One type of TMF test that can be performed on a material is a Gleeble test. This type of test involves heating a sample through highly thermally conductive grips (direct resistance heating) and heating the sample at tremendously high heating rates (up to 10,000°C/min) while simultaneously putting a sample in compression or tension. This technique is limited as the sample must be conductive unless a modification is made to include a conductive sample holder [6]. An example of a test setup for Gleeble testing is shown in Figure 3.

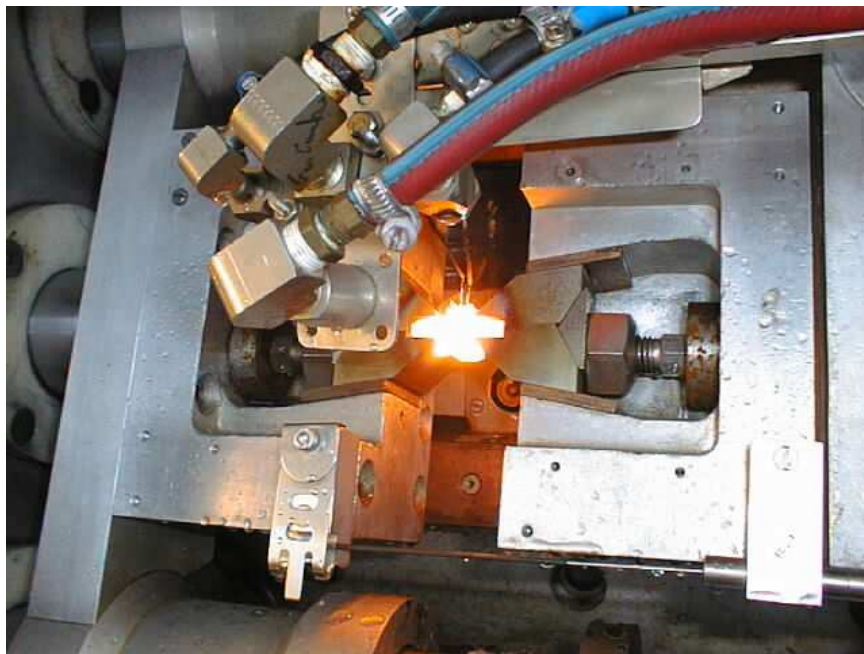


Figure 3 - Gleeble test setup showing the sample under direct heating [9].

Directionally solidified Superalloys alloys have been shown to have improved creep strength with limited amounts of carbides or borides present on grain boundaries which restrict grain boundary movement. Polycrystalline cast alloys have been shown to have the lowest TMF resistance when compared with SCDS and CGDS alloys. The results for TMF testing on a cast Ni-based Superalloy are shown in Figure 4.

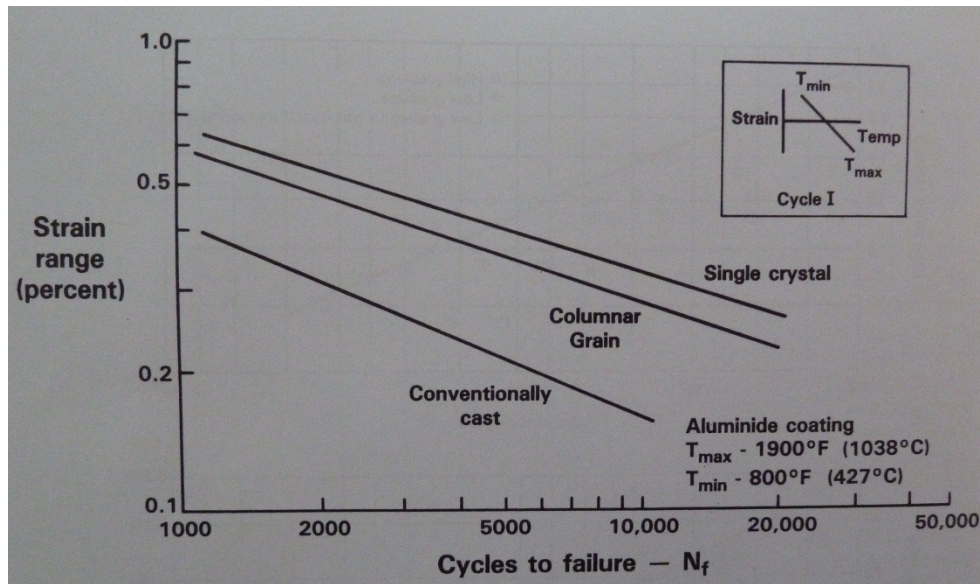


Figure 4 - Graph of the TMF lives of aluminide coated Ni-based Superalloys in the polycrystalline, coarse grained directionally solidified, and single crystal states [6].

Nickel based Superalloys which are produced through powder metallurgy processing routes can have a more homogenous distribution of secondary phases and precipitates when compared to polycrystalline cast alloys, and offer tighter compositional control. There are a few drawbacks to producing Superalloys by some of the powder metallurgy production techniques (cold isostatic compaction or uniaxial die compaction) when referring to TMF and they are porosity and fine grain size. The porosity within powder metallurgy alloys has a detrimental impact on the physical properties of the material and can increase the oxidation rate and depth of the alloy. This is especially true if the porosity is interconnected as the effect of the mismatch between the oxide layer and the substrate will be more pronounced. The fine grain size is generally considered an advantage in terms of strengthening behaviour. However, during TMF testing it has been stated that grain boundaries can be initiation sites for crack propagation or preferential oxidation [6].

If the production method involves hot isostatic pressing nickel-based Superalloys can have an extremely high final density. This higher density can increase the TMF behaviour of the component and lead to a lower compositional gradient within the material than

would be produced by a cast nickel-based Superalloy. This reduced compositional gradient would most likely increase the TMF life and give more homogenous physical properties to the material.

### **1.3 Powder Metallurgy of Superalloys**

Powder metallurgy (P/M) is a process in which powders are processed into compacts and sintered into useable components for various applications. This process (P/M) has evolved to be of prime importance in the manufacturing of a large number of engineering components, usually ferrous but more recently aluminum, magnesium and nickel-based [10], [11]. In addition, P/M products can exhibit a relatively longer component life expectancy when compared to some cast materials. It has even been suggested that P/M processing of some alloys (e.g., a Superalloy) in the 100% dense condition may improve corrosion resistance of the materials in selected applications [12]. Of all its advantages, improved toughness, machinability, controlled grain size and more uniform heat treatment response are most significant [13]. Additionally, the use of P/M processing can also help to control the amount of alloying elements required or intermetallic phases that form which could be difficult to achieve through traditional casting routes [14].

Production of these materials through a powder metallurgy route offers distinct advantages over wrought or cast products. These include a greater morphological control, decrease in macro-segregation, tighter compositional control, a near-net shape product and a higher degree of compositional homogeneity (vs. cast or wrought products) [15].

For nickel based Superalloys, P/M production offers the advantage of a homogeneous, fine-grained microstructure that can be more highly alloyed when compared to conventional processing techniques. The lower amount of raw materials and lower machining required is another advantage to the production of Superalloys through powder metallurgy.

The main drawback with this technique is the inherent cost of the raw materials and that the processing machinery for production can be expensive. The raw material used in the majority of P/M Superalloys is a pre-alloyed powder with each particle acting as a mini-



ingot with the matching composition as the molten alloy [1]. A typical example of a pre-alloyed powder as used in this thesis is shown in Figure 5.

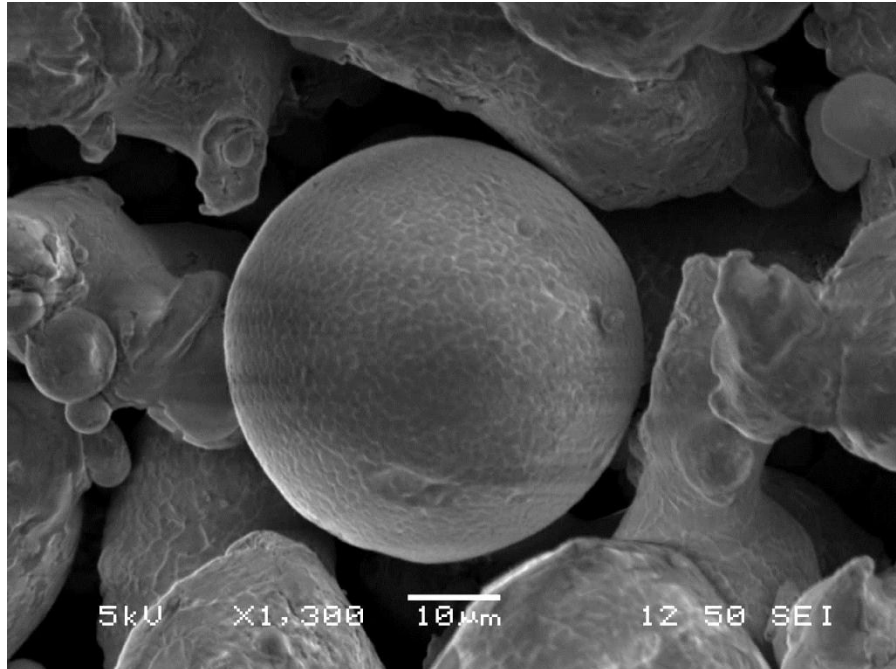


Figure 5 - A SEM micrograph of a pre-alloyed Ni-12Cr-9Fe powder.

The production route most commonly chosen for pre-alloyed Superalloy powders is inert gas atomization. This will often produce powders of a spherical shape, with a low degree of contamination. Gas atomization involves directing a pressurized gas (air, N<sub>2</sub>, He, Ar) through nozzles that break up the liquid stream of molten metal shown in Figure 6.

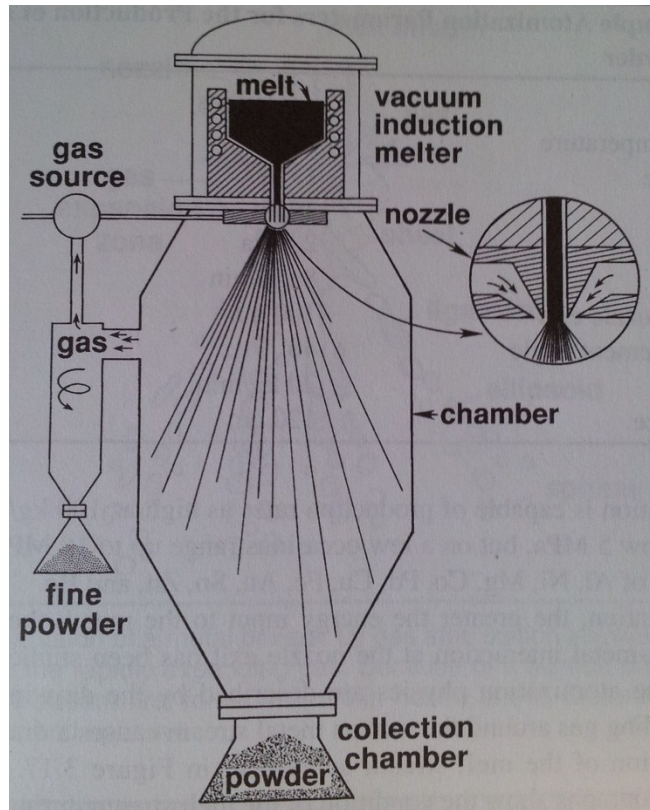


Figure 6 - An example of a vertical gas atomizer [16].

If an inert gas is used the particle shape is frequently spherical with a large size distribution. Often, satellites will occur on the sides of the spherical particles that have not been trapped in the fine powder collection chamber. Depending on a number of variables including the gas used, orientation of the system and the amount of superheat of the melt various shapes, size distributions and morphologies will be observed. There is a generic sequence of particles which are created through vertical gas atomization which is in the order: a cone of liquid, plates, ligaments, rounded particles then spheres.

## 1.4 Laser Particle Size Analysis

With all powder metallurgy processing a minimum quantitative and qualitative characterization battery is critical in order to ensure repeatability in the research environment and to provide a standardized product on an industrial scale. One place to begin this type of characterization is with a quantitative analysis using a laser particle size analysis. In laser particle size analysis a representative sample is dispersed in a fluid and

drawn into a sample cell where a laser beam is scattered by the particle. The photo detector at the end of the device then measures the angle and intensity at which the beam was scattered and converts this into a measure of a particles size [16]. This method is very fast, provides a complete particle size distribution and measurements can be continuously conducted. The main limitation of this technique is that assumes that all particles are spherical.

## **1.5 Scanning Electron Microscopy (SEM)**

A scanning electron microscope (SEM) is one of the preferred techniques for qualitative analysis of powdered materials. The SEM has several advantages over other forms of characterization in that it has a large field of view in order to view topography of the powder, while giving particle chemistry through Energy Dispersive Spectroscopy (EDS). An SEM produces a beam of electrons through an electron gun and directs this beam at the sample. There are detectors within the SEM that collect the electrons which are ejected from the sample and convert them into an image. The use of an SEM also provides the ability to show how particle shape relates to particle characteristics [16] [17].

## **1.6 Differential Scanning Calorimetry (DSC)**

The process of differential scanning calorimetry involves heating or cooling a sample + reference at the same rate and measuring the difference in energy input required to maintain the two materials at nearly the same temperature. The difference in energy that is required to hold both materials at an identical temperature is given by heat changes in the sample. If an extra energy input is required to hold both materials at the same temperature, it is measured between the sample and the reference material. A schematic of the workings of a DSC is shown in Figure 7.



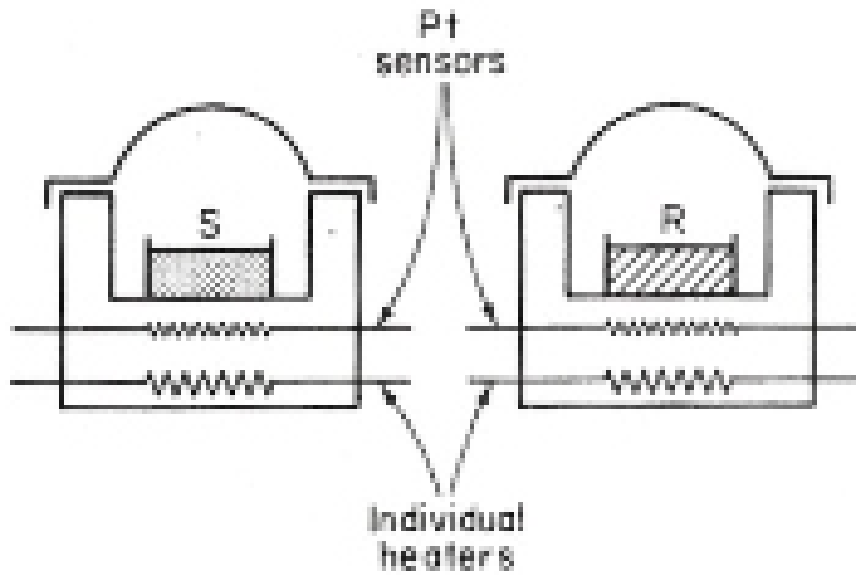


Figure 7 - A schematic of the workings of a DSC where S is the sample crucible and R is the reference crucible [18].

This is a very useful technique when trying to determine phase changes within a material and within nickel based Superalloys, determining the onset of the various intermetallics.

## 1.7 Consolidation and Sintering

In order to obtain a P/M compact having reasonable mechanical integrity and predictable dimensional attributes a process that includes powder characterization, blending, pressing to form a green body and sintering to final density is required.

### 1.7.1 Consolidation

Powder consolidation can be achieved through various processes such as metal injection molding (MIM), hot or cold iso-static pressing (HIP, CIP) and die compaction. Uniaxial powder die compaction is the predominant means of powder compaction as it offers high production rates, good dimensional tolerance, and lower maintenance relative to other forms of powder compaction such as CIP [11].

In uniaxial die compaction powders are poured into a die and compressed linearly. Powder compaction is a critical step in P/M, in which metal powder particles are consolidated together through applied pressure, into a brittle, porous fragile solid termed a green body.

The compaction process is one of key importance in the powder metallurgy process. Properties such as green density and green strength are highly dependent on compaction pressure used, and will help determine the properties of the sintered component. Powder size, morphology and chemistry along with the additions of lubricants and binders will also have an effect on green strength and density. Particle packing through interlocking (particle shape) and plastic deformation (particle chemistry) affect the ability of particles to pack more efficiently. The lubricants are used to minimize die wall friction, decrease density gradients in the green body and facilitate ejection [16].

One method to optimize the pressure employed during compaction is via compressibility curves. Here a standard weight of the powders of interest is blended with a suitable lubricant and uni-axially pressed over a range of pressures, typically 100-600MPa. The per cent porosity, measured as per cent of theoretical density as determined using the Rule of Mixtures, may then be plotted as a function of applied pressure to yield the optimum pressure for preparing a given green body prior to sintering.

### **1.7.2 Sintering**

There are various types of sintering for powder metallurgy products. The sintering of loosely consolidated powders produced through compaction imparts strength, and should ultimately yield a component that has much greater mechanical properties than the green body. Some examples of sintering types are solid-state, mixed phase, activated transient liquid phase and persistent liquid phase [11].

There are several different ways to measure the sintering response of an alloy. These include density increase from green to the sintered state, shrinkage and swelling (dimensional change), and the increase in mechanical strength.

### 1.7.2.1 Solid State Sintering

Solid state sintering is a process whereby two adjacent powder particles come together and form a neck. There is a reduction in surface energy for the individual powder particles when this occurs which reduces the overall free energy in the system. Solid state sintering is always done below the solidus temperature of the alloy system. A two sphere model is a good way to represent what occurs during solid state sintering as shown in Figure 8.

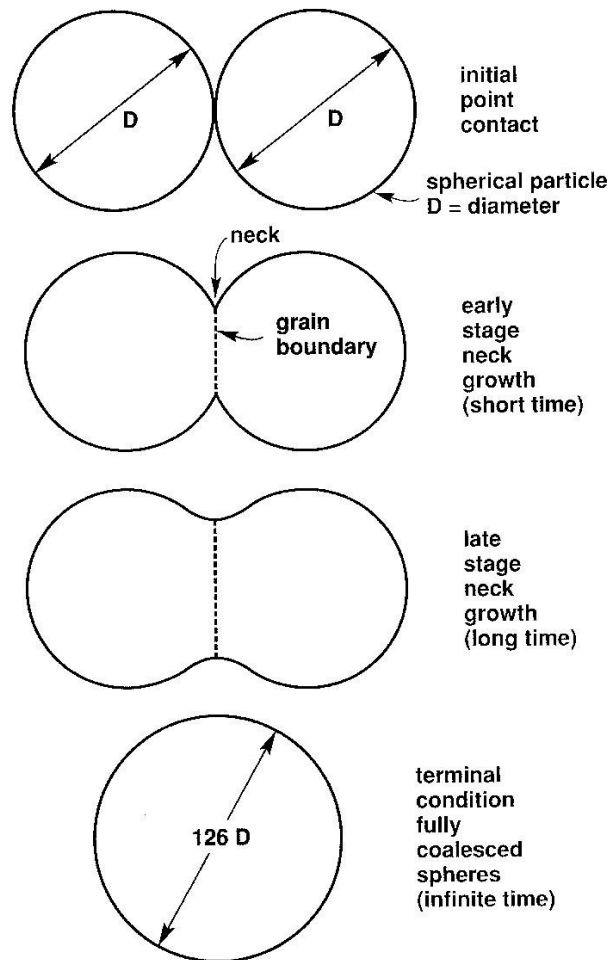


Figure 8 – Two sphere solid state sintering model [19].

There are two main mechanisms that can be used to describe what occurs during solid state sintering which are surface transport mechanisms and bulk transport mechanisms. Both of these mechanisms will contribute to neck growth within a powder compact. The process that make up the surface transport mechanisms are evaporation-condensation (E-C), surface diffusion (SD) and volume diffusion (VD). The bulk transport mechanisms are made up of grain boundary diffusion (GBD) and volume diffusion (VD). It is only the bulk transport mechanisms that contribute to shrinkage within a compact when referring to solid state sintering alone [16]. These sintering mechanisms are shown in Figure 9.

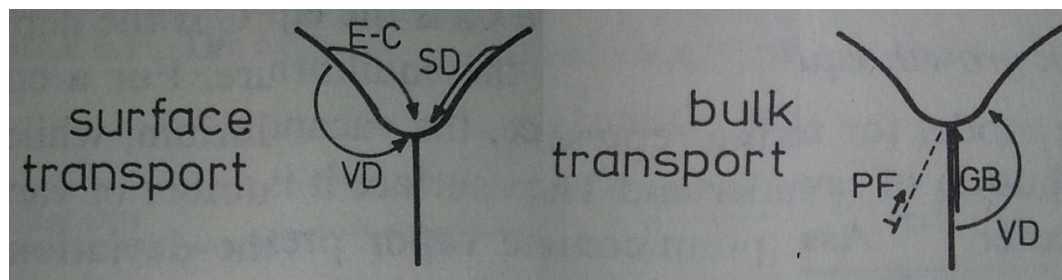


Figure 9 - Examples of surface and bulk transport mechanisms [16].

#### 1.7.1.2 Liquid Phase Sintering

A type of sintering that is commonly employed in industrial powder metallurgy operations is of the liquid phase type. The driving force behind this is a decrease in surface area in order to reduce the Gibbs free energy in the system. This results in the necking of powder particles thus reducing porosity [19]. The final percent theoretical density (porosity) of an object after sintering is highly dependent on its percent theoretical density after powder compacting. This underlines the importance of the compressibility curves noted in the previous section.

This is a very successful technique for creating parts made from mixed powdered materials as a liquid phase can spread through the porous structure of the green compact. Liquid phase sintering is often chosen for industrial applications because of the increased rate of sintering by forming a liquid. Once a liquid phase is formed within the compact upon heating, the liquid will be drawn between solid particles by capillary action. The small spaces between the solid particles within the green body act as small capillary tube

and draw the liquid between them. There are three main requirements for liquid phase sintering which are: a high solubility of solid in liquid, low solubility of liquid in the solid, and wetting of the liquid on the solid grains. There are four key stages within liquid phase sintering which are: a heating of the particles, particle rearrangement, solution-reprecipitation, and finished with solid state sintering. The stages within liquid phase sintering are shown in Figure 10.

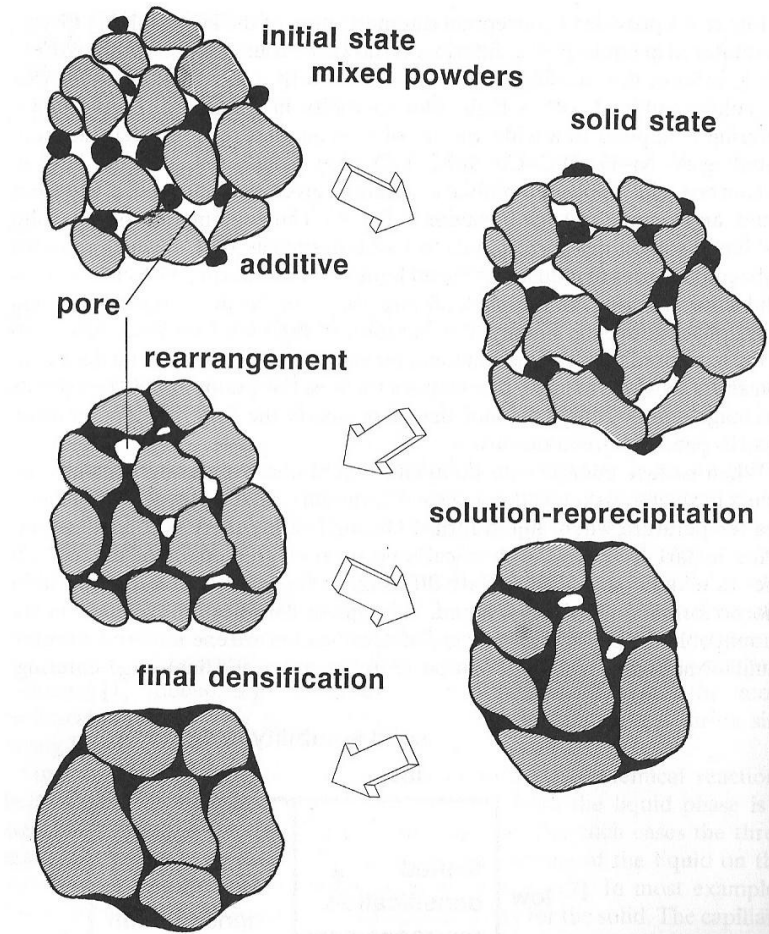


Figure 10 - Stages of liquid phase sintering [19].

LPS is the sintering mode used in the present work, principally because the aluminum added to promote gamma prime formation melts and subsequently reacts with surrounding ternary master alloy particles well in advance of the final sintering temperature (1300°C).

## 1.8 Porosity Reduction

One drawback of using P/M is the inherent presence of porosity after sintering. Therefore a method to increase the sintered density (reduce porosity) of the final product is needed to increase the mechanical properties and oxidation resistance. Various options have been proposed to increase the density of Superalloys produced by powder metallurgy. They include heat treatment, hot rolling, hot isostatically pressing (HIP), and HIP plus forging [20]. There is no evidence to confirm that any heat treatment process alone will increase the density of a powder metallurgy product as such processes are primarily used to modify the microstructure and change various mechanical properties to suit different applications [1]. Hot rolling could also be attempted, though atmospheric control may be difficult (initiating oxidation on the P/M produced sample) if the correct system is not used. HIP products have been shown to achieve full density though the HIP product usually has lower strength than its wrought counterpart [20]. As a result the HIP product can often require a thermomechanical treatment once powders are consolidated by this method. Options for thermomechanical treatment of these alloys (for a laboratory process) include forging or the use of a Gleeble thermomechanical testing system. The use of a Gleeble is preferred as the atmosphere, heating rate and applied pressures can be controlled. The Gleeble also offers the advantage of a rapid heating and cooling rate through resistance heating. This therefore allows for more rapid testing vs. a uniaxial press coupled with furnace heating in the same time period [21].

## 1.9 Oxidation Behaviour of Nickel-Based Superalloys

The oxidation behavior of Superalloys is important because it can reduce component life via [3]:

1. Reducing load bearing cross section
2. Introducing sources of stress concentration

There are four separate oxidation processes that can occur singularly or in combination which are [3]:

1. Surface scaling – This is the conversion of the metal to an oxide at the surface which will decrease the cross-sectional area and thereby diminish the amount of material for bearing a load.
2. Internal oxidation – further reduces the amount of load bearing material and introduces stress concentrations at the metal/oxide interface.
3. Oxide spalling – there is a heterogeneous scale of oxides grown on, and in the component which have different coefficients of thermal expansion (CTE). This mismatch can cause spalling under thermal cycling.
4. Oxide vaporization – oxides such as  $\text{Cr}_2\text{O}_3$  will vaporize at high temperatures (between approximately  $750^\circ\text{C}$  and  $900^\circ\text{C}$ ) and deplete the alloy of chromium.

This also reduces the amount of load bearing cross sectional metal and promotes higher oxidation rates.

Some desirable properties of oxide layers that will form on Superalloys are the initial formation of a thin, dense and continuous protective oxide film. After this initial transient oxidation it is beneficial to have a slow scale growth rate to minimize the loss in load bearing cross sectional area [22].

This oxide scale should be highly adherent to the un-oxidized metal substrate and the CTE's of the oxide and the metal should be as close as possible in an attempt to reduce spalling on thermal cycling [23].

The oxidation of any alloy system is complex as a result of several factors which include [10]:

1. Different elements have different affinities for different gases and the activities of these elements can change depending on alloy system.
2. The formation of spinels ( $\text{AB}_2\text{O}_4$ ), ternary or higher oxides.

3. Different metals have different diffusivities in different systems.
4. Complex nature of rates of reaction at the surface with the simultaneous depletion of oxidizing elements at the oxide/alloy interface and substrate.
5. Differences in grain sizes and production methods. Even alloys of the same composition will have different oxidation rates and can therefore form different oxides.
6. The diffusion rates of the anions (oxygen) and cations in various systems is a combination of the grain size in the oxide and alloy, and also is a time and temperature dependent process.

For nickel-based Superalloys containing aluminum and chromium oxide maps have been developed which schematically represent the oxidation behavior of various compositions of the Ni-Al-Cr system. These maps are developed by collecting oxidation data for various compositions and superimposing these data over a ternary diagram [24]. An example of this is shown in Figure 11 for alloys oxidized at 1000°C.

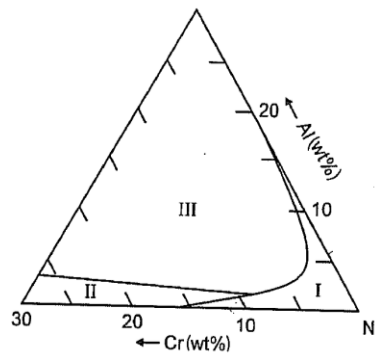


Figure 11 - The oxidation behaviour for various compositions of the Ni-Al-Cr system oxidized at 1000°C. The different regions represent: (I) - External NiO , internal  $\text{Cr}_2\text{O}_3$ ,  $\text{Al}_2\text{O}_3$  and spinels, (II) - External  $\text{Cr}_2\text{O}_3$ , internal  $\text{Al}_2\text{O}_3$ , (III) – External  $\text{Al}_2\text{O}_3$  [24].

These maps were created through careful examination of oxidized samples using a microscan electron probe-microanalyzer, standard x-ray diffraction and transmission electron microscopy [25]. The initial transient oxidation data collected for a Ni-15Cr-6Al sample oxidized at 1000°C are shown in Figure 12.



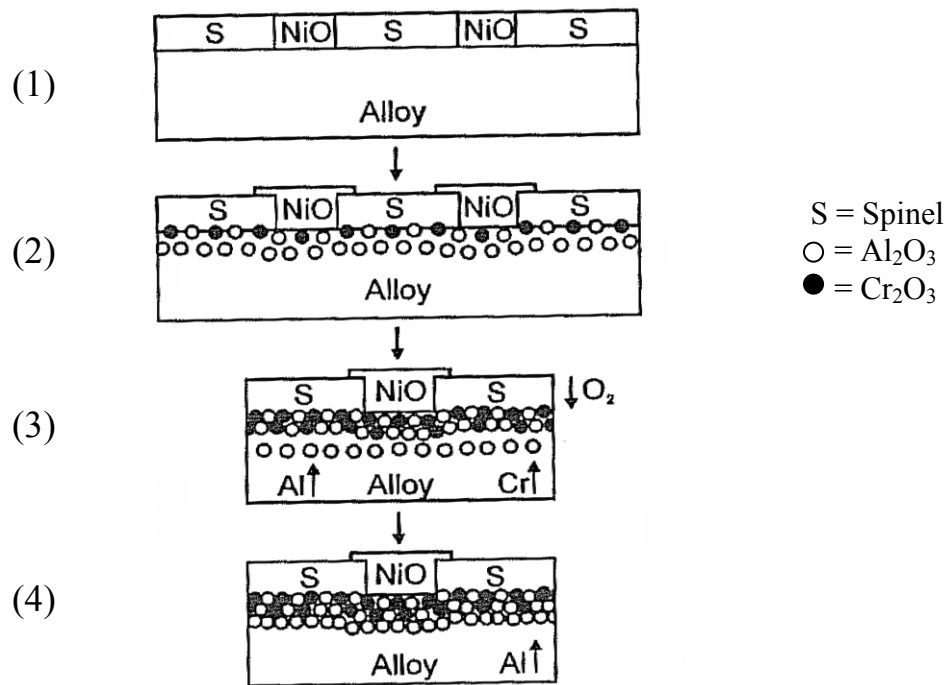


Figure 12- Oxidation stages and layers for a Ni-15Cr-6Al Superalloy at 1000 C for: (1) 1 min; (2) 5 min; (3) 40 min; (4) >40 min. Adapted from reference [25].

It is well known that there is a synergistic effect between the elements Cr and Al within these nickel-based systems. By having the two elements together in the system the overall aluminum amount in the alloy can be decreased while still promoting the formation of the stable alumina layer [24].

Growth mechanisms of the oxides for systems containing both Cr and Al change in the region of 750°C-1100°C. Chromia is protective below approximately 900°C where chromium is diffusing outward to oxidize, above this temperature it may vaporize. Alumina is protective at above 900°C and the aluminum diffuses outward to oxidize at the alloy/oxide interface. At 1100°C alumina protective oxygen now diffuses inward and oxidizes the aluminum at the metal/oxide interface. These processes are still deemed “simple generalizations” and cannot be used for all compositions [25].

The literature has indicated that Superalloys containing aluminum that are doped with one or more reactive elements precipitate a greater fraction of gamma prime (compared with un-doped) and exhibit greater oxidation resistance [26] [27]. There are other

beneficial effects of the minor additions which are a slow growing, adherent oxide layer that is resistant to spalling. These elements include yttrium, boron, zirconium, lanthanum, and silicon [28].

An alternative approach is to incorporate a second precipitate-forming element such as titanium. In this case the major precipitate within Ni-based Superalloys is of the form  $Ni_3(Al,Ti)$  [1]. A P/M study to evaluate the potential microstructural advantages of adding 3w/o Ti to such an alloy is given by Murray [29]; however, only a minimal effect was noted in the final microstructure (precipitate size was increased with the addition of Ti).

### **1.10 Reactive Element Additions**

The beneficial effects of reactive element additions to the oxidation of nickel-based Superalloy systems have been well documented. Elements that have been said to improve the oxidation resistance of these alloys include Sc, Y, Zr, La, Hf, Ce, Yb, Th, Mn and Si along with several other rare earth elements [3] [24] [25]. The exact effects of these elements vary depending on which alloy system they are in, the amounts to which they are present, the homogeneity of their distribution and how they were introduced to the system (i.e. ion implementation vs. diffusion coating) [3] [30] [31]. There is no one agreed-upon reason behind the mechanism for the increased scale adherence of the oxide layer when reactive elements are added to these systems. The proposed mechanisms for the increased adherence of the oxide layer when reactive element additions are that they [24]:

1. Act as vacancy sinks thereby suppressing void formations
2. Form oxide pegs which helps scale adherence
3. Alter the growth mechanism which reduces alloy/oxide stresses
4. Strengthen alloy/oxide interface through segregation to this interface and the form a graded seal
5. Increase oxide plasticity by changing the CTE of the oxide which reduces spalling
6. Tie up sulfur present in the alloy to prevent the formation of brittle sulfides at the alloy/oxide interface

7. Slow the diffusion of the cations trying to break through the various oxide layers

Most researchers do agree that if present in the proper amounts, (between approximately 0.1% ~ 1% w/o) reactive elements can be a benefit with regards to the adherence of the oxide layer that is developed on various nickel-based Superalloys [25]. Figure 13 is a schematic comparison for the alloys CoCrAl+(Y or Hf) and NiCrAl+Zr during cyclic and isothermal oxidation.

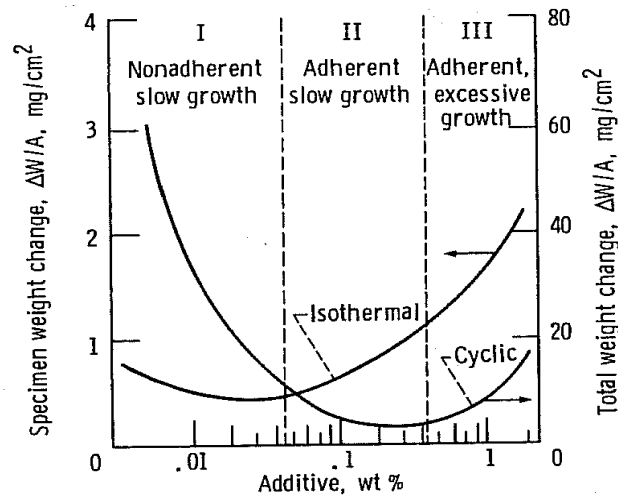


Figure 13 - Schematic representation weight change during isothermal and cyclic oxidation of CoCrAl+(Y or Hf) and NiCrAl+Zr vs. the amount of reactive element addition [25].

It should be noted that the gain in oxidation behavior of the Superalloys through the addition of reactive elements is also generally associated with a decline in mechanical properties such as tensile strength [25].

It has also been proposed that co-operative doping of Superalloys with more than one reactive element can reduce the overall amount of reactive element additions needed to achieve the beneficial results of a singularly doped one. This could reduce the cost of the alloy while achieving the same beneficial results of a more adherent scale [23].

### 1.10.1 Silicon Additions

Silicon has a reactivity between aluminum and nickel and is added to Hastalloy X to increase the oxidation resistance of the alloy [25]. It has the largest beneficial effect in

alloys which produce protective alumina and/or chromia scales. The addition of between 0.5-1.3 w/o Si has been shown to improve the cyclic oxidation resistance of an aluminide coating applied to B-1900, MAR-M 200 and IN-713(Cast Ni-based alloys) [30].

The reasons for these benefits are thought to derive from formation of SiO<sub>2</sub> subscales and prevention of the formation of Ni(Fe) oxides [25]. Another suggested benefit of Si on the chromia forming nickel-based Superalloys is that it could form a thin silica layer at the alloy/oxide interface. It is stated that this layer could impede chromium and oxygen diffusion thereby decreasing the kinetics of the chromia formation [32]. Silicon additions have also been reported to increase the activity of aluminum in these systems which helps create a thinner, faster forming layer of alumina at the alloy oxide interface. The amount of precipitated  $\gamma'$  phase within these alloys has also been shown to increase with additions of silicon further increasing the high temperature strength of these alloys [33].

### **1.10.2 Yttrium Additions**

There are several reported benefits that occur with the additions of yttrium to nickel-based Superalloys with regards to oxidation. These benefits include [24] [25] [34] [35]:

1. Enhancement of the selective oxidation of Cr or Al in systems containing these elements
2. Reduction in growth rate of Cr<sub>2</sub>O<sub>3</sub>
3. Change in diffusional process for Cr (O anion diffusion inward rather than Cr cation diffusion outward)
4. Largest benefits noted in thermal cycling where spalling normally occurs
5. Restricts grain growth in the alumina forming scale by segregating to aluminum oxide grain boundary
6. Prevents lateral oxide growth
7. Dominance of inward oxygen anion diffusion which limits diffusion outward of cations (i.e. Cr)
8. Prevention of void formation at alloy/oxide interface
9. Reduction of oxide grain growth during oxidation
10. Pegging or keying effect for enhanced scale adherence

11. Change in directionality of the oxide growth to columnar and normal to the oxidizing surface
12. Lower stresses generated at the metal/oxide interface resulting in increased adherence

These are not universally agreed upon though most authors agree that there is a pegging effect for any Y addition at or just above 0.1% and there is generally a reduction in spallation for cyclically oxidized samples in most nickel-based Superalloys. Through most oxidation studies a reduction in void formation at the alloy/oxide interface has also been noted [35]. An example of the yttria pegs is shown in Figure 14.

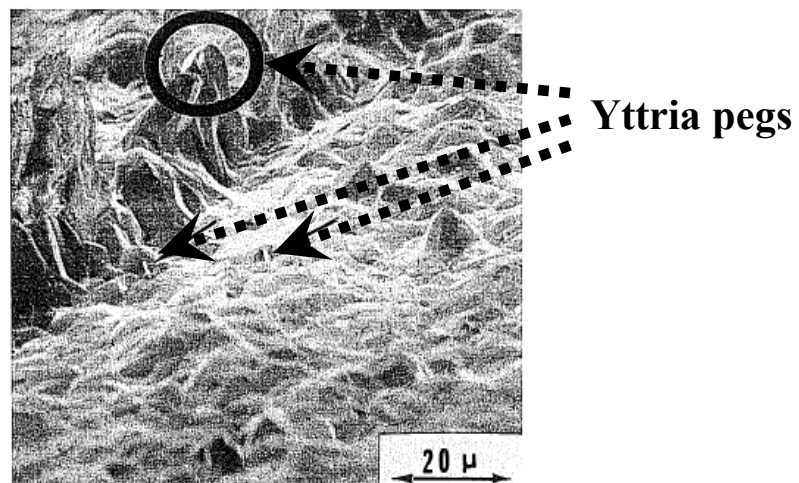


Figure 14 - An SEM micrograph of yttria pegs at the oxide alloy interface after the metal substrate removed [36].

### 1.11 Modeling via JMat Pro

JMat Pro is a computer software package that uses thermodynamic modeling to predict [37]:

1. Stable and metastable phase equilibria
2. Solidification simulations
3. Mechanical properties
4. Thermo-physical and physical properties
5. Phase transformations

6. Stacking fault energy
7. Chemical properties

The software is based on the CALculation of PHAse Diagrams (CALPHAD) database of thermodynamic properties gathered for various binary and ternary systems. If the thermodynamic properties are well documented for a system, it is possible to combine the thermodynamic information (i.e. Gibbs energy of each phase present) and draw conclusions (based on thermodynamic equilibrium) for various compositions. The time consuming and costly methods needed to determine the phase diagrams and properties of systems has been greatly decreased with the use of software programs such as JMat Pro or Thermo-Calc [37]. The thermodynamic software can make calculations for various compositions that can then be verified through standard laboratory methods, saving time in the development and optimization of alloys. The software has been validated with various materials such as a variety of Nimonic Superalloys [38].

In the present study the software was used to predict temperature for the onset of gamma prime precipitates on cooling from sintering temperature, the liquation of the alloy post sintering, as well as the volume fraction of precipitates that would be expected to be present on cooling to room temperature following a sintering regime.

## CHAPTER 2     **Research objectives**

The objectives of this thesis are to develop a suitable P/M process for fabricating sintered compacts of a nickel-based alloy similar to Inconel 600 in composition and subsequently to assess the benefits (or otherwise) regarding oxidation resistance of adding silicon and/or yttrium to the compacts. As a starting point, the software JMatPro was used to provide predictions of onset of gamma prime formation as well as melting point of the various compositions investigated. The models were then used to develop a suitable sintering regime and static oxidation tests were employed to assess oxidation behaviour. Final P/M sample characterization involved microstructural examination, hardness testing, X-ray diffraction (XRD) evaluation and use of differential scanning calorimetry (DSC) to document any endothermic or exothermic reactions that may occur on sintering.

## CHAPTER 3     **Materials and Methods**

The materials used and methodologies employed in this work are detailed in the following sections.

### **3.1 Materials**

A simple three component starting material was chosen to replicate Inconel 600 because the intent was to simulate a nickel-based Superalloy using a powder metallurgy approach. Specifically, the base master alloy ternary powder used in this study had a composition of Ni72:14-17Cr:6-10Fe (w/o) as a 325 mesh pre-alloyed powder produced by Alfa Aesar® through inert gas atomization  $d_{50} = 37 \mu\text{m}$ . This material had been used in previous studies on developing a P/M process suitable for Ni-based powders [39].

To promote formation of gamma prime precipitates, 6w/o aluminum was added to the ternary powder mixture. Finally, for the oxidation resistance studies, 0.5w/o silicon and/or 0.1w/o yttrium was added as appropriate.

The silicon and yttrium powders used were also produced by Alfa Aesar® through inert gas atomization and were listed as 99.5% and 99.9% respectively pure metals, 325 mesh. The aluminium powder was obtained through Ecka Granules and was listed to have a  $d_{50}$  of  $6\mu\text{m}$ .

Throughout this thesis the master ternary nickel alloy will be referred to as “the ternary” or T, the alloy modified with 6w/o Al as TA and for the oxidation testing whereby Si and/or Y was added, TAS, TAY or TAYS.

### **3.2 Methods**

#### **3.2.1 Powder Characterization**

Powder characterization was carried out using a Malvern laser particle size analyzer for the log normal plots of the powder size distributions. The powders were prepared for



visual and chemical analysis by pouring loose powder onto an aluminum stub coated with silver paste and allowing the paste to set for 24h. The resulting microstructures, morphologies, and general compositions were then analyzed using a JEOL JSM-5900LV scanning electron microscope (SEM) equipped with an Oxford 50mm<sup>2</sup> X-MAX energy dispersive spectrometer (EDS).

### **3.2.2 Powder Processing**

#### **3.2.2.1 Blending**

The base ternary powder was mixed with various amounts and combinations of Al, Si and Y in small laboratory batches (300g). All compositions were mixed with 0.75w/o microwax (lubricant) in order to reduce die wear and aid in compaction. This amount of lubricant was previously determined to be optimum through previous research by Akinlade [39]. Blending was carried out in a Turbula Model T2M mixer and each composition was blended for 30min in order to obtain chemical homogeneity within the powder blend.

#### **3.2.2.2 Compaction**

Transverse Rupture Strength (TRS) bars of approximate dimensions 31x13x8mm were produced using a Satec Systems Model 5594 -200HVL 1000kN load frame. Samples were pressed at a rate of 2kN/s until the desired load was achieved. TRS bars were compacted using pressures of 400-600MPa in an attempt to determine the optimum compaction pressure which would yield the highest density of the TRS bar in the sintered condition.

#### **3.2.3 Delubrication**

All green TRS bars were subsequently heated in a Lindburg Blue 3-Zone Furnace Model STF55666C-1 equipped with 3 UP150 control modules. This was done under flowing nitrogen for 30min at 400°C to remove the lubricant that was used to reduce die wear during pressing.

### **3.2.4 Thermodynamic Modelling**

Thermodynamic modelling was carried out on the various compositions that were produced using JMat Pro® software. The software is based on the CALculation of PHase Diagrams (CALPHAD) database of thermodynamic properties gathered for various binary and ternary systems [37]. Using this information the software is able to predict various physical or chemical properties and phase transformations such as solid to liquid phase changes or precipitation of secondary phases (e.g. gamma prime) based on the principle of minimization of Gibbs free energy [37]. Data bases for various alloys are available; the one chosen for the present work was for nickel-based alloys.

### **3.2.5 Differential Scanning Calorimetry (DSC)**

The behaviour of both green samples in terms of endothermic and exothermic events on sintering and sintered samples regarding onset of melting and intermetallic solutionizing temperature was examined using a Netzsch 404C differential scanning calorimeter (DSC) from room temperature to 1300°C. Heating/cooling rates of 2.5<sup>0</sup>C/min were employed. Samples size were in the form of 6mm diameter cylinders that weighed approximately 100mg.

### **3.2.6 Sintering**

An optimum sintering profile for the ternary + 6wo Al had previously been developed by Akinlade [39] which consisted of three stages as follows: (1)Heating at 10°C/min up to 1300°C; (2) a hold of 2h at 1300°C followed by; (3) cooling at 10°C/min down to room temperature as shown in Figure 15. All sintering was done in a bell furnace produced by Materials Research Furnaces Inc. under 10<sup>-5</sup> torr vacuum.

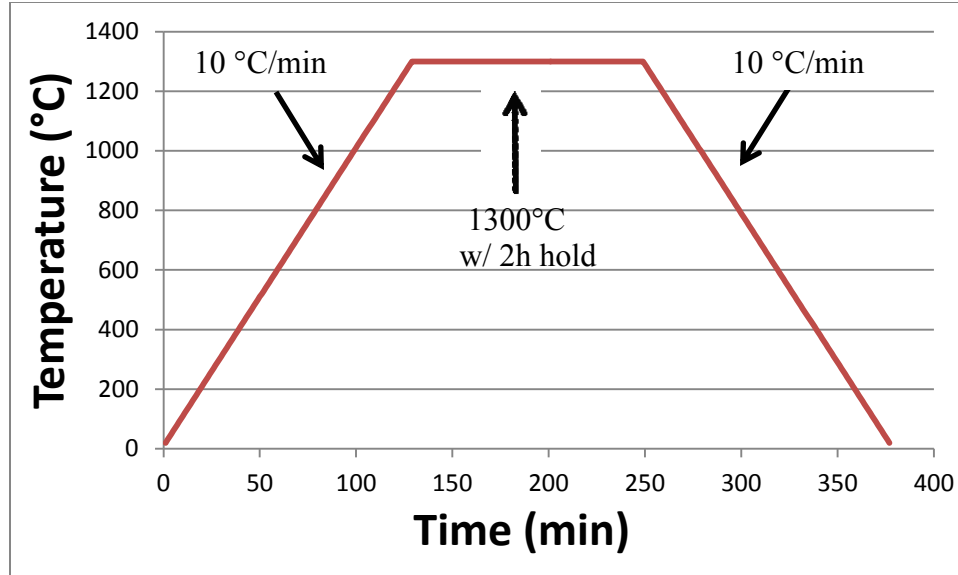


Figure 15 - Sintering profile used for de-lubricated TRS bars.

### 3.2.7 Density Measurements

Density measurements were performed on a representative number of samples to quantify the final density (or porosity) of the sintered compacts. Samples were first weighed in air, then infiltrated with ESSO-NUTO H46 hydraulic oil, followed by weighing in air once more with oil impregnation. The oil impregnated samples were then weighed while suspended in water. The density of the compacts could then be determined using Equation 1.

$$\rho_{compact} = \frac{M_{Air} \times \rho_{water}}{M_{Airw/Oil} - M_{Waterw/Oil}} \quad \text{Equation 1}$$

Where  $\rho_{compact}$  is the density of the sintered compact,  $M_{Air}$  is the mass of the compact in air,  $\rho_{water}$  is the density of the water that the compact was submerged in.  $M_{Airw/Oil}$  and  $M_{Waterw/Oil}$  are the masses of the compact in air and water respectively after oil infiltration. The density of water was calculated using Equation 2.

$$\rho_{Water} = 7 \times 10^{-8} T^3 - 1 \times 10^{-5} T^2 + 1 \times 10^{-4} T + 0.9996 \quad \text{Equation 2}$$

Density measurements also were carried out using MPIF standard 42 [40] following Arrhenius' principle where samples were weighed both in air and while suspended in a jar of distilled water. The density could then be calculated using Equation 3.

$$\rho_{compact} = \frac{M_{Air} \times \rho_{Water}}{M_{Air} - M_{Water}} \quad \text{Equation 3}$$

### 3.2.8 Electrical Discharge Machining (EDM)

Electrical discharge machining was employed to prepare sintered samples for Gleeble thermo-mechanical deformation prior to oxidation testing. This was done on as-sintered samples using a Hansvedt EDM, model DS-2 traveling wire EDM (aqueous environment) as seen in Figure 16. (Parameters: Pulse 2.4/ $\mu$ s, % On-Time 2.5, Peak Amps 3.0, Gap Spacing 3, Servo-Speed 12, cut off 2)



Figure 16 - Image of the traveling wire EDM used in the present research.

### 3.2.9 Thermo-mechanical Deformation

In an effort to reduce the porosity of the as sintered TRS bars Gleeble thermo-mechanical deformation was employed. All deformation was carried out in a Gleeble 1500 D Gleeble thermo-mechanical tester that was produced by Dynamic Systems Incorporated™. Prior to deformation, samples were sectioned using the EDM to approximately 10x12x8mm, polished through 600 grit SiC paper and wired with Type K thermocouples as shown in Figure 17. To ensure that the samples did not weld onto the WC anvils, Ta foil was attached to two faces of each sectioned TRS bar.

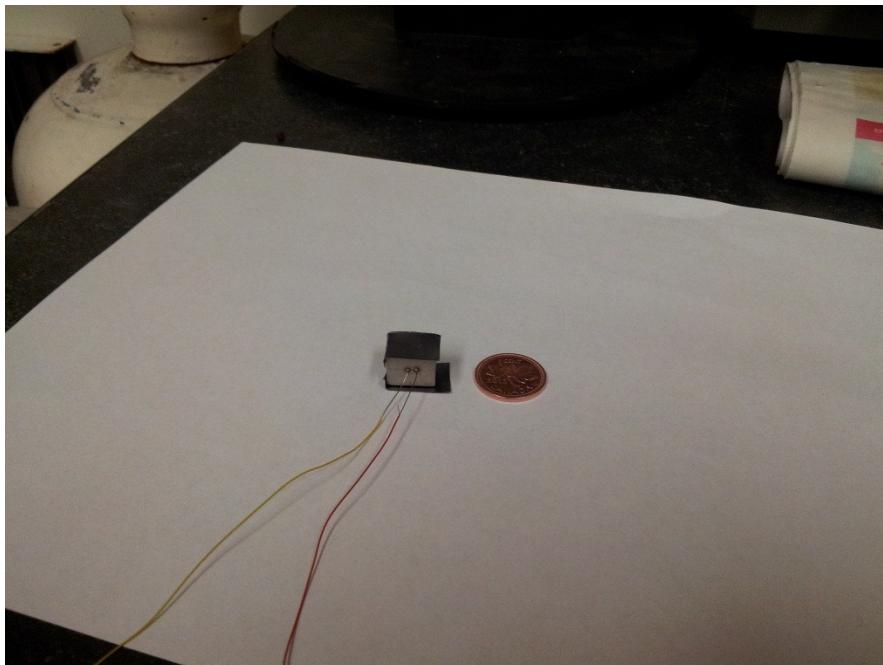


Figure 17 – Image of wired sample in prepared for Gleeble thermomechanical deformation.

During hot deformation the samples were heated at a rate of 450°C/min, held at 1200°C for one minute, deformed in amounts of 10% up to 40% of their original width over a period of 2 seconds and cooled back to room temperature at a rate of 450°C/min. A sample undergoing hot deformation can be seen pictorially in Figure 18. Visual inspection of the samples was then performed to ensure no cracking of the samples had occurred. Density measurement was undertaken using MPIF 42 [40] and some SEM-EDS

analysis performed in an effort to confirm there had been no transfer of Ta into the samples or vice versa.

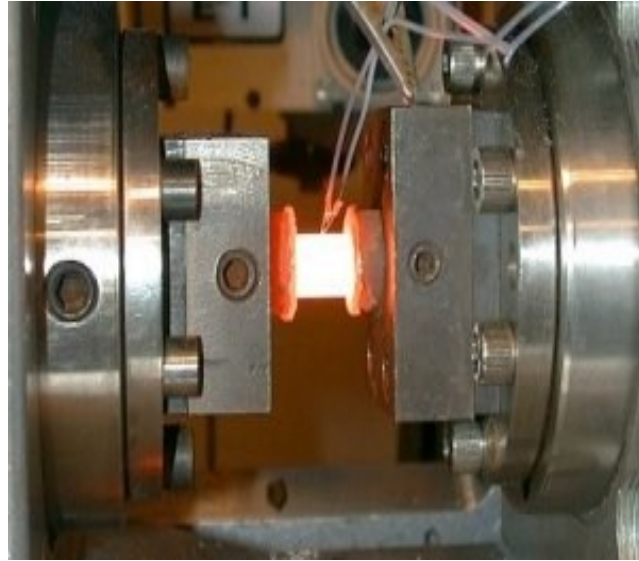


Figure 18 - Sample undergoing thermo-mechanical deformation.

### **3.2.10 Heat Treatment**

Various heat treatment procedures were tested between 750°C and 950°C from one to four hours in order to re-constitute the gamma prime precipitates noted prior to Gleeble thermo-mechanical deformation. In preparation for heat treatment the thermo-mechanically deformed samples were placed in Vycor™ ampoules that had been drawn/sealed under  $< 10^{-6}$  torr vacuum in an attempt to minimize oxidation of the samples while ageing as shown in Figure 19. Initially heat treatments were carried out in a Lindberg/Blue M model BF 51894C-1 box furnace. However the samples that were ultimately used for oxidation testing were heat treated in a vacuum furnace fabricated in house at the University of Manitoba.



Figure 19 - Thermomechanically deformed 1 cm sample that has been prepared for ageing.

### **3.2.11 Oxidation**

Deformed and aged samples were sectioned into approximately 1.5x7.5x6.5mm coupons using the EDM and polished through 600 grit SiC paper. Samples were then cleaned in methanol and carefully weighed using AND company Ltd., FR-200 MKII scale/balance with dimensional measurements also recorded. Coupons were then placed in alumina crucibles, subsequently into a 316 low carbon stainless steel platform and then oxidized at 900°C under static air for up to 1000h in the Lindberg/Blue M model BF 51894C-1 box furnace to monitor the high temperature oxidation behaviour of the alloys.

Figure 20 and Figure 21 show the configuration of the crucibles and the platform prior the oxidation. Four samples, one for each composition investigated, namely TA, TAS, TAY and TAYS, were removed after each of 10 oxidation times. This test was done twice in order to achieve a standard deviation on the data collected and to repeat anomalous data points (2 x 40 = 80 samples).





Figure 20 – Test setup with samples in glazed alumina crucibles prior to oxidation.



Figure 21 - Test setup crucibles in stainless steel tray prior to oxidation.



### 3.2.12 Microscopy

Following the oxidation tests the microstructures of selected samples were examined using the SEM EDS (JEOL 5900-LV/Oxford Link). Samples were first polished to 1 $\mu$ m diamond paste and subsequently electrolytically etched in a solution of 12ml 70% H<sub>3</sub>PO<sub>4</sub> + 40ml 70%HNO<sub>3</sub> + 48ml 98% H<sub>2</sub>SO<sub>4</sub> ( $\gamma'$  etchant) at 5V for 1-5s. Where appropriate, the volume fraction and size of precipitates was determined using a point count method.

### 3.2.13 X-Ray Diffraction

X-ray diffraction patterns were obtained of the as-sintered, deformed, and deformed+aged samples using a Rigaku X-ray diffractometer. The parameters used in this instrument were a Cu, K $\alpha$  radiation using a wavelength  $\lambda = 1.54056\text{nm}$  and 40mA current and a voltage of 40kV. Analysis of the diffraction patterns was carried out using WINJADE analysis software in order to identify the various phases present after each stage of processing.

### 3.2.14 Hardness Measurements

Hardness measurements were carried out on the samples in the as-sintered, deformed and deformed + aged samples using a Vickers hardness tester with a 50kg/f load. Every face of the tested sample was polished with 240, 400, then 600 grit SiC paper. A minimum of eight readings were taken from each sample with the highest and lowest values from each sample being dropped. An example of the faces tested is shown in Figure 22.

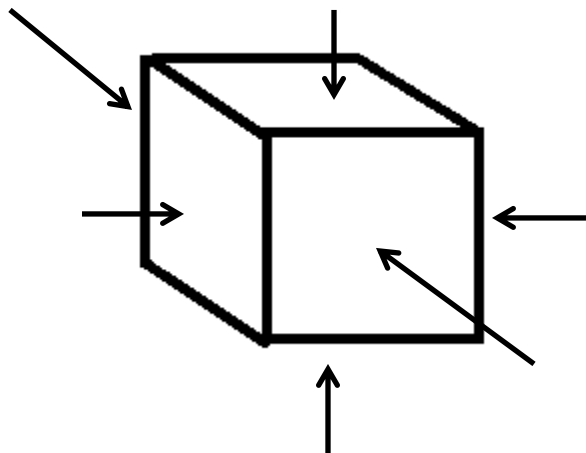


Figure 22 – An example of the faces tested during hardness testing.

## CHAPTER 4 Results and Discussion

### 4.1 Materials

The following sections outline the steps followed in characterizing the P/M materials used.

#### 4.1.1 Microscopy

The starting materials, namely the master ternary nickel alloy, aluminum, silicon and yttrium powders were characterized prior to compaction/sintering.

A representative SEM micrograph of the base ternary powder is shown in Figure 23.

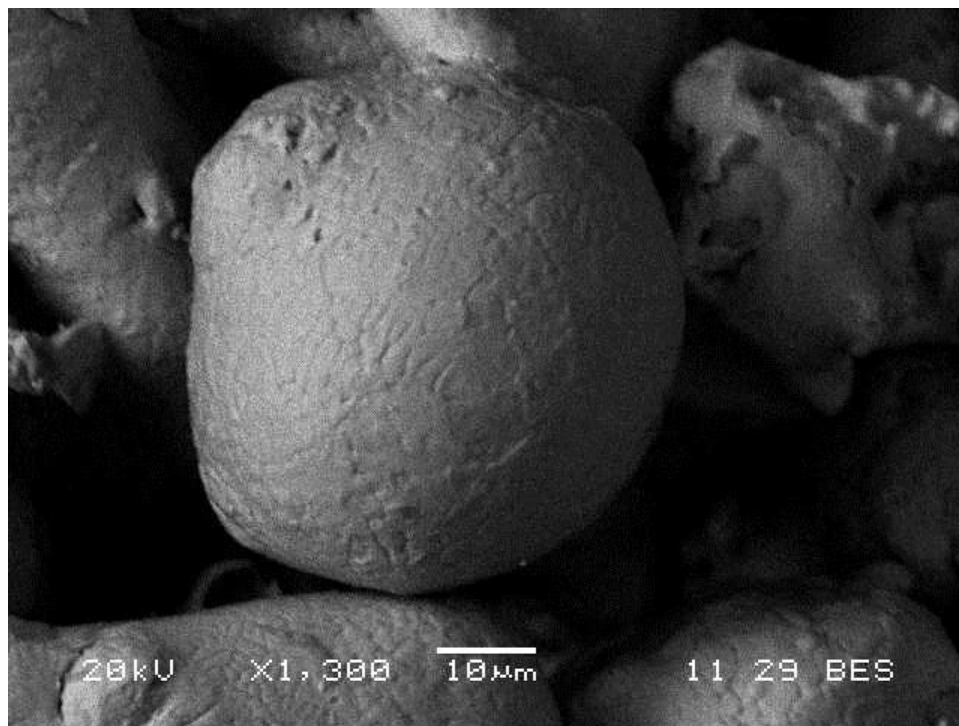


Figure 23 – Representative SEM micrograph of the base ternary powder.

The micrograph shows prior particle boundaries that are typical in pre-alloyed nickel-based powders. As can be seen, the powder was spherical to rounded in shape which is indicative of inert gas atomized powders.

The prior particle boundaries ideally would disappear on complete sintering. However, as will be discussed later, residual porosity in the order of 10 % was present in all samples even after hot forging in the Gleeble. As a result the boundaries persisted in all samples during the oxidation testing.

Within the characterization battery performed on the loose powders it is imperative to verify the compositional analysis provided by the manufacturer of the powder. This improves quality and repeatability in both industrial and research settings. A standardless EDS analysis of the base ternary powder was performed to compare the values supplied by the manufacturer and the actual powder lot received. The results are shown in Figures 24, 25 and Table 1.

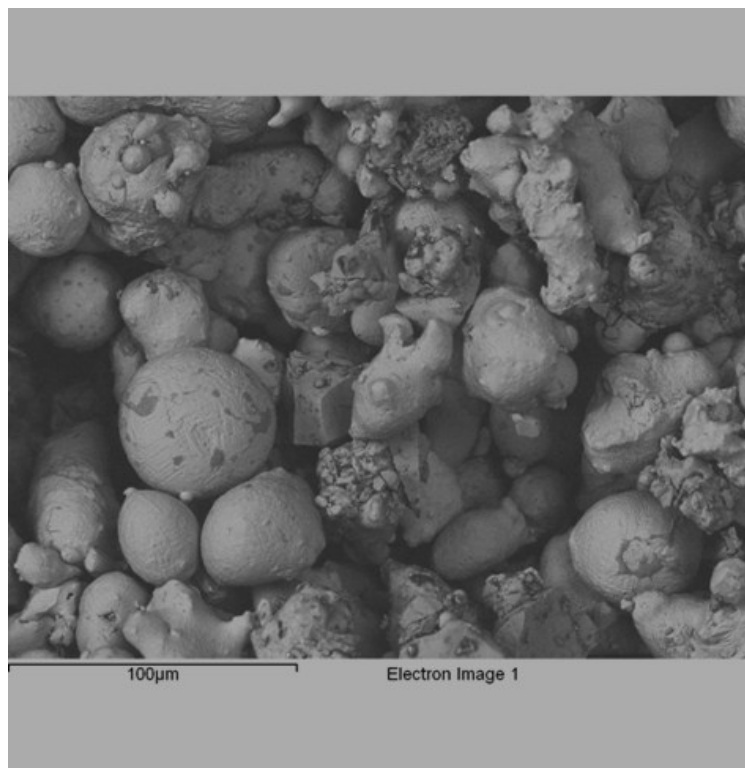


Figure 24 – SEM micrograph of the base ternary powder.

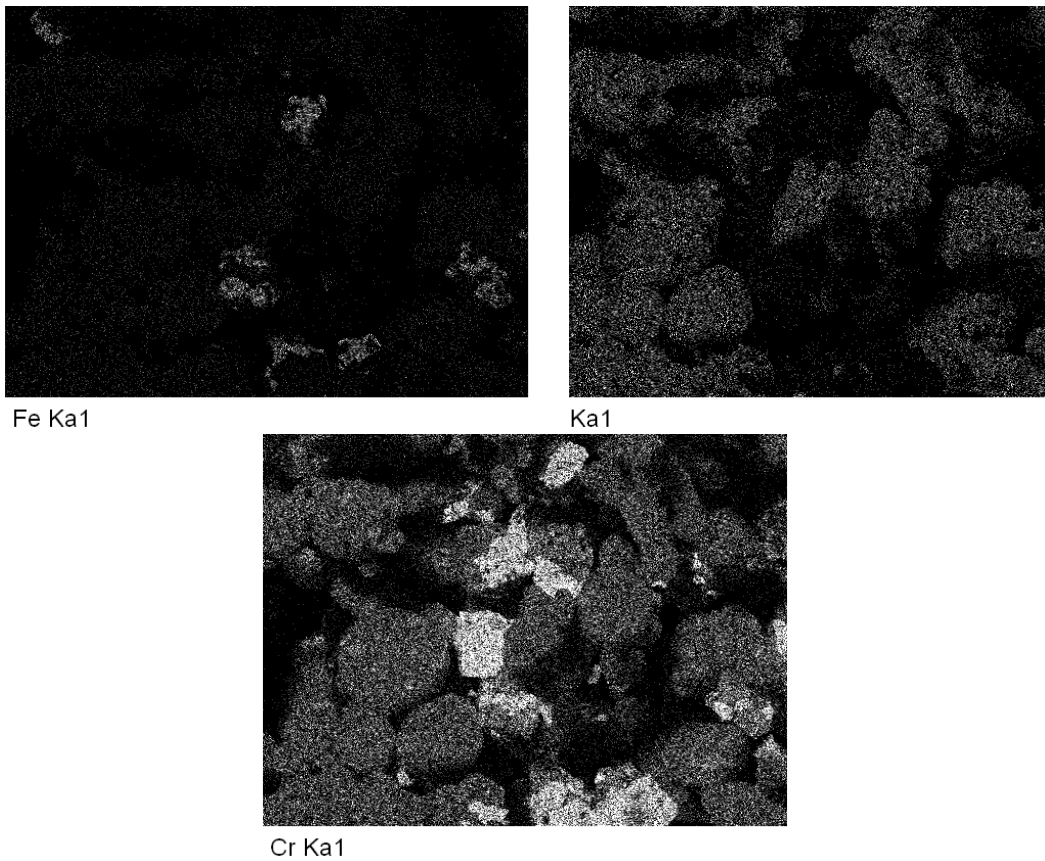


Figure 25 - Standardless elemental mapping of the elements found in the base ternary powder.

Table 1 – Semi-quantitative EDS results for the base ternary powder.

<b>Element</b>	<b>Average Content (w/o)</b>	<b>Range (w/o)</b>	<b>Standard Deviation</b>
<b>Nickel</b>	<b>78.7</b>	<b>77.4-80.4</b>	<b>1</b>
<b>Chromium</b>	<b>12.7</b>	<b>10.6-13.9</b>	<b>1</b>
<b>Iron</b>	<b>8.7</b>	<b>7.9-9.3</b>	<b>0.5</b>

The atomic weight percents attained through EDS were Ni-12.7Cr-8.7Fe which were within +/- 0.7% to the compositional analysis supplied by Alfa Aesar of Ni-12Cr-9Fe (w/o) from a total of 12 elemental maps on random positions within the powder sample. However, isolated occurrences of pure Cr and Fe were also found. These artifacts should

not influence either sintering response or the oxidation testing results. However their presence in selected micrographs is noted where appropriate.

#### 4.1.2 Particle Size Analysis

Laser particle size analysis was carried out on all powders using the Malvern particle size analyzer; the results are shown in Figure 26.

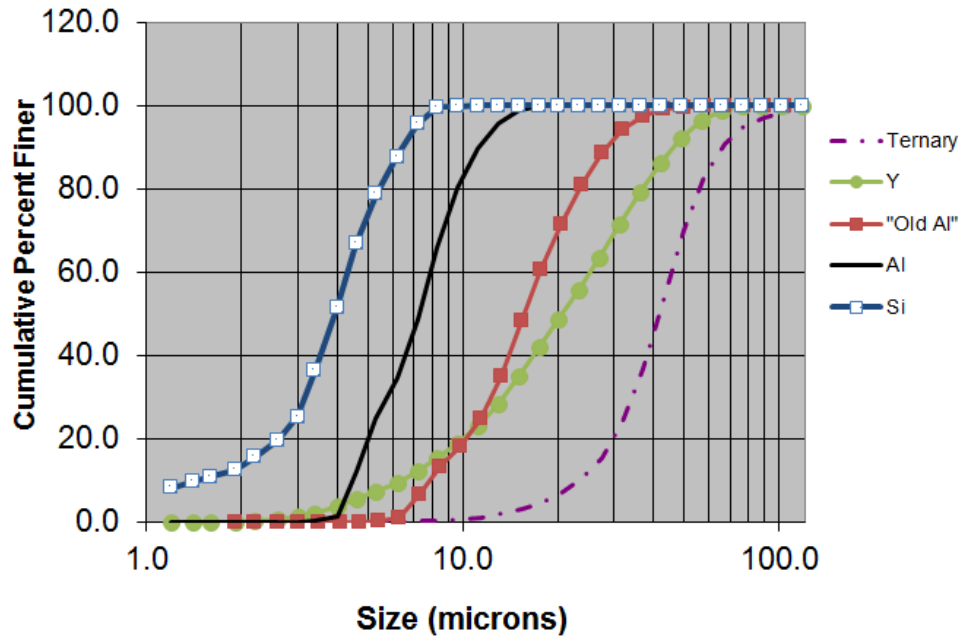


Figure 26 - The results of the laser particle size analysis.

The plot shows that the  $d_{50}$  values for the Al, Si and Y are all less than the value for the starting master alloy. This was to ensure maximum % theoretical green density after blending/compaction whereby the smaller particles can fill voids between the master alloy particles [11].

As an attempt to further increase green density a 7.2 micron Al material was substituted for the 15.6 micron Al ("old Al"). This had little effect on green density but improved sintering response and thus was used for the final samples prepared in the thesis. Where appropriate the size used is documented.

The particle size comparisons given in Figure 26 show that the  $D_{50}$  value for the base ternary powder is approximately  $42\ \mu\text{m}$ . The  $D_{50}$  value for the yttrium is approximately half that size at  $20.7\ \mu\text{m}$ , after which there is a significant drop in particle size. The aluminum and silicon, which have  $D_{50}$  values of  $7.2$  and  $3.9\ \mu\text{m}$ , respectively, play an important role in improving the sintering response of the compacts. Though compressibility is reduced by increasing friction between the particles, the packing density and therefore the sintering response is increased due to more contact between the surface area of the particles as shown in Figure 27.

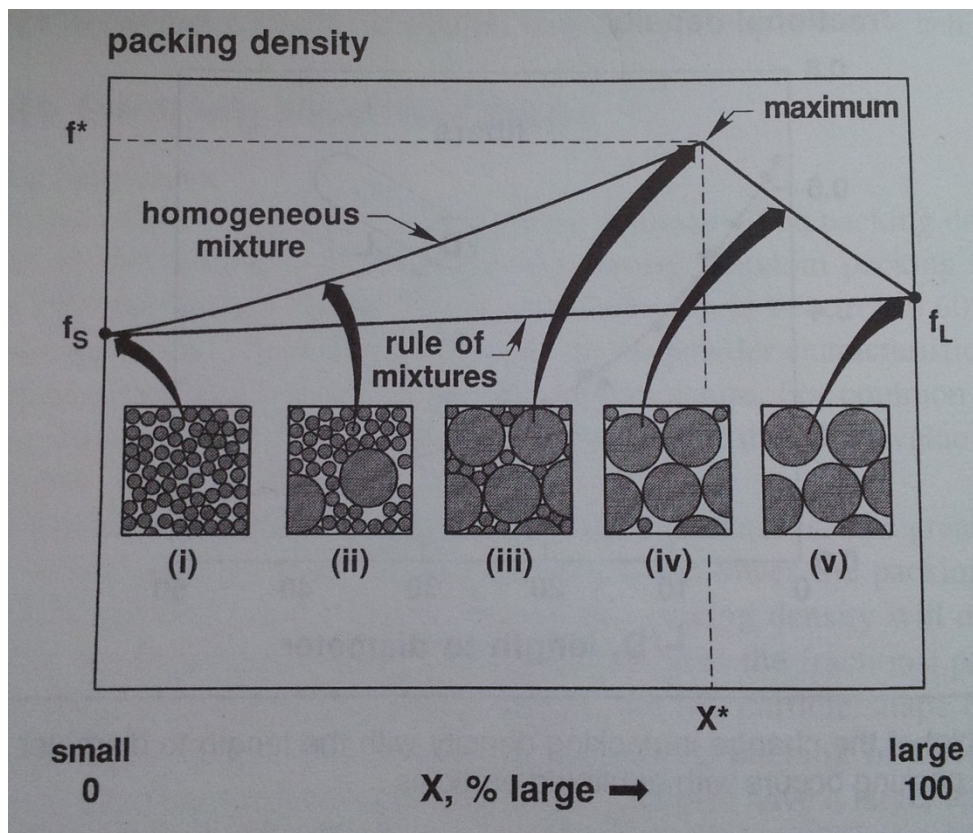


Figure 27 – Packing density of a mixture of powder sizes [11]

This underlines the importance of having both a particle size distribution (rather than a uniformity of particle size and shape) and ensuring that the alloying elements of interest (in this case Al, Si, Y) are smaller than the master ternary alloy.

## 4.2 Blending and Compaction

Following a previous work, (Akinlade, D.A. et al) [28], 6w/o Al powder was added to the Ni ternary to promote gamma prime formation, with 0.75w/o microwax added and the mixture blended in the Turbula blender for 20 minutes. Where appropriate for the oxidation resistance studies, Si and or Y powders were added to the blend. The amount chosen to be added (0.5 w/o Si; 0.1 w/o Y) was based on typical industrial standards for wrought Ni-based Superalloy materials as documented in Superalloys II by Sims, Stoloff and Hagel [25].

The compaction pressure was then determined via compressibility tests using an Instron 5595 Satec press; a typical compaction curve is given in Figure 28 for the ternary-6Al-3Ti samples examined by Murray et al [29] previously.

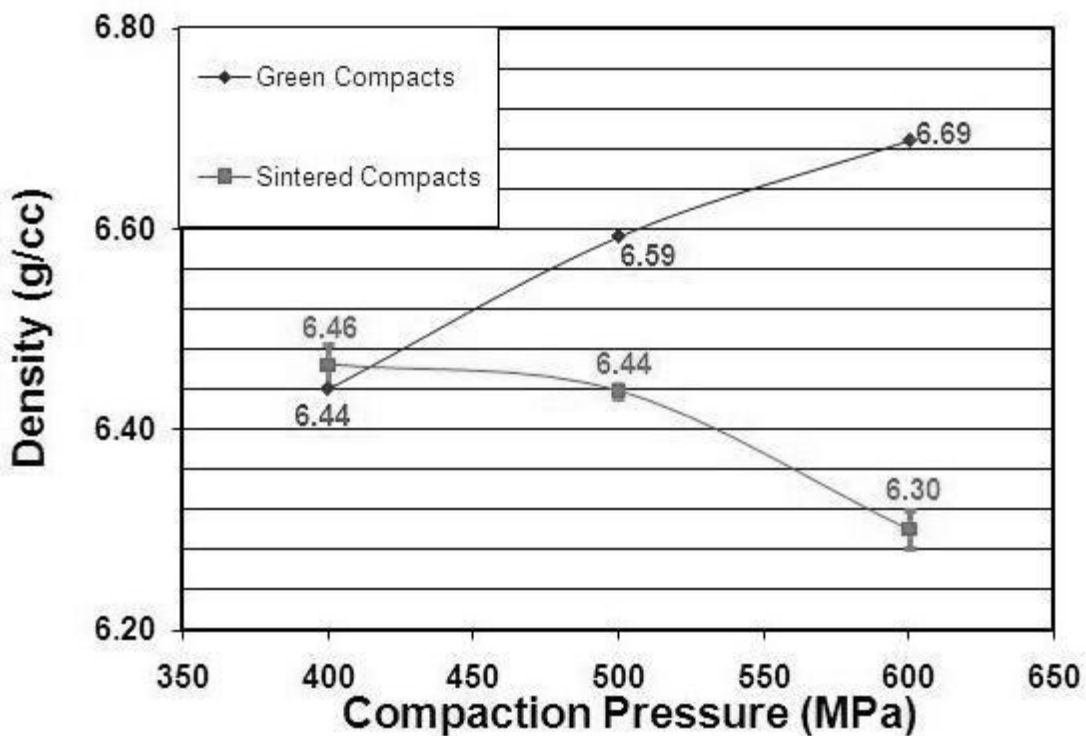


Figure 28 – Plot of density (green and sintered) as a function of compaction pressure for ternary + 6w/oAl + 3w/oTi samples [29].

From Figure 28 it can be seen that porosity for sintered compacts varies inversely with the green bodies at increasing compaction pressures. The reason for this may well be that

at higher pressures there is more closed porosity leaving pores trapped between particles with no pathway to facilitate liberation. Because the compaction curves showed that there were diminishing returns on compression from 500MPa to 600MPa and also the error bars overlapped, 500 MPa was chosen. This facilitated comparison with previous work that also used 500 MPa [28].

Based on theoretical densities ranging from of 8.10 to 8.61g/cm<sup>3</sup> acquired by the Rule of Mixtures for the alloy, the porosity of the green bodies ranges from 22.5-25.5% and that for the sintered compacts 10.1 to 22.9 %. A summary of % theoretical density for all compositions studied in the present work using 500MPa is provided later in a separate section on sintering.

### 4.3 Delubrication and Dimensional Change

As noted in the Methods section previously all samples were subjected to a delubrication step (400<sup>0</sup>C; 30 min) prior to sintering. The temperature and time were chosen based on previous work by Akinlade et al [28].

A dimensional analysis was also performed on selected samples; results are given in Table 2 and Figure 29 where overall length (OAL) is defined as the direction of uniaxial pressure during compaction.

Table 2 - Dimensional changes for the TAY, TAS and TAYS samples from green body to de-lubricated.

Material		OAL	Length	Width
TAYS		-0.20%	0.01%	0.00%
TAY		-0.28%	0.05%	-0.02%
TAS		-0.15%	0.05%	-0.01%



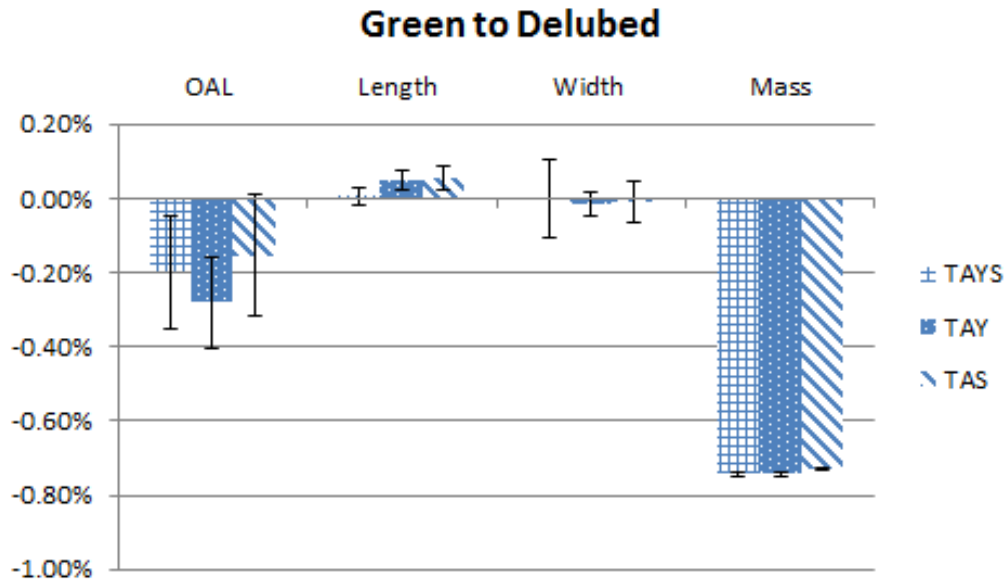


Figure 29 - Dimensional change for TAY, TAS and TAYS using "new Al" from green body to delubricated.

The sintered samples that contained both Si and Al showed more shrinkage when compared with all other compositions (Tern, TA, TAY). This is due to a combination of small 7.2 $\mu\text{m}$  Al with the small 3.9 $\mu\text{m}$  Si. This was mentioned in section 4.1.2 and was proven by German in Powder Metallurgy Science [16] in the fact that small particles will show a better sintering response due to a higher percentage of surface area contact. It should be noted that all samples shown in this study and used for oxidation testing were produced using this 7.2 $\mu\text{m}$  Al.

#### 4.4 Modeling Using JMatPro

A JMatPro model for this system is shown in Figure 30 for a composition that contained the ternary + 6Al. From the diagram there are two main features of interest in the present work. First, the solutionizing temperature for gamma prime is predicted to occur at  $\sim 1050^{\circ}\text{C}$  and second the onset of melting for a TA sample is predicted to be at  $\sim 1392^{\circ}\text{C}$  with complete melting occurring at  $\sim 1408^{\circ}\text{C}$ .

From this information a sintering temperature of 1300<sup>0</sup>C was chosen to avoid any liquation. As well, the solutionizing temperature of 1200<sup>0</sup>C was used as a guide in subsequent heat treatment experiments.

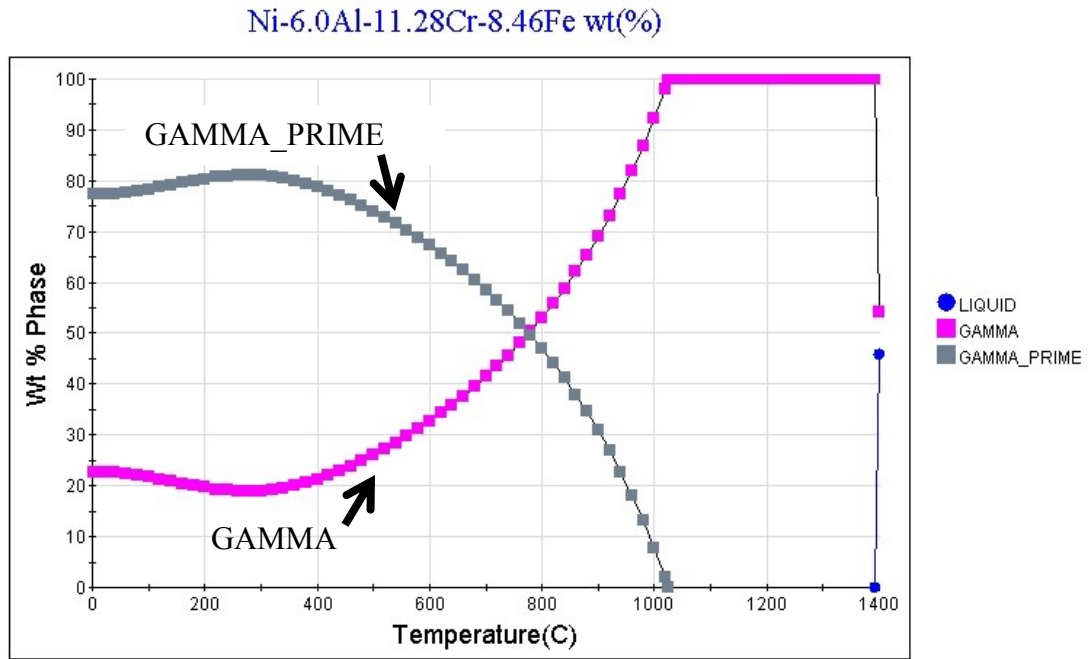


Figure 30 - Step Calculations for ternary-6Al alloy (TA).

A CCT diagram was also created for this composition which is shown in Figure 31. From this diagram the model predicted the presence of 25 v/o gamma prime on cooling at 10<sup>0</sup>C/min from sintering temperature to room temperature. This value will be addressed later via an evaluation of volume fraction precipitates using the SEM.

## CCT Nickel Based Superalloy

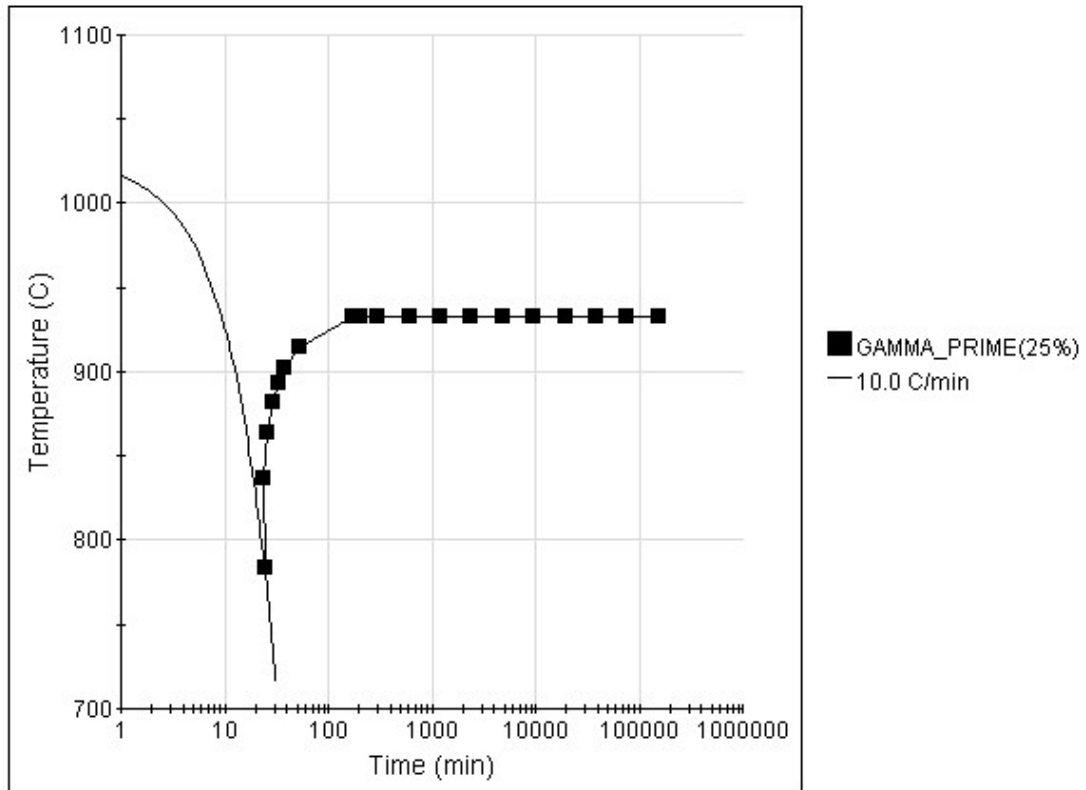


Figure 31 - JMatPro CCT diagram for the TA alloy.

Modeling was then undertaken for the ternary-6Al-0.5Si composition. The step calculation for this composition can be seen in Figure 32. For these calculations, carbon was eliminated from the model because no evidence was found in any micrographs to indicate the presence of carbides, suggesting that the carbon found via the Leco analysis by Akinlade [28] was in fact due to lubricant used to obtain the drill turnings referred to earlier.

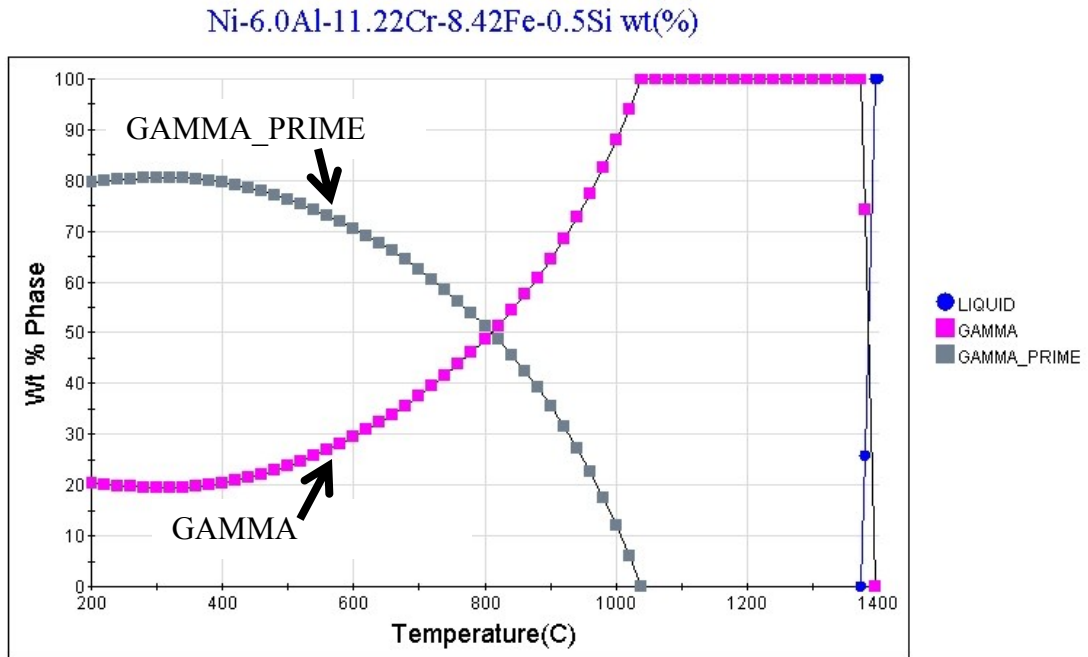


Figure 32 - Step temperature calculations for the TAS composition.

The liquation of the  $\gamma$  matrix begins at a higher temperature for the ternary-6Al (~1392°C) than the ternary-6Al-0.5Si system (~1372°C) and this is depicted in Figure 33 and Figure 34.

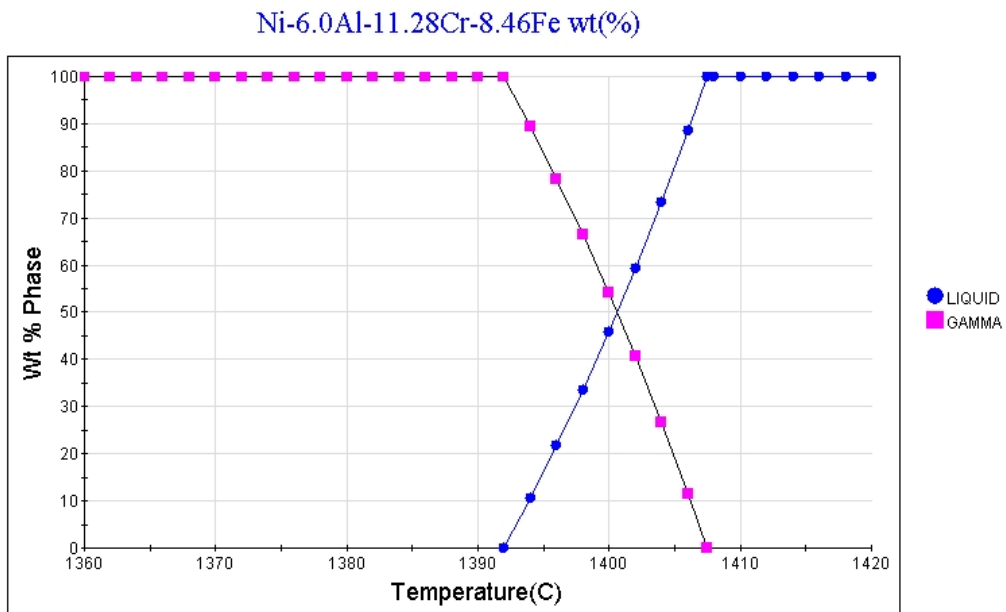


Figure 33 - JMatPro model of liquation of TA between 1392°C and 1408°C.

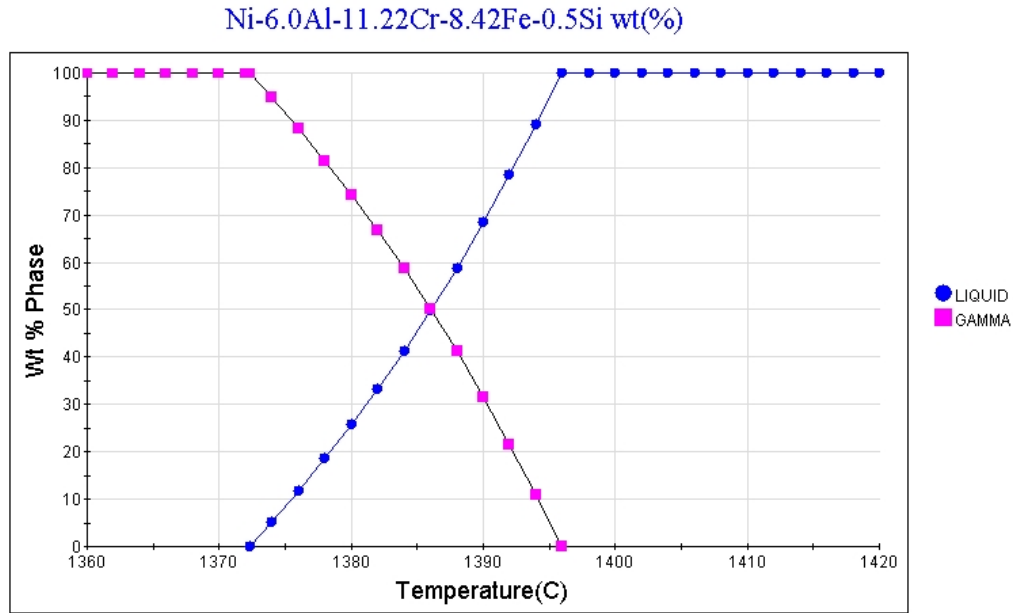


Figure 34 - JMatPro model of liquation of TAS between 1372°C and 1396°C.

The addition of even small amount of elements to alloy systems would be expected to drop the melting point slightly so this result is logical.

Next the CCT diagram was created for the ternary-6Al-0.5Si system shown in Figure 35. As noted earlier this model (TAS) does differ from the ternary-6Al system (Figure 31) in that the gamma prime appears to form at approximately 100°C sooner (lower temperature) than in the ternary-6Al CCT diagram. These predictions will subsequently be investigated when a microstructural examination is carried out on the two compositions because the ternary-6Al-0.5Si sample should, by this model, have larger precipitates since they formed earlier and would therefore have more time to grow.

## CCT Nickel Based Superalloy

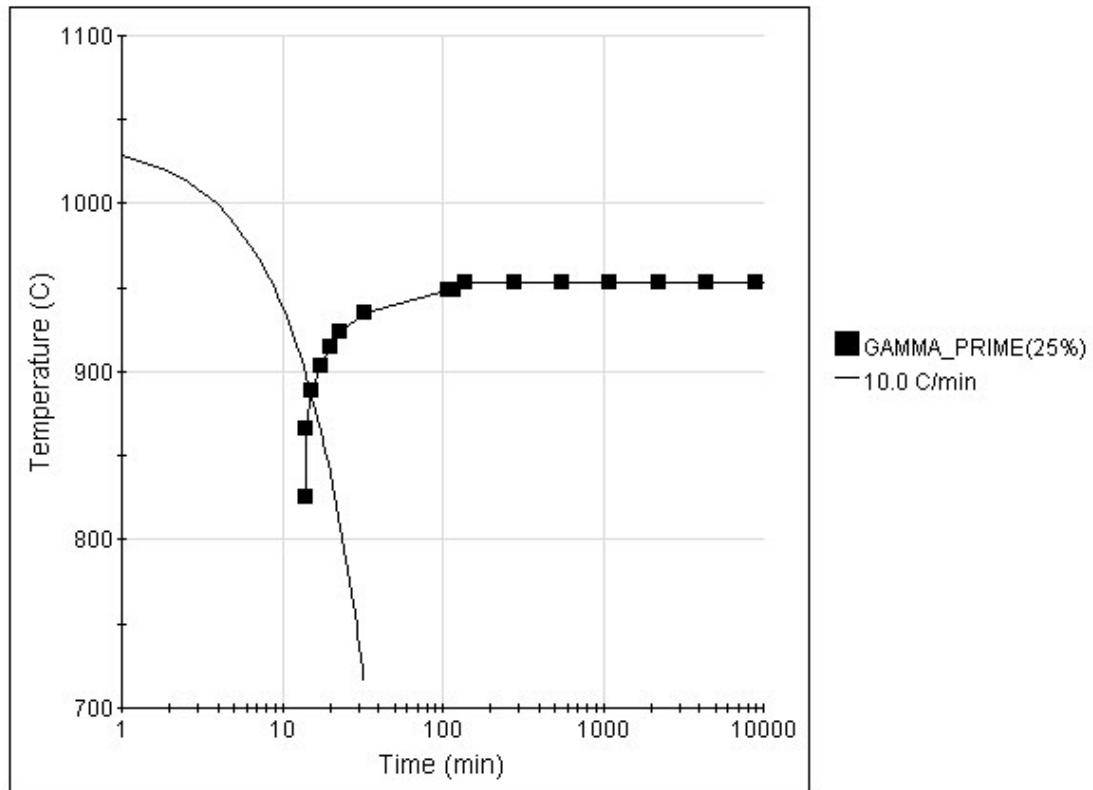


Figure 35 – JmatPro CCT diagram for the TAS alloy

As noted earlier a pilot study was undertaken to evaluate the possible benefits on microstructure of adding Ti, a second intermetallic forming element, to a TA sample. Representative SEM micrographs can be found in Figure 36 (Murray et al.) [29].

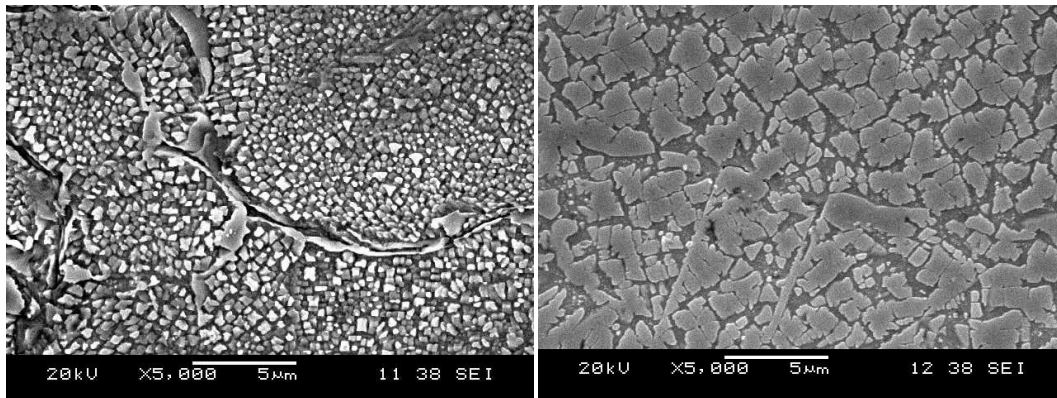


Figure 36 - SEM micrographs of the TA sample (left) and TAT (right) [29].

It is clear that the ternary-6Al-3Ti sample (TAT) contains gamma prime precipitates that are much larger than in the ternary-6Al sample (TA). A CCT diagram of the TAT sample is shown in Figure 37.

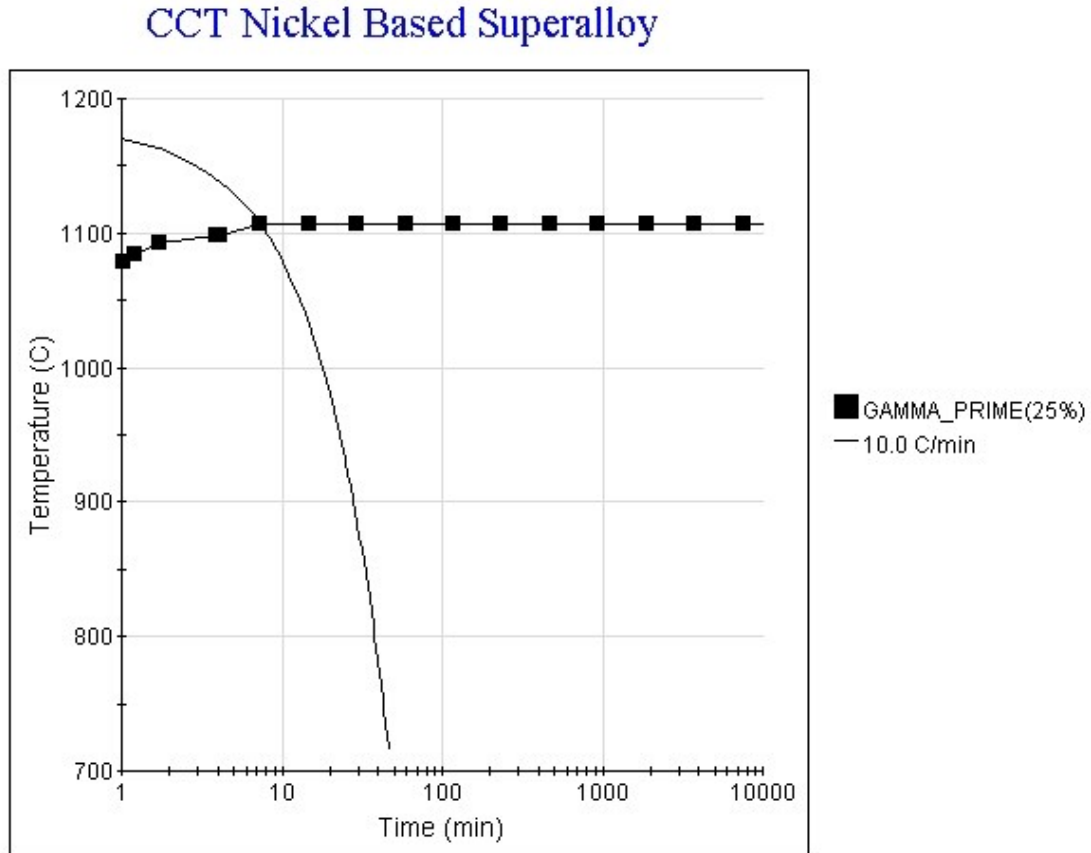


Figure 37 - JMatPro model of the CCT diagram for the TAT alloy.

By comparing the modeled CCT diagrams for the TA and TAT, an explanation can be offered for these differences of precipitate size. The gamma prime in the TAT system was predicted by JMatPro to form at a much higher temperature than the TA composition. This would allow more time for the  $\gamma'$  precipitates to grow in the ternary-6Al-3Ti sample, therefore meaning they should be of a larger size than the composition without Ti.

These results are instrumental in understanding subsequent precipitate size found in the TA vs. TAS systems in the present work.

## 4.5 Differential Scanning Calorimetry

Prior to sintering, TA and TAS samples were subjected to a DSC analysis between room temperature and 1300<sup>0</sup>C. This was to supplement the JMatPro predictions on solutionizing temperature and onset of melting, primarily to ensure that no liquation occurred in the Bell furnace on sintering. A detailed DSC study on the TA composition was reported previously by Akinlade et al [41]. Therefore in the present work the intent was to replicate the TA spectra regarding thermal events and then provide a comparison with the TAS samples in the present investigation. It was assumed that because of the small amount of Y in the TAY and TAYS compositions that the resulting DSC spectra would be similar to the TAS.

Representative traces for TA and TAS are given for heating and cooling (2.5<sup>0</sup>C/min) in Figure 38 and Figure 39. The presence of the 0.5 w/o Si modified the exothermic reactions in the system by lowering the temperature at which the exothermic reaction occurred. This was thought to coincide with an aluminium silicon eutectic though this was not studied in depth in the present work. The Si addition also played a major role in increasing the major exothermic event which peaked at 1277<sup>0</sup>C for the TAS system; however, further examination of this event was beyond the scope of this work.



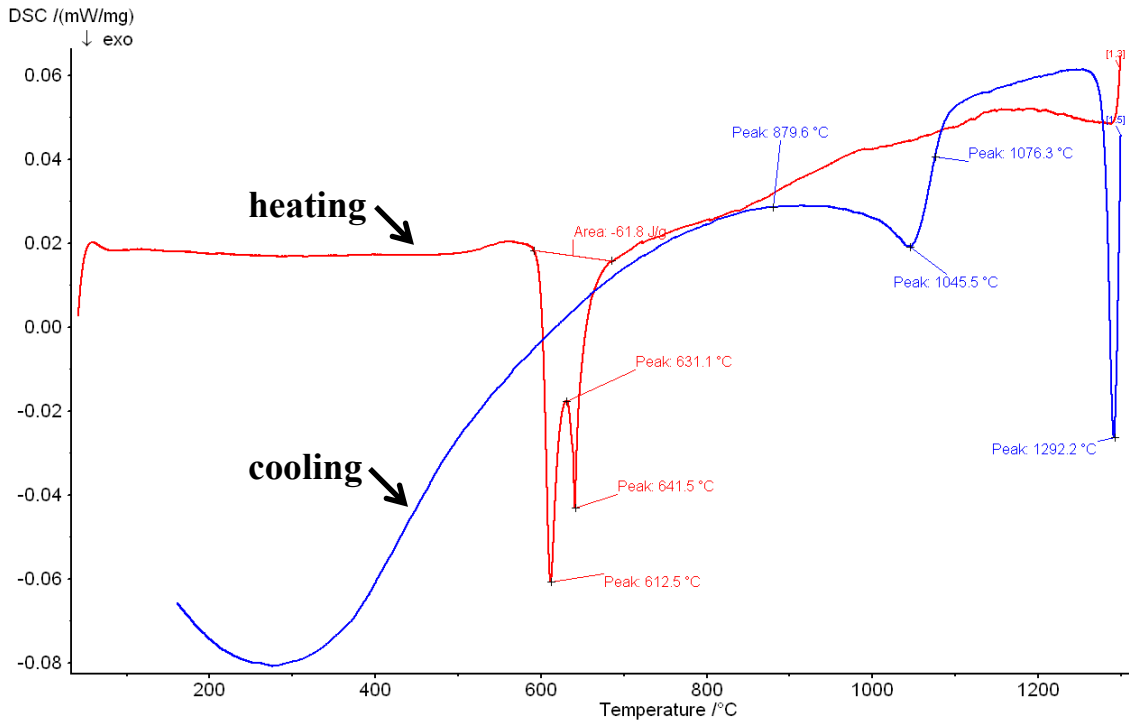


Figure 38 - DSC trace for TA on heating and cooling up to 1300°C (2.5°C/min).

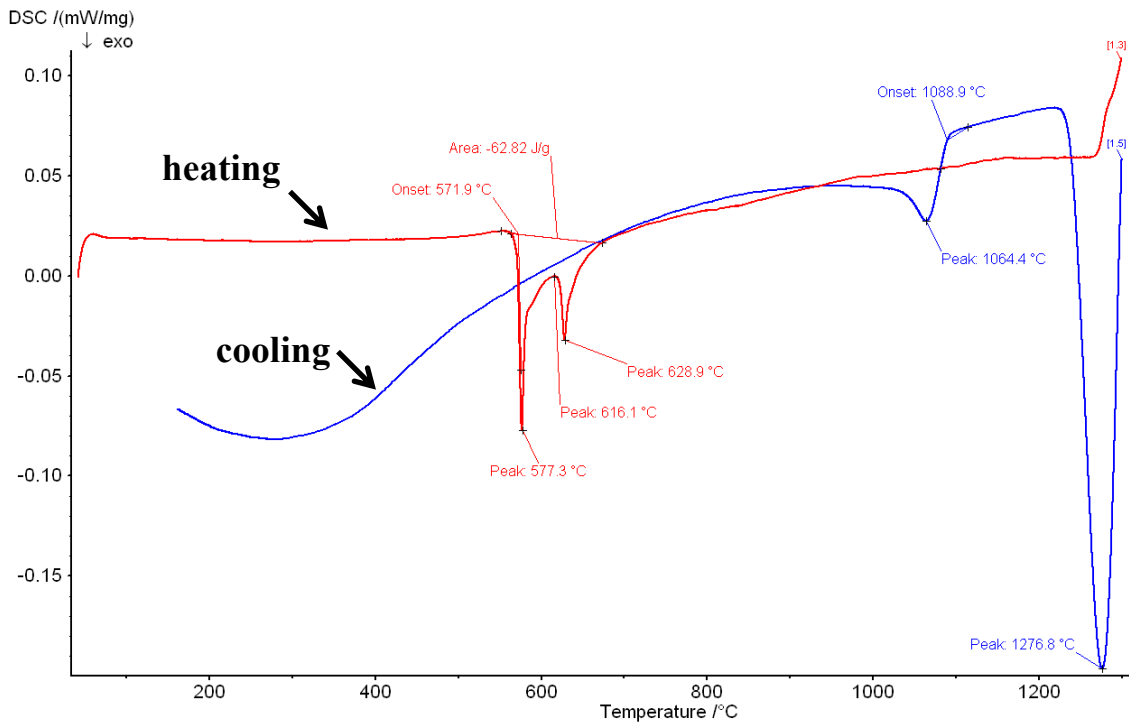


Figure 39 - DSC trace for TAS on heating and cooling up to 1300°C (2.5°C/min).

## 4.6 Sintering

Following sintering all samples were subjected to an examination of sintered density (% theoretical), hardness evaluation (used as a measure of presence of gamma prime) and dimensional change.

### 4.6.1 Hardness

The hardness values of the as sintered samples are given in Figure 40.

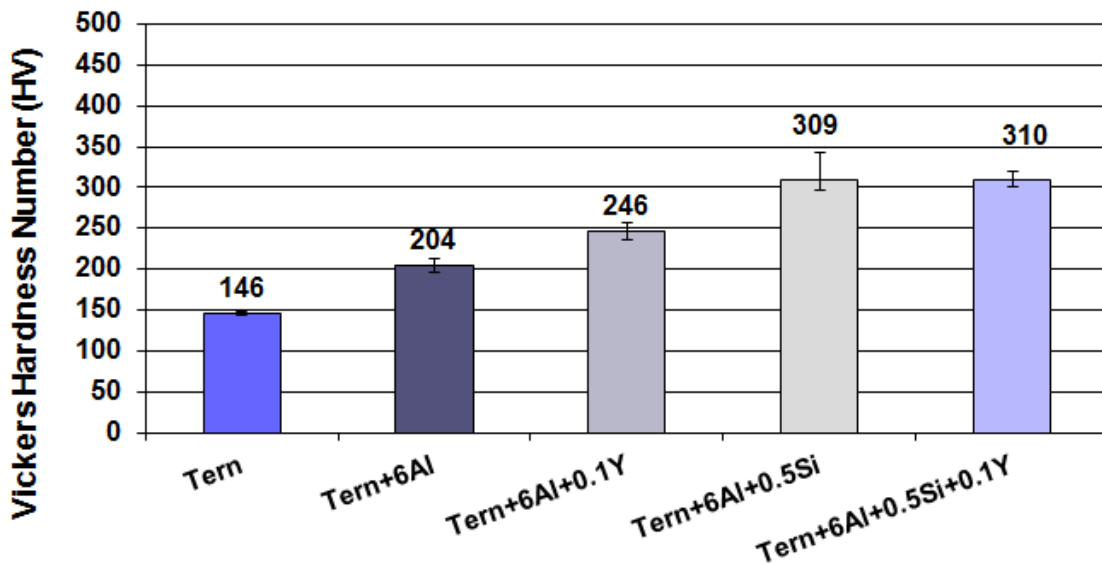


Figure 40 - Hardness values for the alloys produced.

The hardness data in Figure 40 show that the additions of Y and Si, alone or in combination will increase the hardness of these alloys which contain aluminum. The increased hardness is also an indication of the gamma prime ( $\gamma'$ ) phase existing in the microstructure. This would be due to the increased percentage of gamma prime that would be precipitated with minor additions of reactive elements to the  $\gamma'$  forming alloys. This will be reviewed when the microstructural analysis is presented and discussed in Section 4.6.4

#### 4.6.2 Percent Theoretical Density (Porosity)

Figure 41 shows the density comparisons of the alloys after sintering.

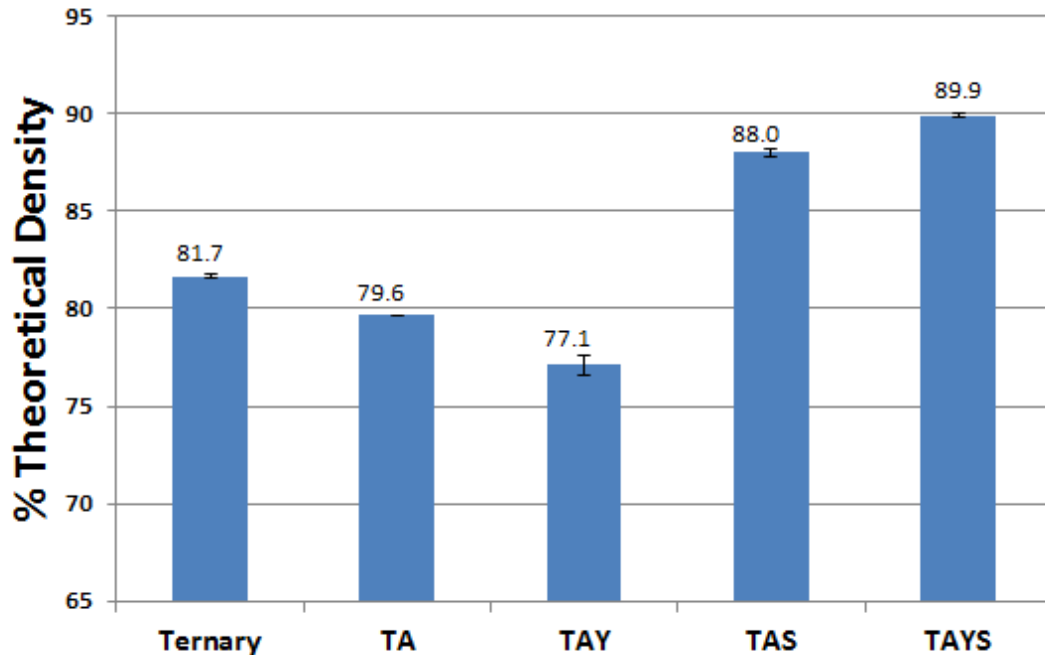


Figure 41 – Density comparison of the alloys after sintering

It is clear from Figure 41 that there existed some major differences in % theoretical densities between the various compositions, with samples containing both aluminum and silicon (TAS, TAYS) far less porous than the other three, namely ternary, TA, or TAY. In previous studies by Murray et al [42], the densities of samples containing an older aluminum with a  $d_{50}$  of  $15.7\mu\text{m}$  only achieved densities similar to the other compositions (~80% theoretical), however, in this thesis the “new Al” with a  $d_{50} = 7.2\mu\text{m}$  was used throughout. The increased surface area contact between the two smallest constituents within the TAS and TAYS alloy systems would facilitate an increase thermodynamic drive towards the reduction in free energy in the system. This agrees with well recognized principles outlined by German in Sintering Theory and Practice (pgs. 232-234). Another possible explanation is the hydration of the “old” aluminum powder which would reduce the sintering response of the alloys.

### 4.6.3 Dimensional Change

The sintered samples in the present study that contained both Si and Al showed more shrinkage when compared with all other compositions (Tern, TA, TAY). This is due to a combination of small  $7.2\mu\text{m}$  Al with the small  $3.9\mu\text{m}$  Si. This was mentioned in section 4.1.2 and again is because small particles will show a better sintering response due to a higher percentage of surface area contact. The results from dimensional change from green to sintered bodies are given in Table 3 and Figure 42.

Table 3 – Dimensional change from green to sintered state

Material	OAL	Length	Width
TAYS	-4.34%	-5.12%	-4.94%
TAY	-0.03%	-0.94%	-1.24%
TAS	-3.72%	-5.03%	-4.79%

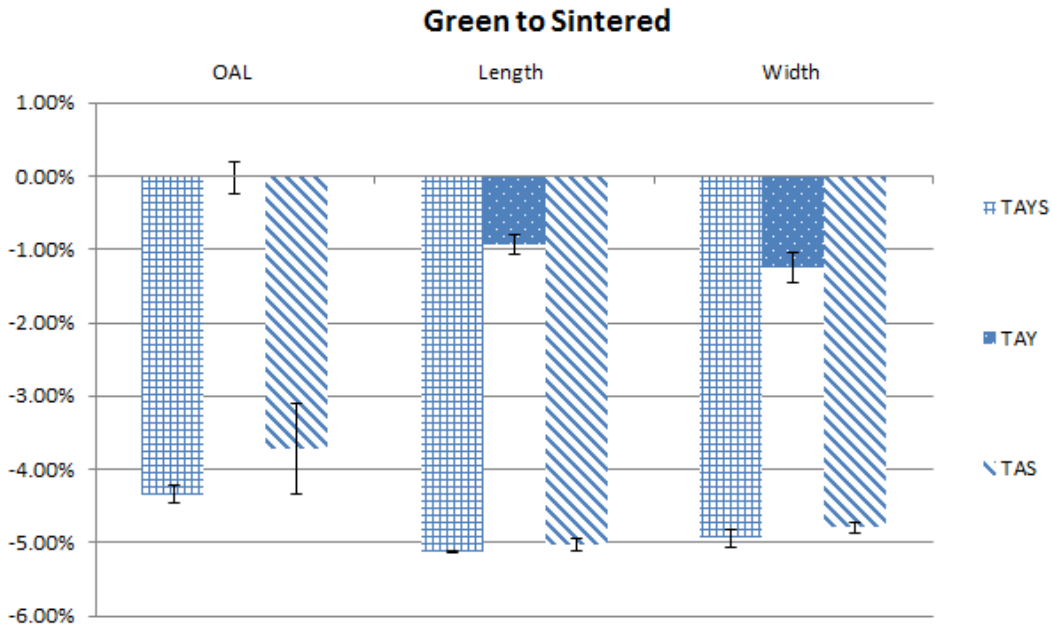


Figure 42 - Dimensional change for TAY, TAS and TAYS from green body to sintered state.

The results from Table 3 and Figure 42 indicate that there was much more shrinkage with the samples that contained both Al and Si together. Since the porosity is lower in the TAYS and TAS samples this result makes sense. These results indicate that there was

proof that there was a higher degree of bulk transport mechanisms operating in these alloy systems when compared with the T, TA, or TAY systems. This will be discussed further in Section 4.6.4.

#### 4.6.4 Microstructure (as sintered)

The microstructure of all alloys post-sintering was very similar as would be expected from using the same production technique and minor variations in composition. Figure 43 shows the TA and TAS in the as sintered conditions after etching with the  $\gamma'$  etchant.

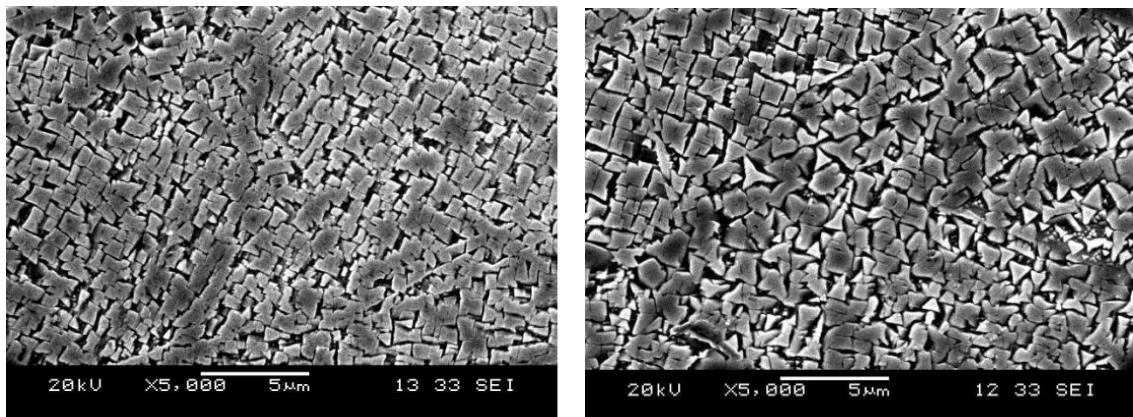


Figure 43 - TA (left) and TAS (right) in the as sintered condition.

It is seen in Figure 43 that the TA and TAS samples had similar-sized precipitates although JMatPro predicted the  $\gamma'$  in TA to be slightly smaller. Both had similar microstructures, containing primarily cuboidal  $\gamma'$  precipitates in a  $\gamma$  matrix. Similar results are shown in Figure 44 where the  $\gamma'$  precipitates were formed at a higher temperature in the sample containing the aluminum, silicon and yttrium (right) compared to the sample containing just aluminum and yttrium (left).

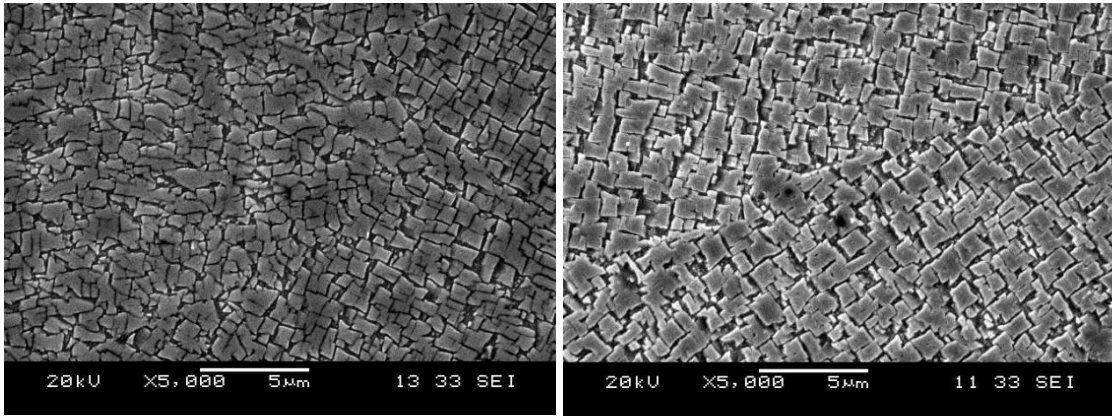


Figure 44 - TAY (left) and TAYS (right) in the as sintered condition.

## 4.7 Porosity Reduction

Because of the effect of porosity on eventual oxidation studies (more open porosity would lead to enhanced oxidation) and with reference to differences in sintered sample porosity noted in Section 3.6.2 a method was needed to normalize final % theoretical density. A Gleeble thermo-mechanical approach (hot deformation) was presented earlier as a potential method to reduce/normalize porosity. Prior to Gleeble testing a temperature must be selected in order to bring all of the brittle gamma prime precipitates into solution prior to deformation. For wrought Ni-based Superalloys the temperature at which the  $\gamma'$  is reported to go into solution is about 1175°C [2]. A diagram from Donachie's *Superalloys: Source book* [20] suggests that this may be slightly higher as seen in Figure 45.

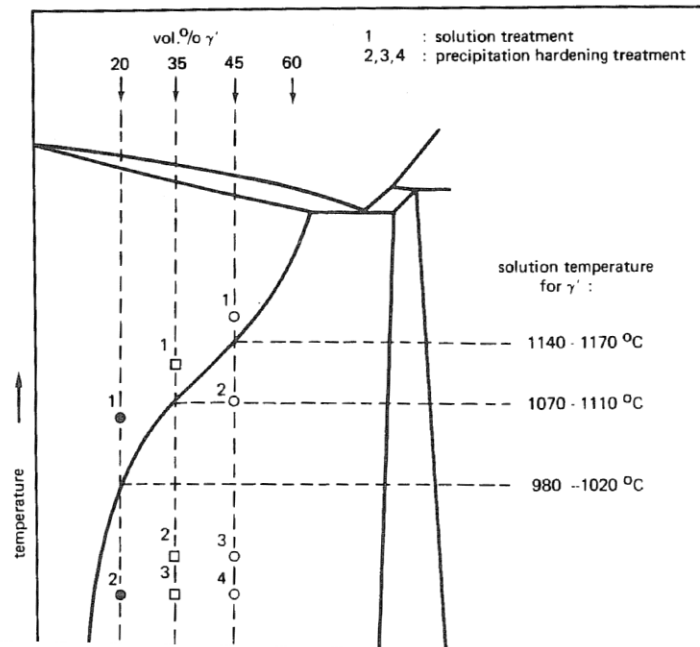


Figure 45 - Solutionizing treatment for wrought Ni-based Superalloys vs. vol% gamma prime [20].

Interestingly, JMatPro predicted a solutionizing temperature of  $\sim 1050^{\circ}\text{C}$  and the DSC work in Section 4.5 a temperature of  $1050^{\circ}\text{C}$  as well.

Considering these aspects and wishing to ensure full solutionizing without liquation a temperature of  $1200^{\circ}\text{C}$  was chosen.

Results in the form of percent theoretical density for all five compositions (T, TA, TAS, TAY and TAYS) in the as sintered and post-Gleeble deformed condition are given in Figure 46.

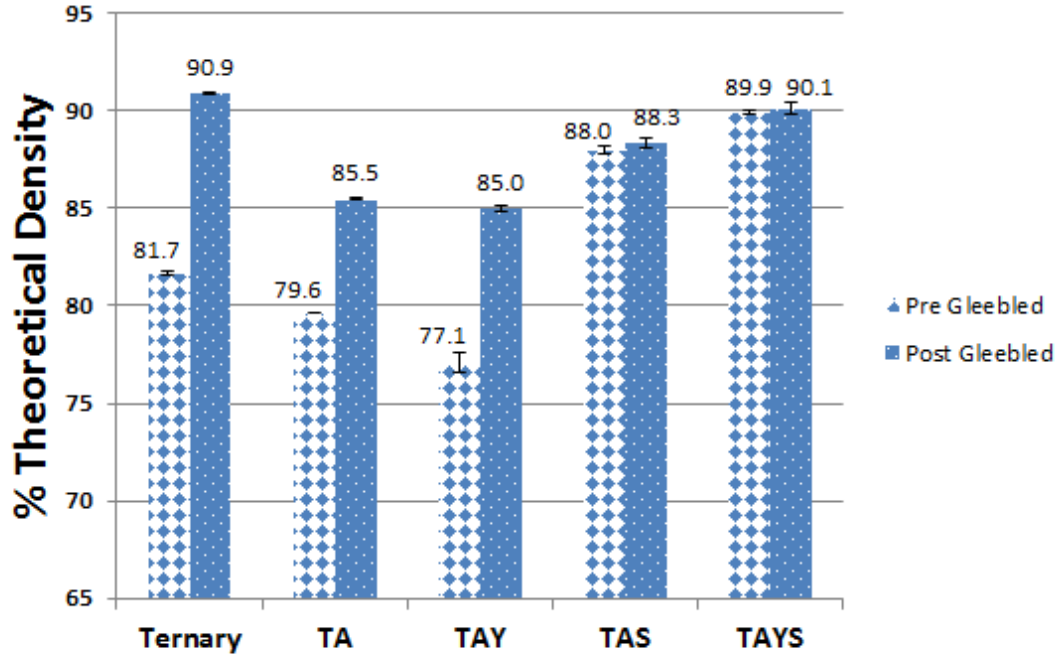


Figure 46 – Percent theoretical densities for all five compositions in the as sintered (left) and post (right) Gleeble deformed conditions.

From Figure 46 it can be seen that the final residual porosity was of the order of 10 - 15 v/o; therefore, although the hot-deformation step did not eliminate porosity it did succeed in providing samples with similar porosity for oxidation testing. Therefore any differences experienced by the samples during oxidation testing should be a function of composition (additions of Si and/or Y) and not microstructure.

## 4.8 Heat Treatment

Heat treated/hot deformed (Gleeble) samples were characterized in terms of microstructure and hardness prior to oxidation testing. Heat treatment was a necessary step to restore the visible gamma prime (at 10,000x magnification), to the microstructure. Having  $\gamma'$  in the microstructure helps ensure rapid formation of a dense alumina/spinel oxide layer at the surface of an oxidizing sample due to an increase in the local concentration of aluminum available to be oxidized. This heat treatment was carried out



under high vacuum ( $10^{-6}$  torr) in an attempt to minimize the oxidation of the samples prior to oxidation testing. Initially select samples were heat treated at  $750^{\circ}\text{C}$  for one hour with no noticeable change in microstructure or hardness. A heat treatment of  $950^{\circ}\text{C}$  was then attempted with a hold time of four hours. The latter heat treatment resulted in a re-emergence of the  $\gamma'$  precipitates ( $0.3\mu\text{m}$ ), though they were noted to be much smaller than in the as sintered condition of  $1\mu\text{m}$ .

#### 4.8.1 Microstructure

Figure 47 is a micrograph of an unetched ternary sample post Gleeble hot forging. The image used EDS mapping and helped to ensure that there was no contamination from the Ta foil into the samples once they were forged.

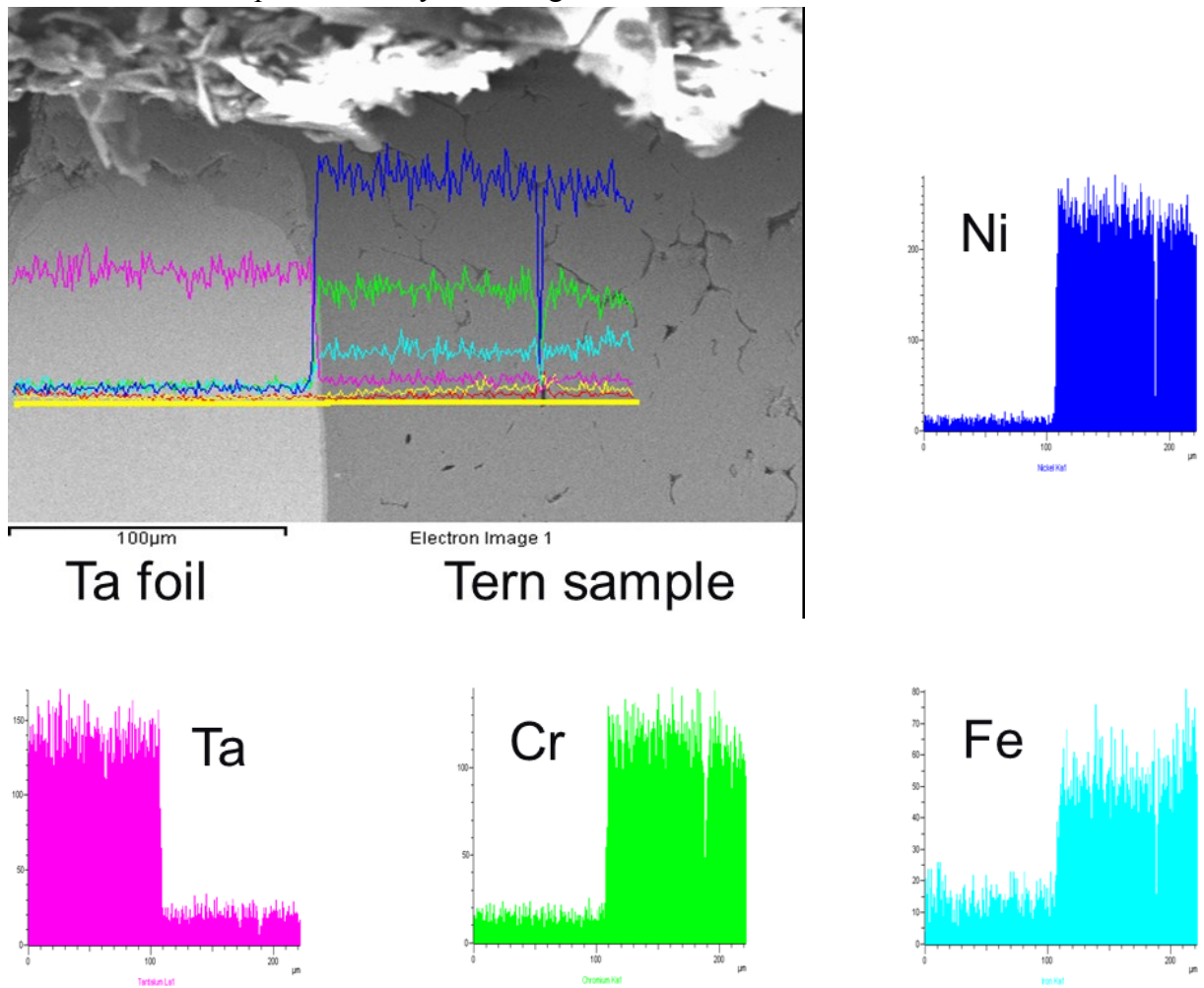


Figure 47 - An SEM-EDS mapping of the Ta foil still attached to a ternary sample after a Gleeble hot forge reduction of 30%.

From Figure 47 it is evident that there was no elemental cross-over or contamination of the sample after a 1min hold at 1200°C followed by a 30% reduction through uniaxial deformation. This is important as it ensures that any effects seen during heat treatment or oxidation will not have been a result of any diffusion of Ta into the alloys.

Figure 48 and are representative SEM micrographs of samples post Gleeble and post heat treatment. All samples were etched with  $\gamma'$  etchant. As may be expected, the microstructures were similar, with gamma prime precipitates and residual porosity evident. There was no visible oxidation on the samples prior to oxidation testing.

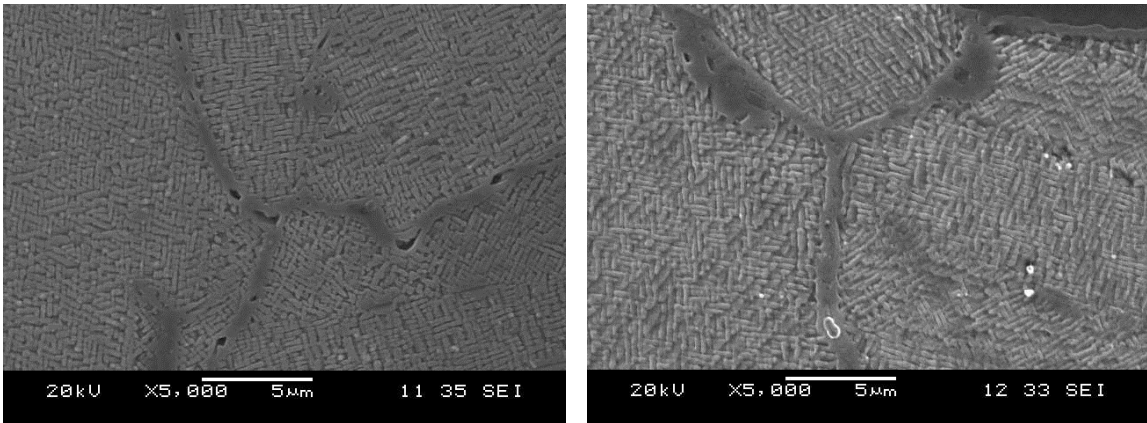


Figure 48 - TA (left) and TAS (right) in the Gleeble hot-deformed and heat-treated condition.

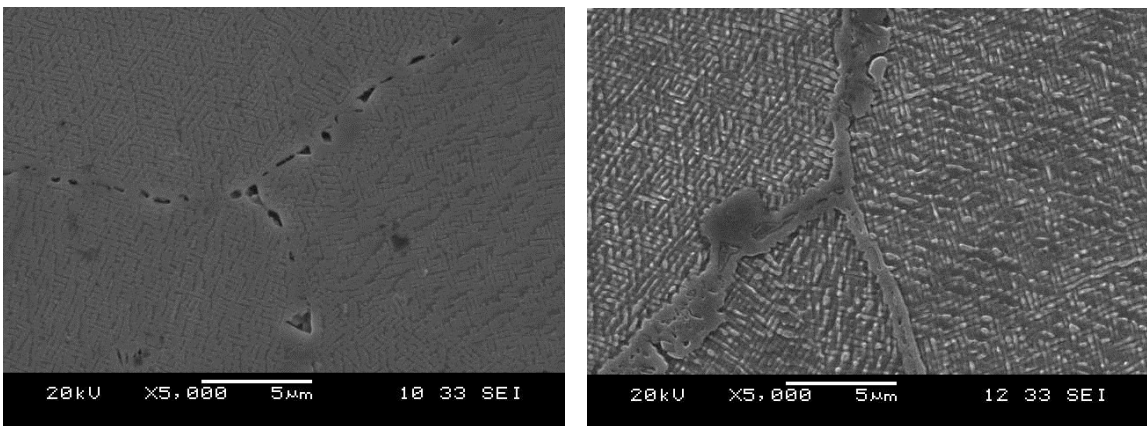


Figure 49 - TAY (left) and TAYS (right) in the Gleeble hot-deformed and heat-treated condition.

Figure 48 and show that there is a re-emergence of the gamma prime precipitates post Gleeble hot deformed coupled with a heat treatment of 950°C with a four hour hold. In the micrographs at 5,000x magnification all compositions have precipitates in the range of 0.3µm. This differs from the 1µm precipitates noted as sintered condition (pre-Gleeble deformed). A comparison of the %  $\gamma'$  and size of the precipitates in the as sintered and post Gleeble deformed conditions is given in Table 4.

Table 4 - Percent  $\gamma'$  and precipitate size in the as sintered and post Gleebled and heat treated conditions.

Sample	Condition	Volume % $\gamma'$	$\gamma'$ Size (µm)
TA	As Sintered	61.7 ± 3.2	1 ± 0.2
TAY	As Sintered	58.3 ± 3.2	1 ± 0.2
TAS	As Sintered	61.7 ± 3.2	1 ± 0.2
TAYS	As Sintered	60 ± 3.2	1 ± 0.2
TA	Gleebled and Heat treated	58.3 ± 3.2	0.3 ± 0.1
TAY	Gleebled and Heat treated	60 ± 3.2	0.3 ± 0.1
TAS	Gleebled and Heat treated	61.6 ± 3.2	0.3 ± 0.1
TAYS	Gleebled and Heat treated	58.3 ± 3.2	0.3 ± 0.1

#### 4.8.2 Hardness Tests

Unlike the results shown in Figure 40, Section 4.6.1, there was significant scatter in the values obtained. Specifically, VHN had ± values of 35VHN for alloys with the same composition and in the same state (Gleebled, or Gleebled and heat treated). Therefore hardness measurements were not instructive in determining any differences in gamma prime formation based solely on sample fabrication history. This scatter was probably due to variations in % theoretical density or density gradients within individual samples following hot deformation that would lead to differing values depending on location, such as proximity to the anvils.

## 4.9 X Ray Diffraction (XRD)

Samples were also subjected to XRD, primarily to determine presence/absence of gamma prime and/or other intermetallic species or mineralogical occurrences such as spinels.

Representative spectra for the TAYS alloys are given in Figure 50 in sintered, Gleebled and Gleebled + heat treated states.

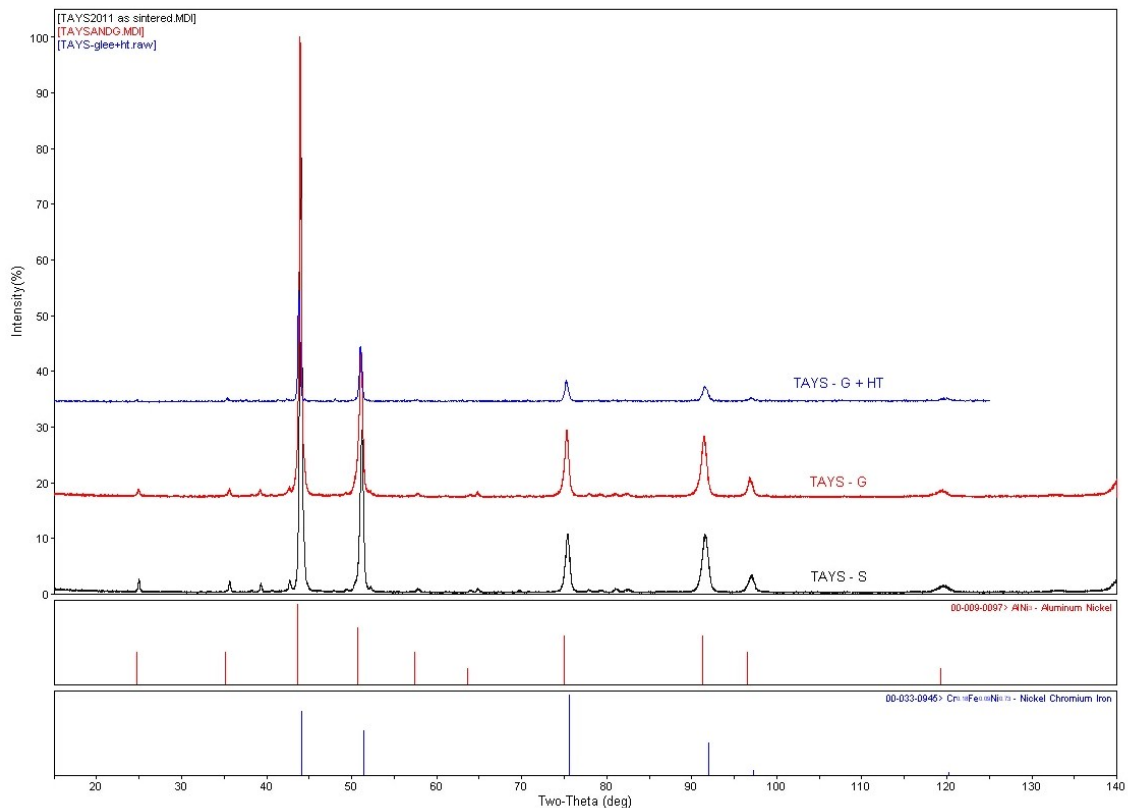


Figure 50 – XRD spectra for the TAYS sample in the sintered (S), Gleebled (G) and Gleebled + heat treated (G + HT) conditions.

As can be seen, Ni<sub>3</sub>Al (gamma prime) was present in all conditions as well as the gamma matrix that encases these precipitates. Therefore, although the hot forging managed to reduce porosity in most compositions (Section 4.7; Figure 46) the persistence of gamma prime suggests that none of the Gleebled samples had been solutionized. This is contrary to reported literature [1] [20] as well as the JMatPro predictions and the DSC results.

Subsequent attempts to water quench a TA sample did not change the resulting microstructure, suggesting that either the presence of porosity and prior particle boundaries inhibited the solutionizing process or that secondary gamma prime formed extremely rapidly on cooling. Bearing in mind that the precipitates post Gleebled and heat-treatment were about one-third the size of those as-sintered suggests the latter to be the likely reason.

## 4.10 Oxidation Testing

Results for the oxidation tests are given in graphical form in Figure 51, Figure 52 and Figure 53 for all four compositions for times up to 1000h at 900<sup>0</sup>C.

### 4.10.1 Weight Gain as a Function of Time

A complete set of the data collected from the oxidation tests performed is shown in Figure 51. It is evident that there is one outlier during the early stages of oxidation testing. This oxidation time was subsequently repeated and fell within the range of the other data.

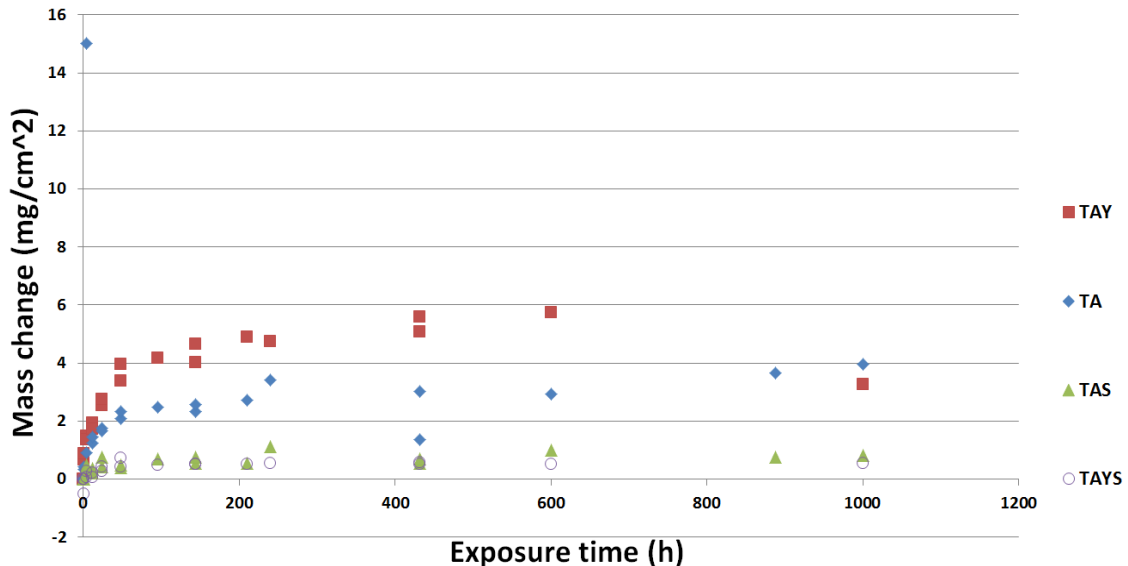


Figure 51 – Mass change vs. exposure time for all oxidized samples.

From Figure 51 it is evident that all alloys oxidized in a generally parabolic manner, though the compositions containing both Al and Si performed much better than those

without. Most noteworthy from Figure 51 is that the sample containing TAY performed much worse during oxidation testing when compared to the other three alloys (TA, TAS, TAYS). This result was somewhat unexpected prior to oxidation testing as the literature review showed yttrium additions in small amounts to be beneficial to the oxidation behaviour of these alloys as stated in Section 1.10.2. In particular the TAY sample spalled during long term oxidation testing thereby increasing the oxidation rate of this alloy. It also appeared that some of the samples containing yttrium had reacted with the glazed alumina crucibles that they were oxidized in. The crucibles were necessary in order to ensure that any spallation could be accounted for when verifying the masses of the oxidized samples. This problem seemed to be limited to the TAY samples.

A closer examination of the first 48 hours of oxidization is shown in Figure 52. This Figure shows even more clearly that the TAY sample oxidized much more rapidly compared to all other compositions. This could be beneficial if such an oxide was quick forming and dense, yet for this composition it did not protect the alloy any better than the ternary with the addition of aluminium.

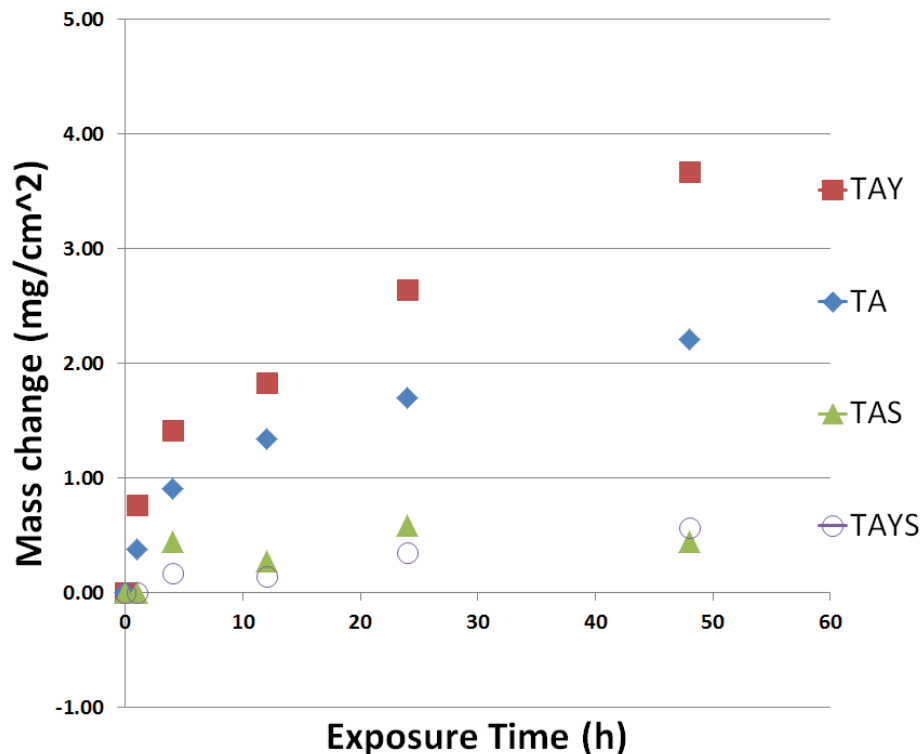


Figure 52 – Mass change vs. exposure time for the first 48 hours.

Figure 53 shows a graph with the oxidation rates for the alloys displayed using a parabolic model. It is evident that, as expected, the oxidation for all alloys shows parabolic behaviour although the fit is best for the TAS and TAYS samples. This may be due to spalling of the oxide at the longer times as noted above and/or reaction with the containment crucible noted for the TAY composition.

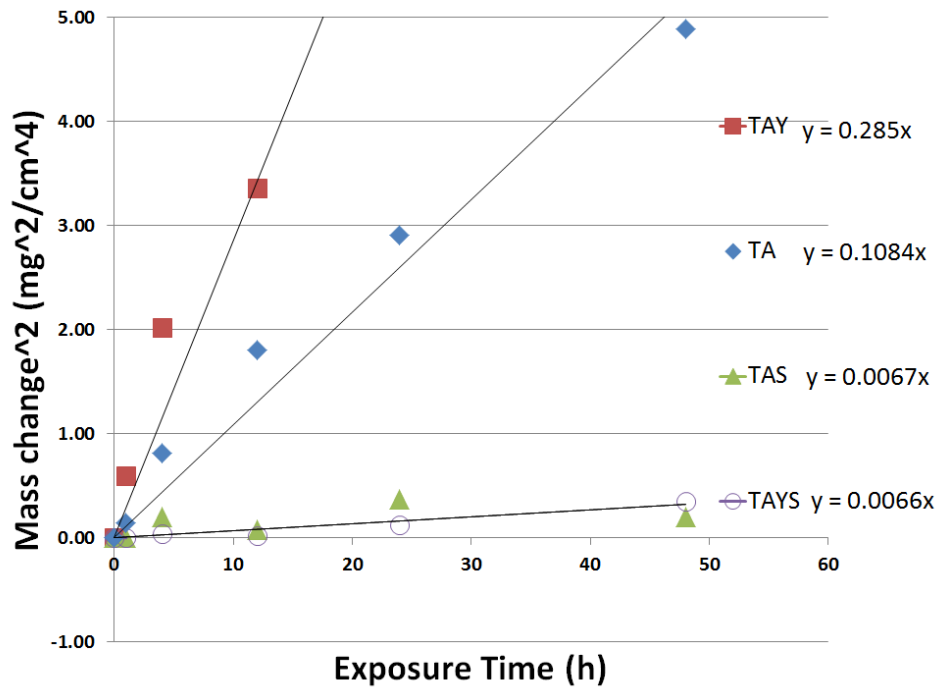


Figure 53 – Oxidation rates of the four alloys tested.

#### 4.10.2 Microscopy of Oxidized Samples

From Figure 51, Figure 52 and Figure 53 the extent of oxidation (both in mass gain/area, and rate of oxidation) was lowest for both the TAS and TAYS samples and highest for samples without Si, namely TA and TAY. Therefore, in this section TA and TAS are used to illustrate differences in microstructure; representative microstructures for the other compositions are given in Appendix A. As well, five oxidation times are presented here, namely 1, 24, 48, 144 and 432h. The remainder appear in Appendix A.

Most micrographs consist of a highly reflective oxide layer, with a precipitate free zone (PFZ) beneath, both being on the surface of the original  $\gamma + \gamma'$  matrix. Figure 54 is presented to illustrate these features; Table 5 gives an EDS analysis of the two surface features, namely the oxide layer and the PFZ.

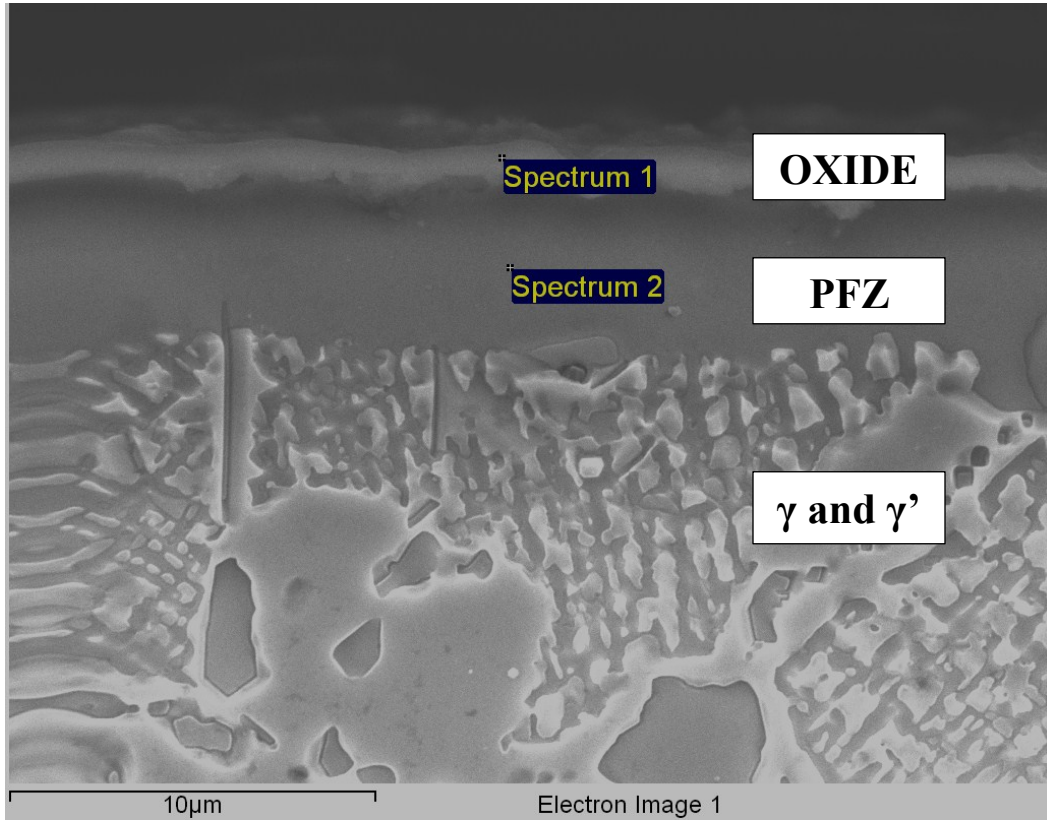


Figure 54 - TAS oxidized for 48h showing various features on the oxidized sample.

Table 5 - EDS results for the spectrum collected.

Spectrum	O	Al	Si	Cr	Fe	Ni	Total
Spectrum 1	46.7	34.6	0.6	5.5	0.9	11.7	100.00
Spectrum 2	1.7	4.4	2.5	16.2	4.8	70.3	100.00

It is clear from Figure 54 in combination with Table 5 that the highly reflective layer that appears did produce a defined oxide layer on the surface of the TAS sample. This layer was over top of a precipitate free zone which was nearly void of aluminium as this was the main element in the protective layer on the oxidized surface. Under the precipitate



free zone was a matrix of gamma intertwined with the gamma prime that had been left untouched in the substrate of the alloy.

Figure 55 and Figure 56 are micrographs of samples TA and TAS respectively, after 1h oxidation. Both samples show slight signs of depletion of  $\gamma'$  at the exposed surface (upper edge), though neither shows any signs of a distinct oxide layer.

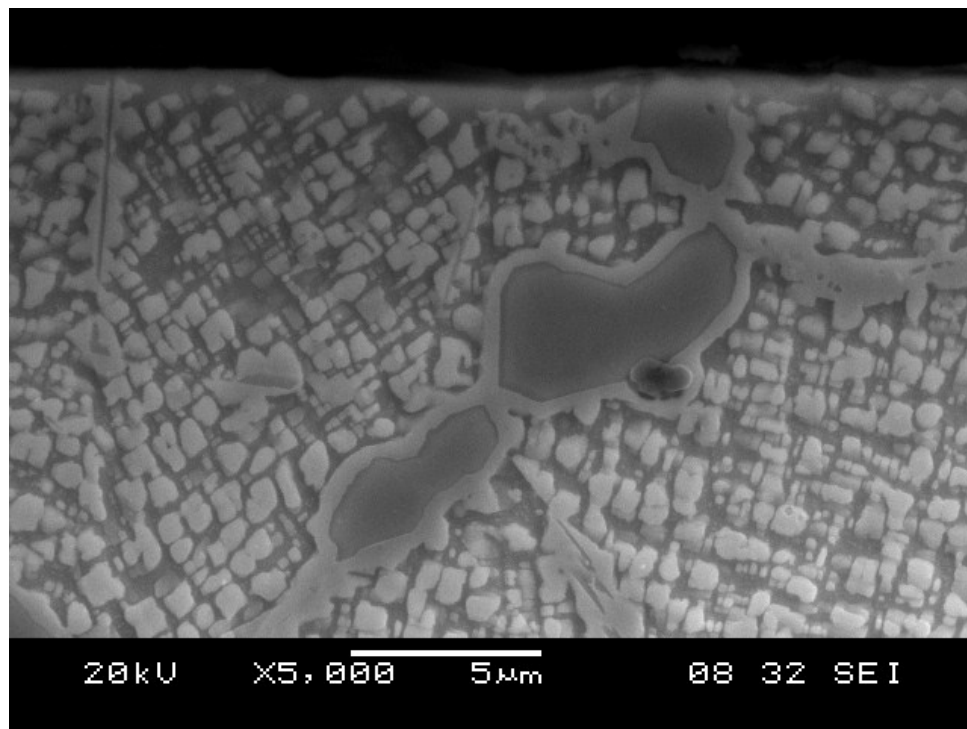


Figure 55 – Micrograph of TA after 1h oxidation.

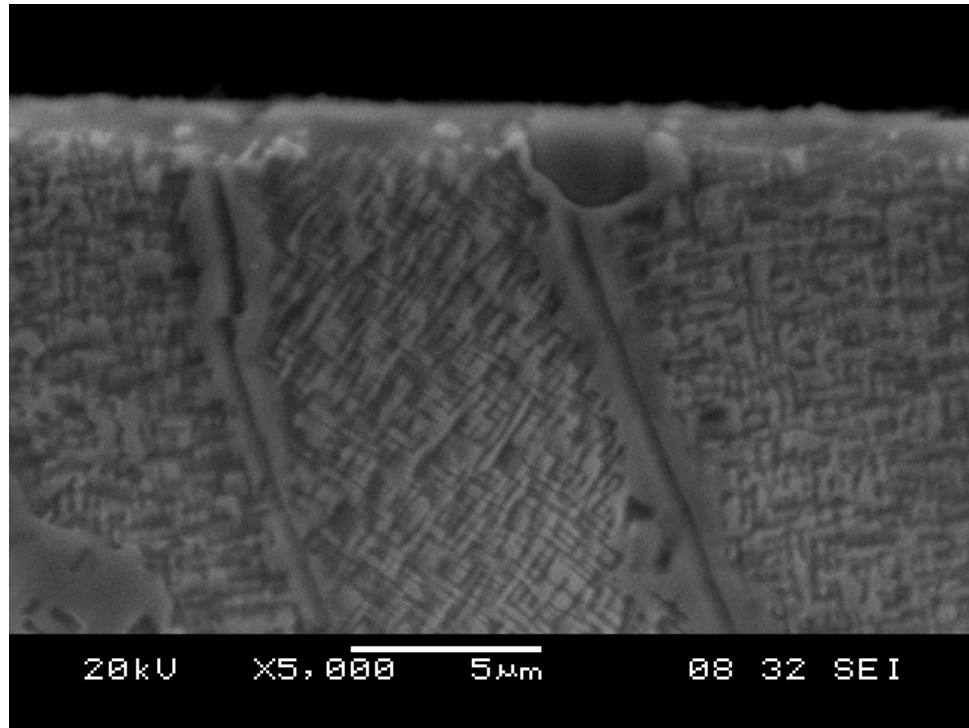


Figure 56 - Micrograph of TAS after 1h oxidation.

Figure 57 and Figure 58 show samples of TA and TAS respectively after 24h oxidation. Again, both samples are starting to show a PFZ which is just below an oxide layer that has formed (indicated by arrows in subsequent micrographs). There is a depletion of aluminum beneath the oxide layer that is forming since the aluminum has a strong thermodynamic driving force to become a stable alumina layer at 900°C at the surface of the material. The TA sample appears to be developing a much thicker precipitate free zone than the TAS sample that was oxidized for the same period of time. This is in agreement with the literature review that was performed in section 1.10 in that an addition of an alloying element can help to improve the oxidation resistance of the Ni-based alloys, though the exact mechanism that is in operation in this case is hard to define without testing by other means such as electro probe micro analysis of the oxide layer.

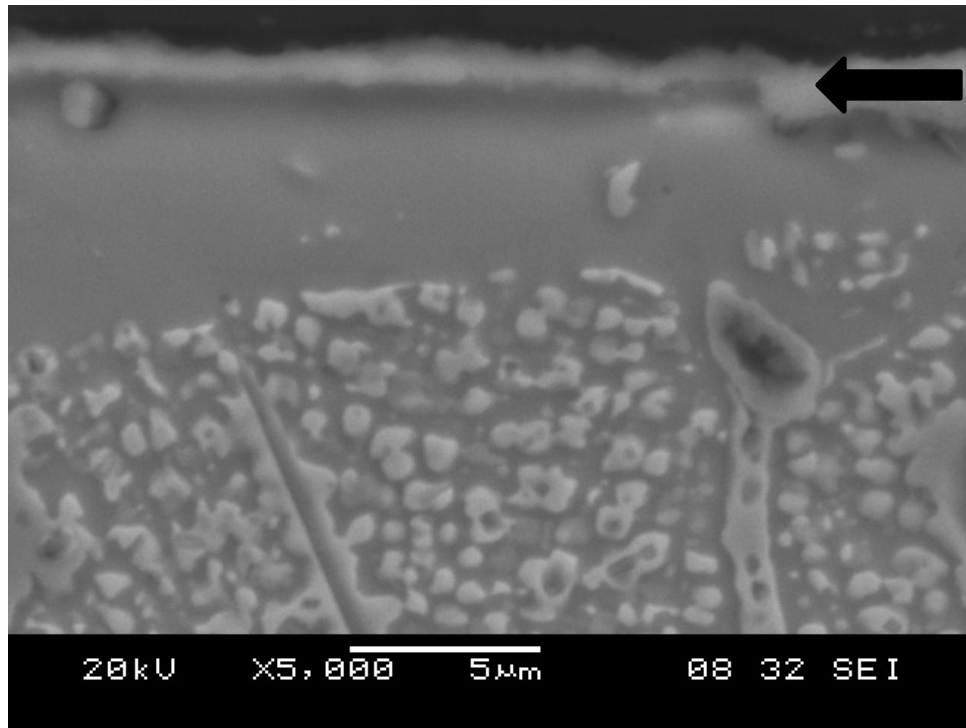


Figure 57 - Micrograph of TA after 24h oxidation.

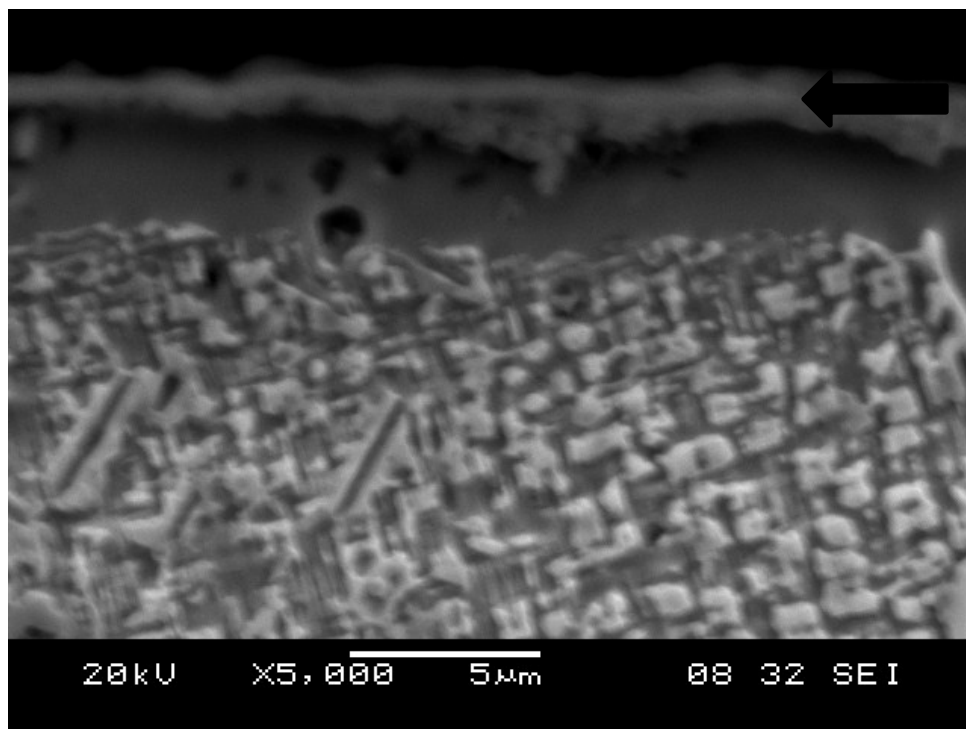


Figure 58 - Micrograph of TAS after 24h oxidation.

Figure 59 and Figure 60 show samples of TA and TAS respectively and both have been oxidized for 48 hours. A major PFZ in the area just below the oxide layer is clearly evident for the TA sample where the TAS sample looks very similar to the sample that had been oxidized for 24 hours. Also, as might be expected, the oxide layer for the TA sample in Figure 59 (oxidized 48h) is much thicker than in Figure 57 (oxidized 24h). A compilation of layer thickness is given later in Tables 6, 7, 8 and 9.

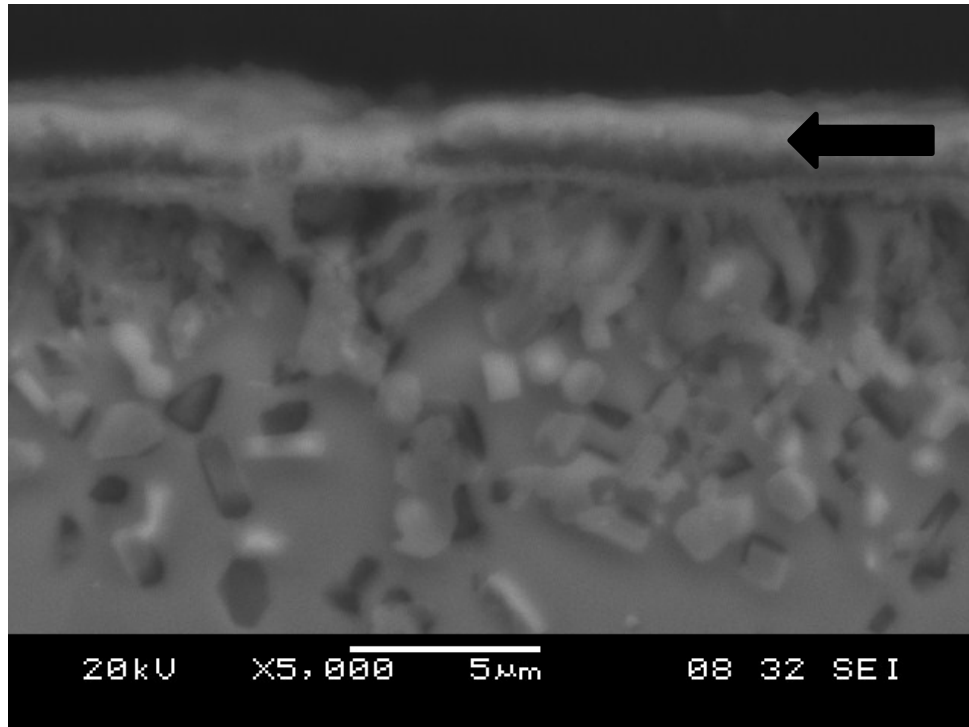


Figure 59 - Micrograph of TA after 48h oxidation.

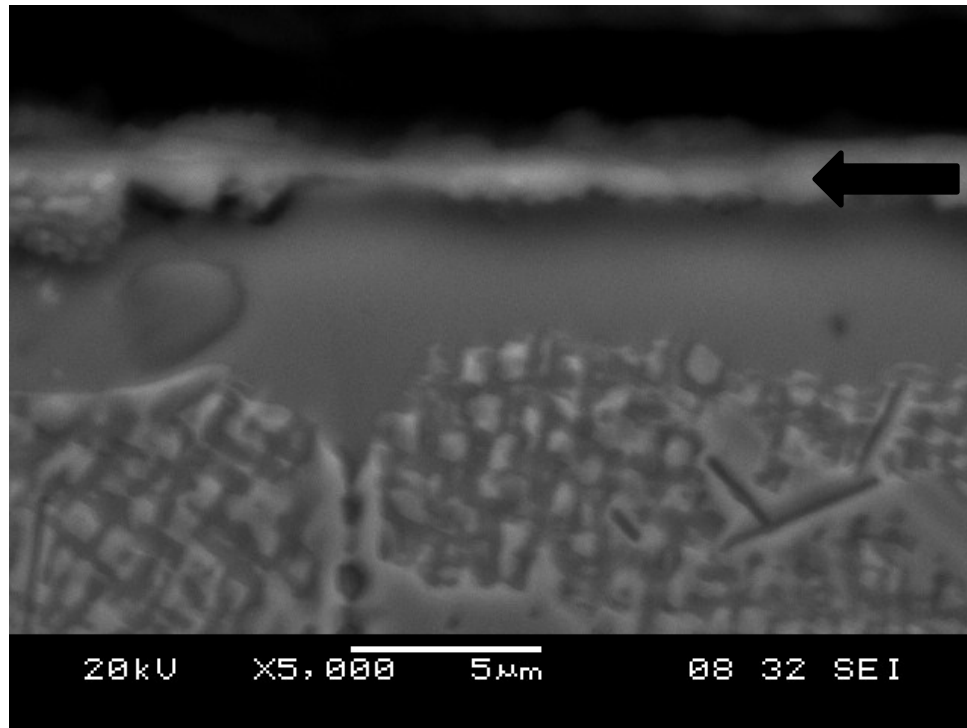


Figure 60 - Micrograph of TAS after 48h oxidation.

Figure 61 and Figure 62 show samples of TA and TAS respectively, now after 144h oxidation. The TA sample in Figure 61 has been heavily oxidized and shows various thicknesses in its oxide layer. The PFZ in this sample has increased and no longer appears to be of uniform in thickness (note the change in magnification from the previous Figures to afford a better resolution of the features of interest).

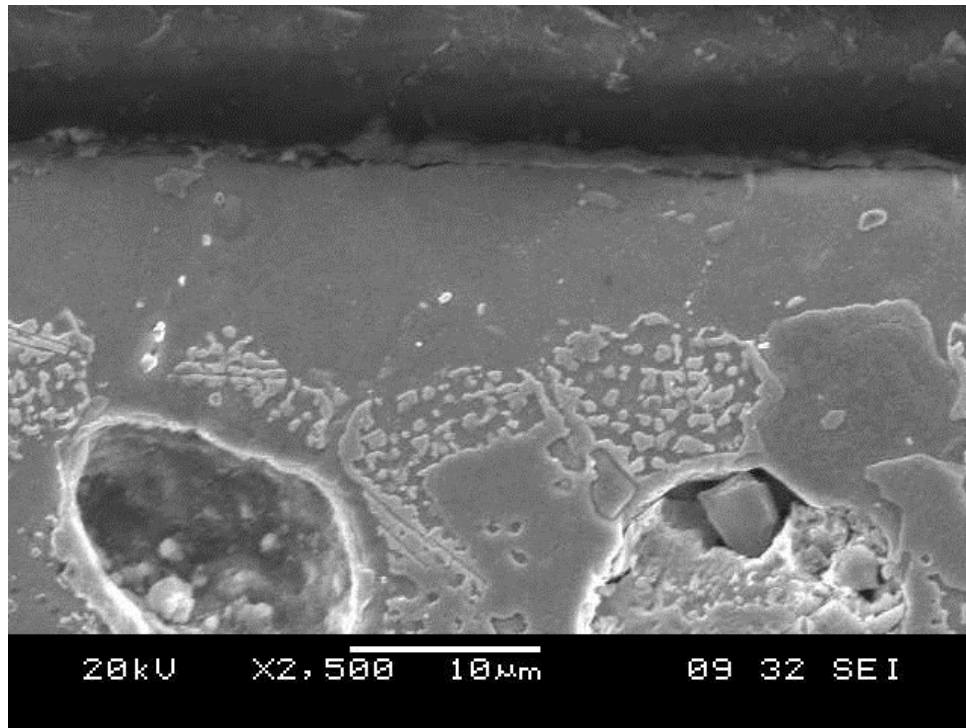


Figure 61 - Micrograph of TA after 144h oxidation.

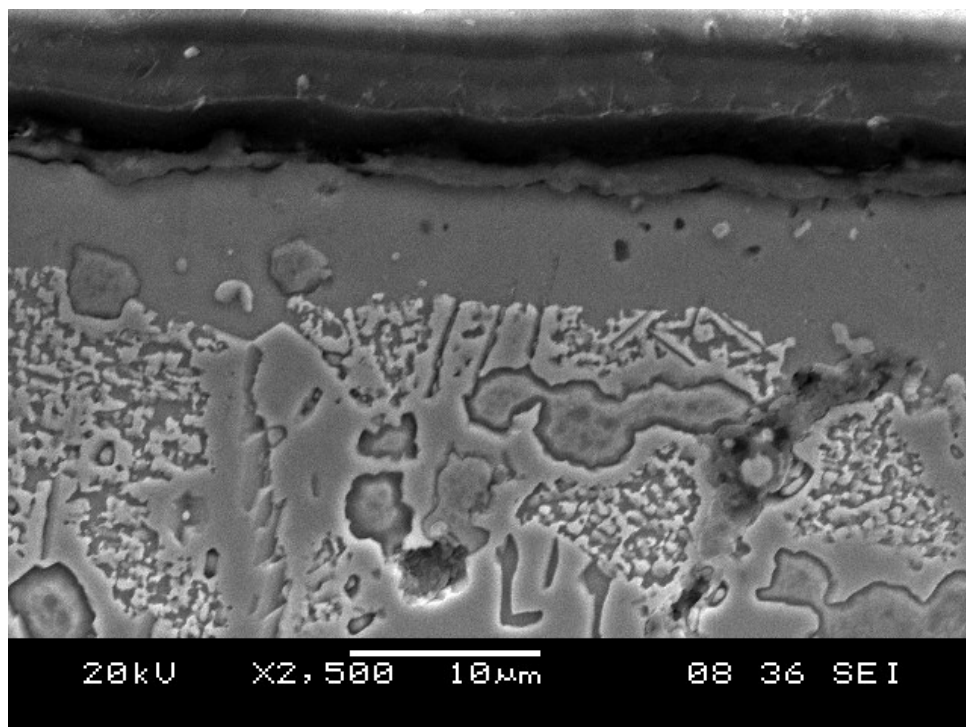


Figure 62 - Micrograph of TAS after 144h oxidation.

Figure 62 shows a much smaller and more uniform PFZ when compared with the TA sample oxidized for the same period of time. In this sample the oxide layer appears to have spalled or pulled away from the sample either during oxidation or possibly while setting in the epoxy cold mount medium. Visual observation after 144h oxidation did not indicate spalling. Therefore it has been assumed that the oxide pulled away from the sample while setting in the epoxy.

Figure 63 and Figure 64 show samples of TA and TAS respectively and both have been oxidized for 432 hours. Figure 63 reveals a massive depletion of the gamma prime precipitate for up to almost 40 $\mu$ m of the oxidized face. There is no adhered oxide on this sample that is visible at this magnification. Interestingly neither the weight gain nor oxide layer thickness for this TA sample for 432h changed significantly from the values for the sample oxidized for 144h as the sample was severely oxidized during this period (between 144h and 43h). Again, representative values for thickness of oxide layer as a function of oxidation time are given later in Tables 6, 7, 8 and 9.

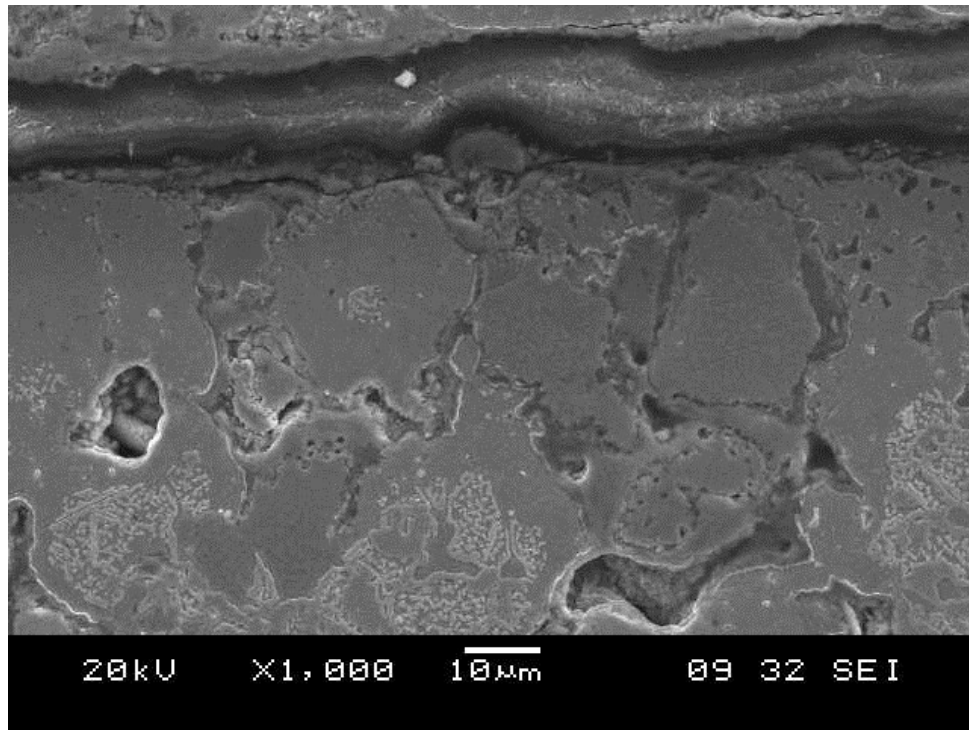


Figure 63 - Micrograph of TA after 432h oxidation.

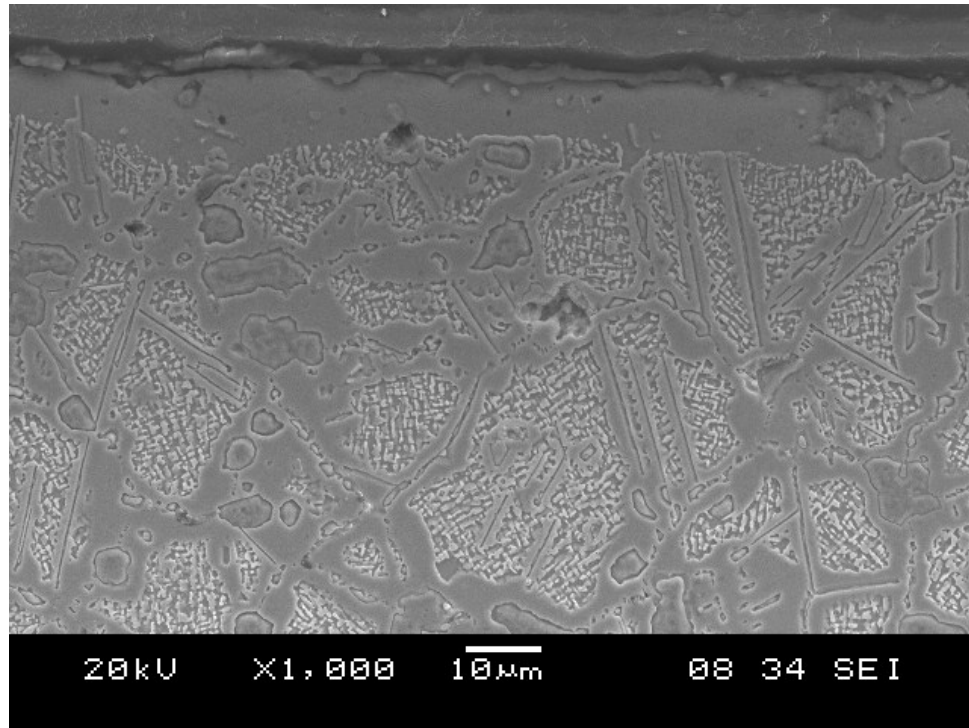


Figure 64 - Micrograph of TAS after 432h oxidation.

Figure 64 shows similar results to Figure 62 where the PFZ did not increase in width, if at all and at this magnification no distinguishable oxide layer is observed. The precipitates in certain areas of the microstructure appear to have grown which would be logical since aging at a temperature of 950°C for 4 hours grew precipitates to 0.3 µm that were unobservable at 10,000x magnification prior to ageing.

The depth of oxide layer and precipitate free zones are shown in Tables 6, 7, 8 and 9. There are several PFZ and oxide depths that were not measureable due to oxide loss during mounting or there was too large a deviation in the PFZ or oxide depth to be useful as data. These are noted as not measureable (NM) in the Tables.



Table 6 - Depth of oxide and PFZ for TA.

Oxidation time (h)	PFZ Thickness ( $\mu\text{m}$ )	PFZ $\pm$ ( $\mu\text{m}$ )	Oxide Thickness ( $\mu\text{m}$ )	Oxide $\pm$ ( $\mu\text{m}$ )
0	0.0	0.0	0.0	0.00
1	NM	NM	NM	NM
4	1.7	0.1	NM	NM
12	2.9	0.5	NM	NM
24	3.7	0.7	0.9	0.14
48	5.2	0.5	1.3	0.23
144	9.2	2.1	1.6	0.21
210	37.3	4.4	NM	NM
432	49.1	13.3	NM	NM
600	30.8	9.7	NM	NM
888	39.7	5.4	NM	NM

Table 7 – Depth of oxide and PFZ for TAY

Oxidation time (h)	PFZ Thickness ( $\mu\text{m}$ )	PFZ $\pm$ ( $\mu\text{m}$ )	Oxide Thickness ( $\mu\text{m}$ )	Oxide $\pm$ ( $\mu\text{m}$ )
0	0.0	0.0	0.0	
1	NM	NM	NM	NM
4	1.5	0.2	NM	NM
12	3.4	0.7	NM	NM
24	3.8	0.4	1.0	0.32
48	6.6	1.8	2.2	1.08
144	NM	NM	NM	NM
210	NM	NM	NM	NM
432	NM	NM	NM	NM
600	NM	NM	NM	NM
888	NM	NM	NM	NM

Table 8 – Depth of oxide and PFZ for TAS

Oxidation time (h)	PFZ Thickness ( $\mu\text{m}$ )	PFZ $\pm$ ( $\mu\text{m}$ )	Oxide Thickness ( $\mu\text{m}$ )	Oxide $\pm$ ( $\mu\text{m}$ )
0	0.0	0.0	0.0	0.00
1	NM	NM	NM	NM
4	1.5	0.3	NM	NM
12	1.6	0.2	1.3	0.35
24	2.8	0.3	1.5	0.60
48	4.1	0.8	1.5	0.26
144	8.5	1.6	1.2	0.18
210	9.6	0.7	1.8	0.05
432	9.3	0.4	1.8	0.80
600	10.0	1.3	1.3	0.57
888	8.9	1.4	2.4	0.29

Table 9 – Depth of oxide and PFZ for TAYS

Oxidation time (h)	PFZ Thickness ( $\mu\text{m}$ )	PFZ $\pm$ ( $\mu\text{m}$ )	Oxide Thickness ( $\mu\text{m}$ )	Oxide $\pm$ ( $\mu\text{m}$ )
0	0.0	0.0	0.0	0.00
1	NM	NM	NM	NM
4	1.8	0.0	NM	NM
12	1.7	0.0	0.9	0.05
24	3.1	0.3	0.9	0.45
48	3.4	0.4	2.0	0.12
144	7.5	0.3	NM	NM
210	6.1	1.0	NM	NM
432	9.8	0.6	NM	NM
600	11.7	1.1	NM	NM
888	14.1	2.0	16.6	0.36

As would be expected, the values are representative of the weight gain observed earlier whereby samples containing silicon were superior to those without Si, and the presence of yttrium alone and with silicon was either detrimental (the former, TAY) or had no measureable effect (the latter, TAYS).

The relationship between the extent of PFZ and oxide thickness is interesting. The PFZ continued to grow in the TAYS and TAS samples even after the oxide thickness had essentially stabilized. It is unlikely that the precipitates were going into solution as this was not predicted through DSC experiments to happen until around 1050°C for most compositions. Since the oxide layer had stabilized in thickness it appears the substrate was undergoing a heat treatment of sorts. It is possible that the dissolution of the  $\gamma'$  below the oxide layer was due to a kinetic event that was not measured while undergoing DSC testing of JMatPro modeling, the later being due to the fact that JMatPro models by assuming thermodynamic equilibrium. This would also help explain what appears to be a Widmanstatten pattern in some of the oxidized samples. This however was not investigated further as it was not the concentration of this research.

### **4.10.3 X Ray Diffraction of Oxidized Samples**

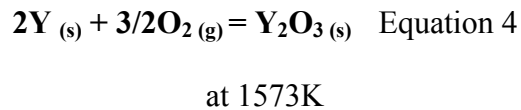
Following the oxidation tests all samples were also subjected to XRD, primarily to determine presence/absence of mineralogical occurrences in the oxide layer such as spinels. Representative spectra are given in Appendix A for TAYS after being oxidized at 900<sup>0</sup>C for various times. Interestingly, although qualitative EDS analyses showed the presence of Cr, no chromia or spinel species were found in the XRD spectra.

## CHAPTER 5 Assessment of findings

One of the more interesting aspects of these results is the apparent lack of improvement in oxidation resistance from the yttrium additions. This finding is contrary to evidence reported in the literature [24] [25] [34] [35] that suggest that yttrium additions on the order of 0.1 w/o should improve the oxidation resistance in a nickel-based Superalloy.

As an explanation for the findings in the present work it should be noted that these reports were for wrought or ingot produced products rather than materials produced via powder metallurgy. It is well known that one drawback of P/M processing is the large surface area present on each particle and the associated thermodynamic drive toward surface oxidation.

In an attempt to determine if the elemental yttrium would oxidize during sintering or hot deformation (prior to the oxidation tests), thermo-chemical data were sought for the reaction:



This would ordinarily be calculated through the equation:

$$\Delta G^0_{1573} = \Delta H^0_{298} + \int_{298}^{1573} \Delta C_p dT - T \Delta S^0_{298} - T \int_{298}^{1573} \frac{\Delta C_p}{T} dT \quad \text{Equation 5- [43]}$$

In this case however, no data were attainable for the  $\Delta C_p$ . It is stated by Kubaschewski that the heat capacity terms may be neglected as an initial approximation, especially if the substance does not go through a phase change [43]. This therefore simplifies the equation to:

$$\Delta G^0_{1573} = \Delta G^0_{298} = \Delta H^0_{298} - T\Delta S^0_{298} \quad \text{Equation 6 - [43].}$$

Knowing that:

$$\Delta H^0_{298} = -\frac{455.4 \text{ kcal}}{\text{mol}} \quad \text{and} \quad \Delta S^0_{298} = \frac{23.7 \text{ cal}}{\text{K} * \text{mol}}$$

$$\therefore \Delta G^0_{1573} = -\frac{488 \text{ kcal}}{\text{mol}}$$

If using a conversion of 4.184 joules = 1 cal;  $\Delta G^0_{1573}$  for  $Y_2O_3 = -\frac{1875 \text{ joule}}{\text{mol}}$

Next knowing that at equilibrium the Gibb's free energy equation reduces to:

$$\Delta G = \Delta G^\circ + RT \ln K_a = 0 \quad \text{Equation 7 - [43]}$$

If  $K_a$  is known as the equilibrium constant for the reaction then:

$$\Delta G^\circ = -RT \ln \frac{a_{Y_2O_3}^{\frac{3}{2}}}{a_{Y^2} * P_{O_2}^{\frac{3}{2}}} \quad \text{Equation 8}$$

Making the standard assumption that the substances are pure and in their standard state the equation can further be reduced to:

$$\Delta G^\circ = -RT \ln \frac{1}{1 * P_{O_2}^{\frac{3}{2}}} \quad \text{Equation 9}$$

Having previously determined the Gibb's standard free energy of formation and using the value of  $R = 8.314 \times 10^{-3} \text{ kJ/mol} \cdot \text{K}$ , the partial pressure of oxygen needed to oxidize the Y in this system was determined to be  $3.09 \text{ E}^{-42}$  atmospheres. This would signify that at equilibrium, all of the yttrium in this system would be oxidized at the sintering temperature of 1573K.

There are, however, several flaws in this calculation. For example, the  $C_p$  value was neglected, the system is assumed to be at equilibrium and this does not determine how deeply the actual yttrium particles would have oxidized. It is highly possible that they form a small oxide shell around each particle which is only a few nano-meters thick, which is similar to what is found for powders used in aluminum powder metallurgy. This shell could potentially be fractured during pressing, exposing a fresh, un-oxidized surface that is then directly touching an un-oxidized particle. This would be expected to sinter properly (i.e. not simply oxidize under high vacuum). Also nothing is addressed about the competing elements within this powder metallurgy system. Another element may prove an even more aggressive "getter" for oxygen under these sintering conditions and this could be proven through scanning ion mass spectroscopy, or transmission electron microscopy. Nonetheless, there is still the strong possibility that under the P/M processing conditions used the Y had oxidised prior to oxidation testing. Unfortunately, due both to the small size and small amounts of Y used, no Y was detected in any of the SEM-EDS investigations.

Another interesting observation from this work is the apparent lack of solutionizing behaviour of the gamma prime during the hot forging/Gleeble testing. These tests were done at  $1200^{\circ}\text{C}$ , well above the  $1050^{\circ}\text{C}$  predicted by JMatPro, the  $1045\text{-}1064^{\circ}\text{C}$  indicated by the DSC study or various values found in the literature (e.g.  $1175^{\circ}\text{C}$ , [20] [25]). Bearing in mind that the JMatPro value assumed equilibrium thermodynamic behaviour and that the literature values were for wrought rather than P/M material it is possible that the temperature chosen was not high enough to enable a reasonable rate of reaction for a P/M material. The compacts in the present work all contained about 10v/o porosity as well as prior particle boundaries, both of which could alter the solutionizing behaviour.

The fact that a water quenched Gleeble sample showed the same behaviour suggests that cooling rate was not a factor in determining the microstructure and that perhaps primary  $\gamma'$  had solutionized, but smaller secondary  $\gamma'$  formed on cooling.

Irrespective of these issues, samples for the four compositions exposed to the oxidation tests all had similar microstructures regarding v/o gamma prime and porosity leaving compositional differences as the major contributor to the differences found in oxidation behaviour.

## CHAPTER 6 Summary and Conclusions

The following conclusions may be drawn from this work.

1. Whereas the modeling tool JMatPro predicted onset of melting and solutionizing temperature of the compositions studied, the w/o  $\gamma'$  predicted was lower than that measured. This may be due to the P/M press and sinter process or the use of a thermodynamic based software to model a kinetic event. Nonetheless, the software provided a reasonable guide in determining both sintering temperature and post-Gleeble heat treatment temperature.
2. The addition of 0.5w/o Si to the quaternary Ni-Cr-Fe-Al P/M system provided a measureable improvement in the oxidation resistance both in terms of thickness of oxide layer and in overall weight gain.
3. The addition of 0.1w/o Y alone to the quaternary system, was found to be detrimental to overall oxidation resistance in the absence of Si, and to have little influence in the presence of Si
4. The  $P_{O_2}$  for the reaction  $2Y + 3/2O_2 = Y_2O_3$  at 1573K was determined to be approximately  $3.09 \times 10^{-42}$  atmospheres. Therefore a thin oxide shell would be expected to form on these particles during sintering thereby reducing the ability of the Y to improve oxidation resistance. If a very thin (nano-meter thick) oxide shell was formed on these particles it may not actually oxidize to any significant depth. However this does not take into account the “gettering” or any potential synergistic effects of the other elements in this powder metallurgy system.
5. The combination of small Al (7.2 $\mu$ m) and small Si (3.9 $\mu$ m) produced much better sintering results when compared with 15.6 $\mu$ m Al and the same Si in the same compositions and resulted in an improvement in sintered density of the Al and Si containing alloys by almost 10%.
6. All the alloys in this study can be successfully Gleeble hot forged by 30% of their original width without cracking. Therefore, this process may well lend itself to additional porosity reduction if parameters such as hold (solutionizing) time and cooling rate are further examined.



## References

- [1] M. J. Donachie and S. J. Donachie, *Superalloys A Technical Guide*, 2nd ed.: ASM international, 2002.
- [2] W. F. Smith, *Structure and Properties of Engineering Alloys*.: McGraw-Hill Inc., 1993, pp. 480-513.
- [3] C. Sims and W. C. Hagel, *The Superalloys*.: Wiley - Interscience Publication. 1972, pp. 281-314.
- [4] Z. W. Huang, Z.G. Wang, S.J. Zhu, F.H. Yuan and F.G. Wang, "Thermomechanical behaviour and life prediction of a cast nickel-based superalloy," *Materials Science and Engineering*, vol. A , no. 432, pp. 308-316, 2006.
- [5] S. S. Manson and G. R. Halford, *Fatigue and Durability of Metals at High Temperatures*.: ASM International, 2006.
- [6] ASM, "ASM Metals Handbook," in *Fatigue and Fracture*.: ASM International, 1996, vol. 19, pp. 1313-1402.
- [7] Y. Kadioglu and H. Sehitoglu, "Thermomechanical and Isothermal Fatigue Behaviour of bare and coated Superalloys," *Journal of Materials and Technology*, vol. 118, no. 1, pp. 96-102, 1996.
- [8] C. Cai, P. Kiliaw, M. Ye and J. Yu, "Recent Developments in the Thermomechanical Fatigue Life Prediction of Superalloys," *Journal of Metallurgy*, vol. 51, no. 4, April 1999.
- [9] (2011, April) [Online]. <http://www.ocas.be/MC.MT.14>
- [10] G. H. Gessinger, *Powder Metallurgy of Superalloys*. London: Butterworth and Co., 1984.
- [11] R. M. German, *Powder Metallurgy Science*. New Jersey: Metal Powder Industries Federation, 2001.
- [12] S. B. Justus and J. J. Eckenrod, in *Sixth International Symposium on Environmental Degradation of Materials in Nuclear Power Systems-Water Reactors*, 1993.
- [13] G. E. Maurer and W. Castledine, *Superalloys*.: The Minerals, Metals and Materials Society, 1996.
- [14] R. G. Iacocca, *Met and Mater Trans. A*, vol. 27, no. A, pp. 145-153, 1996.
- [15] E. F. Bradley, *Superalloys: A Technical Guide*.: ASM international, 1998.
- [16] R. M. German, *Powder Metallurgy Science*.: Metal Powder Industries Federation, 1984.
- [17] D. Brown. (2001, June ) The A to Z of Materials. [Online]. <http://www.azom.com/Details.asp?ArticleID=527>
- [18] Thermal Analysis Newsletter, Norwalk, Connecticut, no. 9, Perkin-Elmer Corporation, 1970
- [19] R. M. German, *Sintering Theory and Practice*. New York, New York: John Wiley and Sons Inc., 1996.
- [20] M. J. Donachie, "Superalloys," in *Souce Book: A collection of outstanding articles from the technical literature*.: ASM International, 1984, pp. 98, 219, 272.

- [21] (2011, January) [Online]. <http://www.bleeble.com/3800.htm>
- [22] T. N. Rhys-Jones, "Protective oxide scales on Superalloys and coatings used in gas turbine blade and vane applications," *Materials Science and Technology*, vol. 4, pp. 421-429, May 1988.
- [23] J. A. Haynes, "Comparison of thermal expansion and oxidation behavior of various high-temperature coating materials and superalloys," *Materials at High Temperatures*, vol. 21, no. 2, pp. 87-94, 2004.
- [24] N. Birks, G. H. Meier and F.S Pettit, *Introduction to the High-Temperature Oxidation of Metals*, Cambridge University Press, 2009, pp. 101-149.
- [25] C. T. Sims, N. S. Stoloff and W. C. Hagel, "Superalloys II," in *High-temperature materials for aerospace and industrial power*. New York, New York: John Wiley and Sons, 1987, pp. 293-326.
- [26] C. Booth-Morrison, R. D. Noebe and D. N. Seidman, "Effects of Tantalum addition on the morphological and compositional evolution of a model Ni-Al-Cr Superalloy," *Superalloys*, pp. 73-79, 2008.
- [27] T. A. Ramanarayanan, R. Ayer, R. Petkovic-Luton and D. P. Leta, "The Influence of Yttrium on Oxide Scale Growth and Adherence," *Oxidation of Metals*, vol. 29, no. 5/6, pp. 445-452, 1988.
- [28] D. A. Akinlade, "Development, Processing and Fabrication of a Nickel Based Nickel-Chromium-Iron Alloy," University of Manitoba, PhD thesis April 2008.
- [29] D. C. Murray, D. A. Akinlade, W. F. Caley and N. L. Richards, "Microstructural and thermal processing effects on adding 3w/o Ti to a powder metallurgy processed Ni-Cr-Fe alloy", *Can. Met. Quart.*, vol. 50, no. 3, pp. 273-277, 2010.
- [30] B. Li, B. Gleeson, "Effects of Silicon on the Oxidation Behavior of Ni-Base Chromia-Forming Alloys," *Oxidation of Metals*, vol. 65, no. 1/2, pp. 101-121, February 2006.
- [31] M. J. Bennett, "The Role of Ion Implantation in High Temperature Oxidation Studies," in *High Temperature Corrosion*, March 2-6, 1981, pp. 145-154.
- [32] J. R. Nicholls, "Designing Oxidation-Resistant Coatings," *Journal of Materials*, pp. 28-35, January 2000.
- [33] C. S. Giggins, "Oxidation of Ni-Cr-Al Alloys Between 1000C and 1200C," *Journal for the Electrochemical Society*, vol. 118, no. 11, pp. 1782-1790, 1971.
- [34] A. C. Yeh, K. Kawagishi, H. Harada, T. Yokokawa, Y. Koizumi, T. Kobayashi, D. Ping, J. Fujioka and T. Suzuki, "Development of a Si-Bearing 4th Generation Ni-Base Single Crystal Superalloys," in *Superalloys 2008*, 2008, pp. 619-629.
- [35] K. N. Strafford, "High temperature corrosion of alloys containing rare earth or refractory elements: a review of current knowledge and possible future developments," *High Temperature Technology*, vol. 1, no. 6, pp. 307-318, November 1983.
- [36] G. C. Wood and F. H. Stott, "The Development and Growth of Protective  $\alpha - \text{Al}_2\text{O}_3$  Scales on Alloys, High Temperature Corrosion," in *High Temperature Corrosion*, March 2-6th, 1981, pp. 227-249.
- [37] (2011, May) Calphad. [Online]. <http://www.calphad.com/jmatpro.html>

- [38] N. Saunders, Phase Diagram Calculations for Ni-Based Superalloys. TMS, 1996, p. 101.
- [39] D. A. Akinlade, W. F. Caley, N. L. Richards, and M. C. Chaturvedi, "Development of a powder metallurgy (PM) nickel base Superalloy," *International Journal of Powder Metallurgy*, vol. 42, pp. 43-56, 2006.
- [40] MPIF, Method for Determination of Density of Compacted of Sintered Powder Metallurgy Products-Standard 42, 2002.
- [41] D. A. Akinlade, W. F. Caley, N. L. Richards, and M. C. Chaturvedi, "Thermodynamic Modelling of a 6w/o Al P/M Processed Ni Based Superalloy," in *WIT Transactions on Engineering Sciences*, Italy, 2007, pp. 85-94.
- [42] D. C. Murray, "Characterization of a P/M produced Nickel based Superalloy with minor reactive element additions," Materials Engineering, Dalhousie University, Halifax, Matl 4804 Report, 2009.
- [43] O. Kubaschewski and C. B. Alcock, *Metallurgical Thermo-Chemistry*, 5th ed., G. V. Raynor, Ed. New York, US: Pergamon Press, 1979, vol. 24.

## APPENDIX A

The following images are samples at various stages of oxidation.

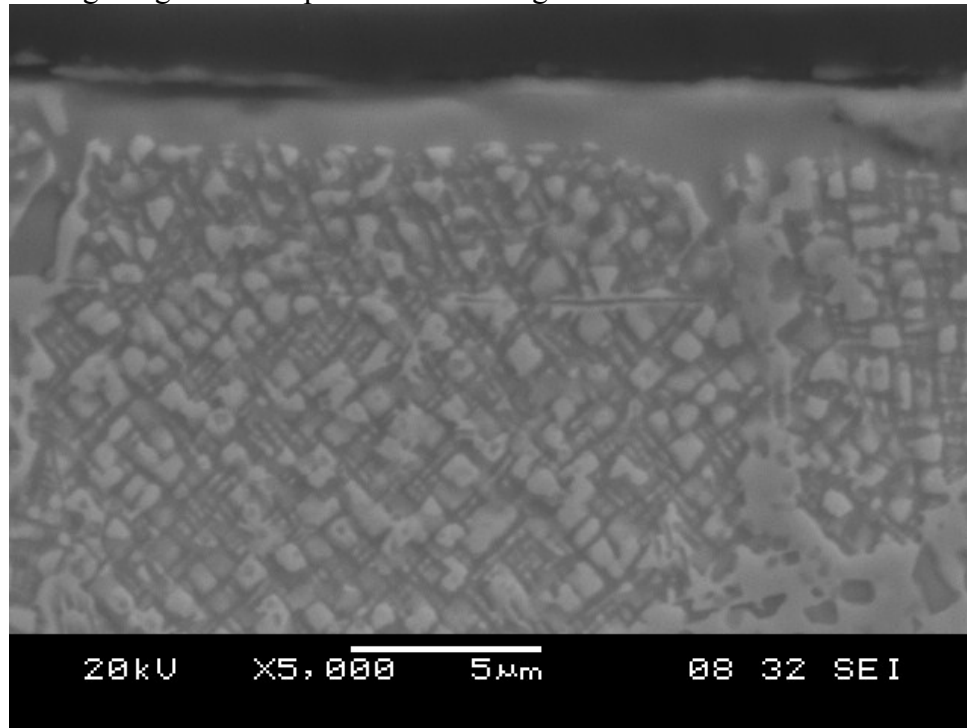


Figure A1- Micrograph of TA after 4h oxidation.

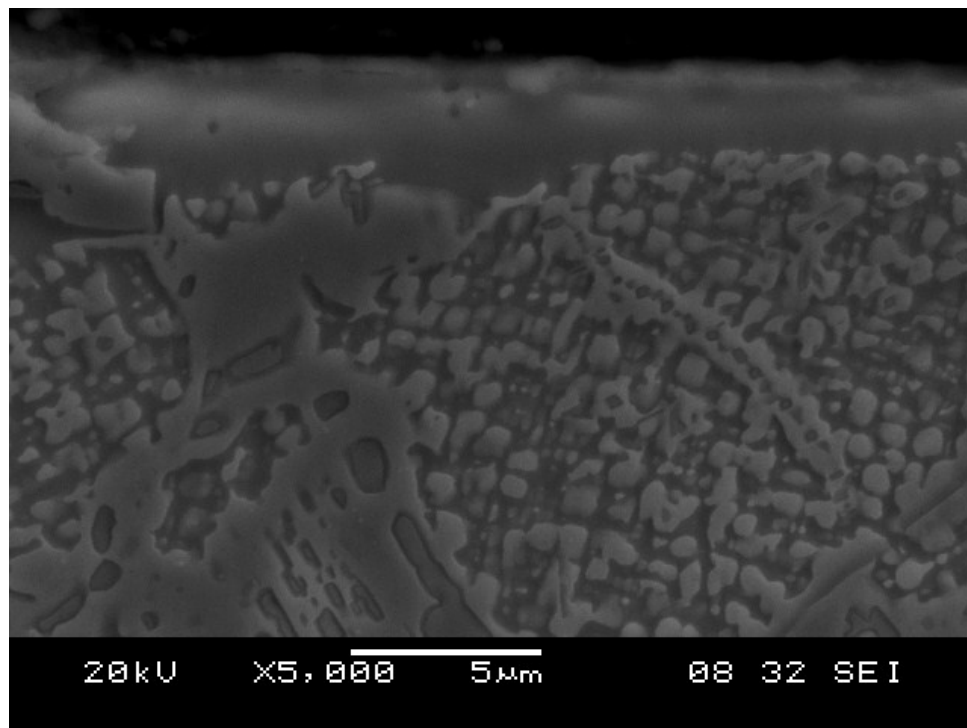


Figure A2 –Micrograph of TA 12h oxidation.

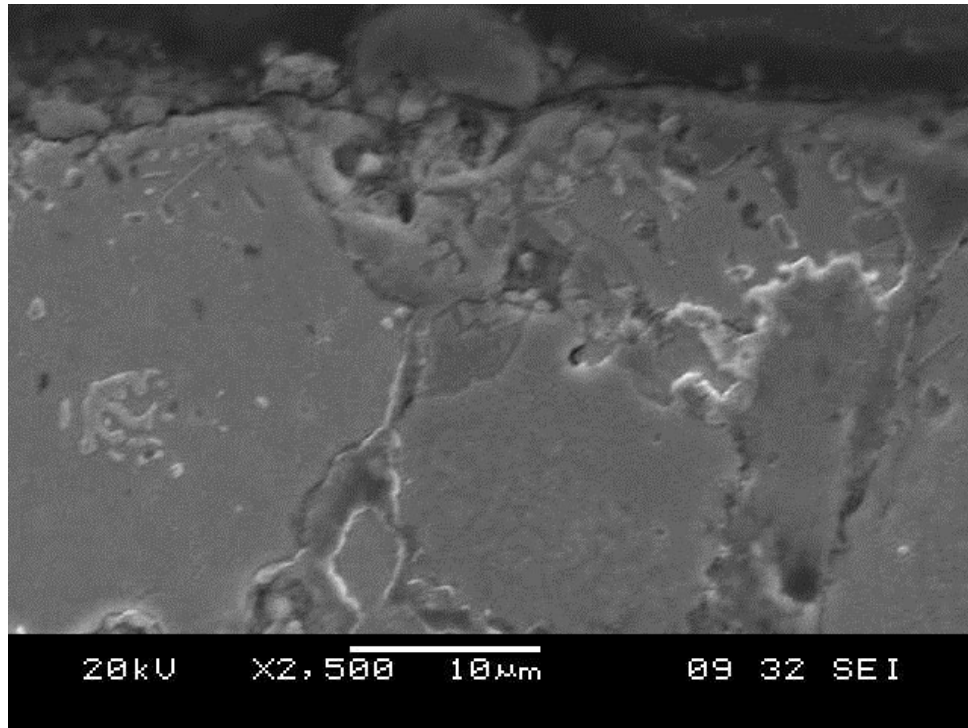


Figure A3 - Micrograph of TA after 210h oxidation.

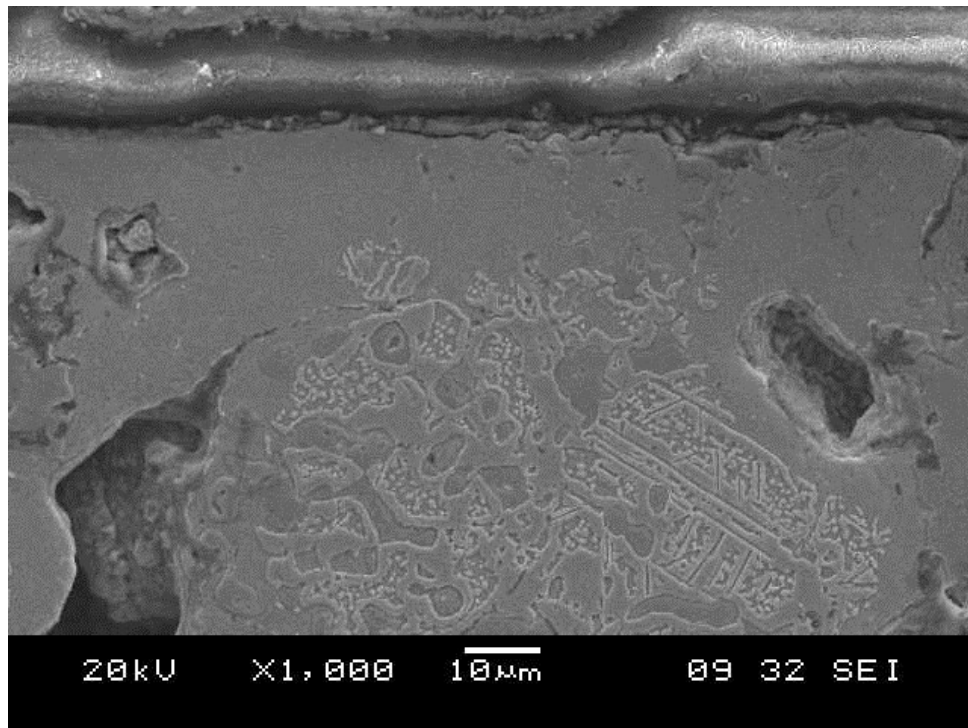


Figure A4 – Micrograph of TA after 600h oxidation.



Figure A5 - Micrograph of TA after 888h oxidation.

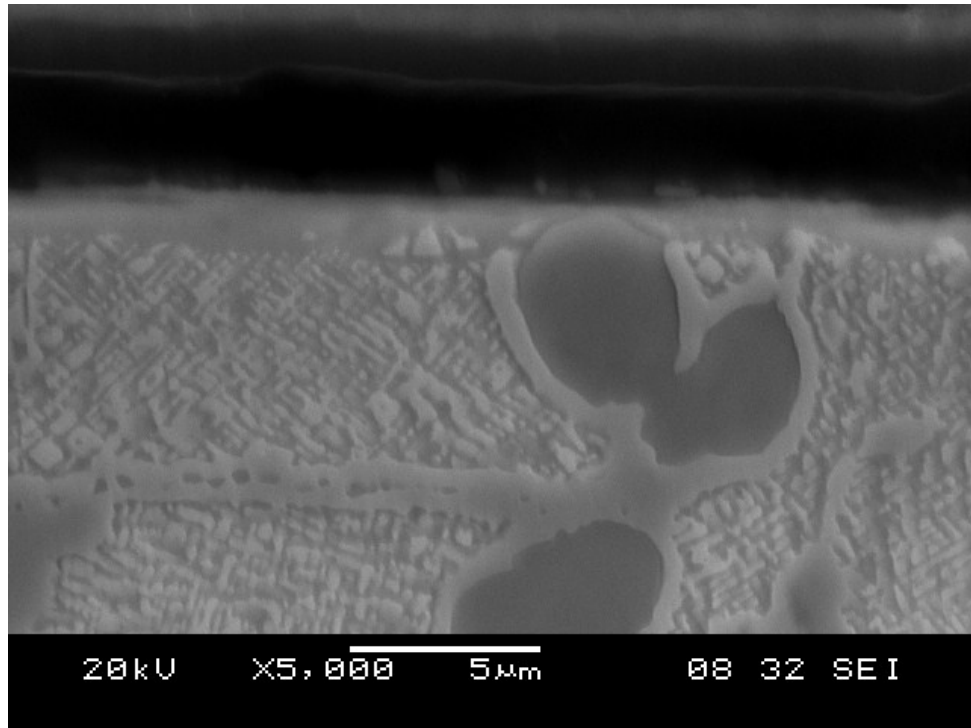


Figure A6 – Micrograph of TAS after 4h oxidation.

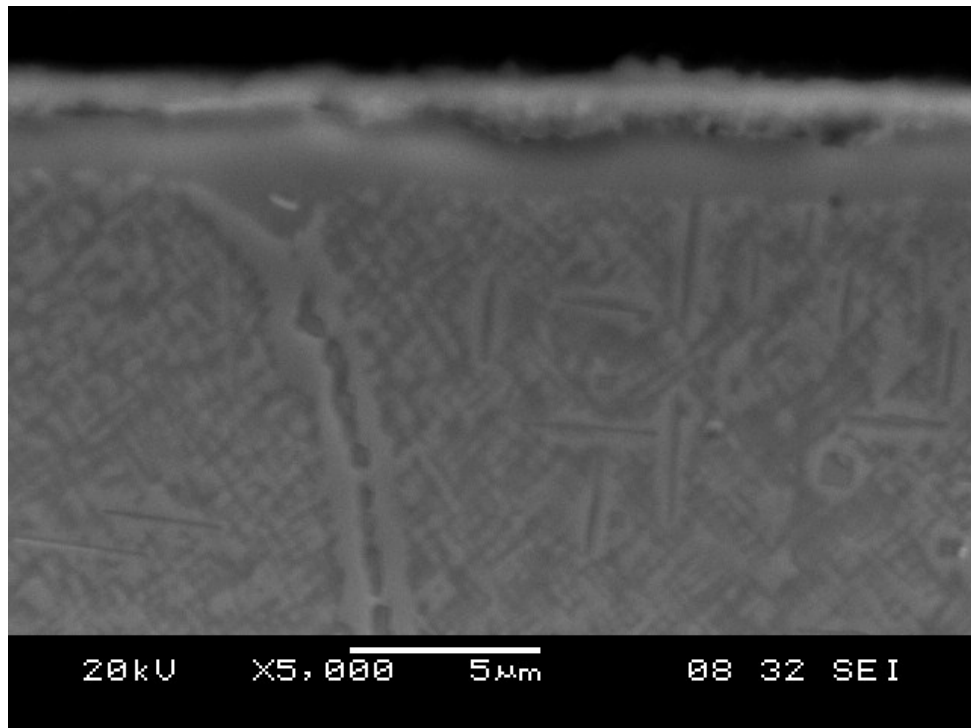


Figure A7 – Micrograph of TAS after 12h oxidation.

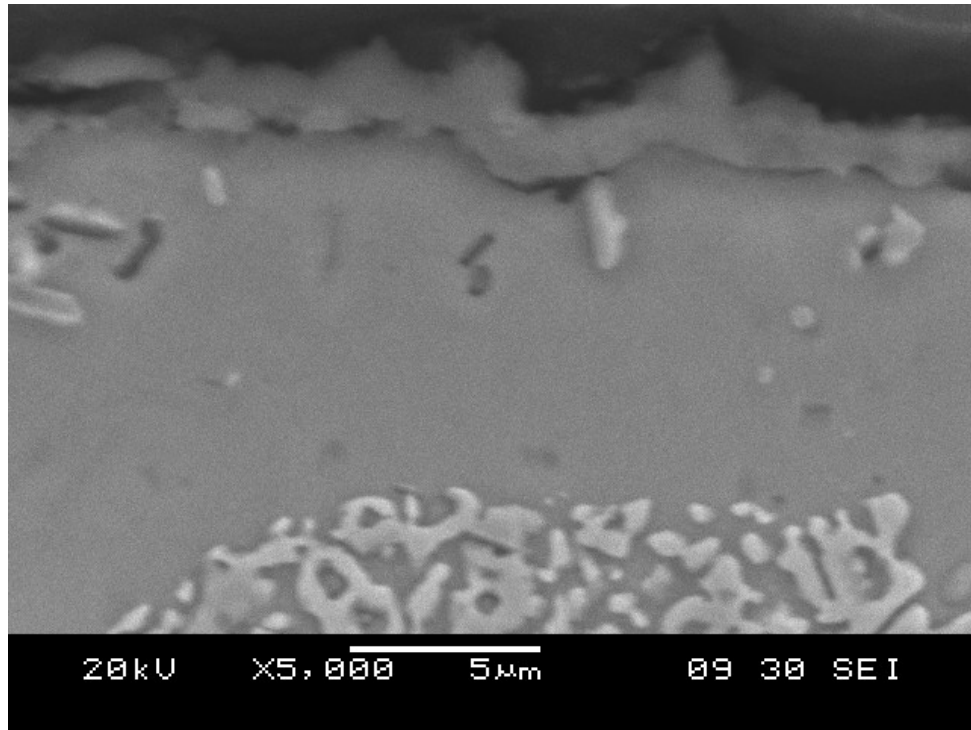


Figure A8 – Micrograph of TAS after 210 h oxidation.

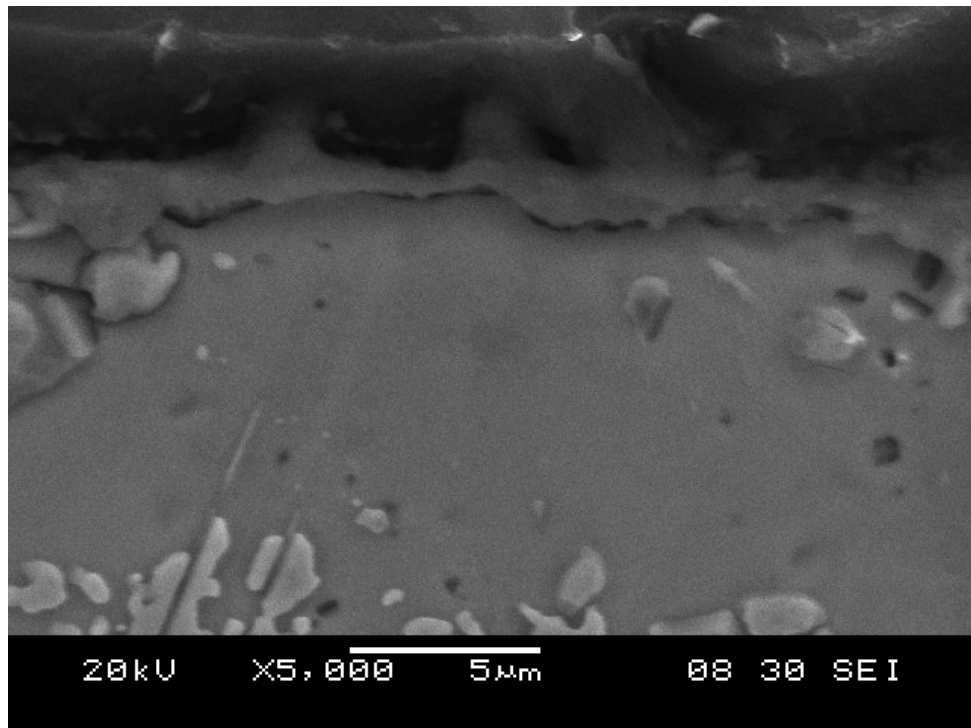


Figure A9- Micrograph of TAS after 600h oxidation.



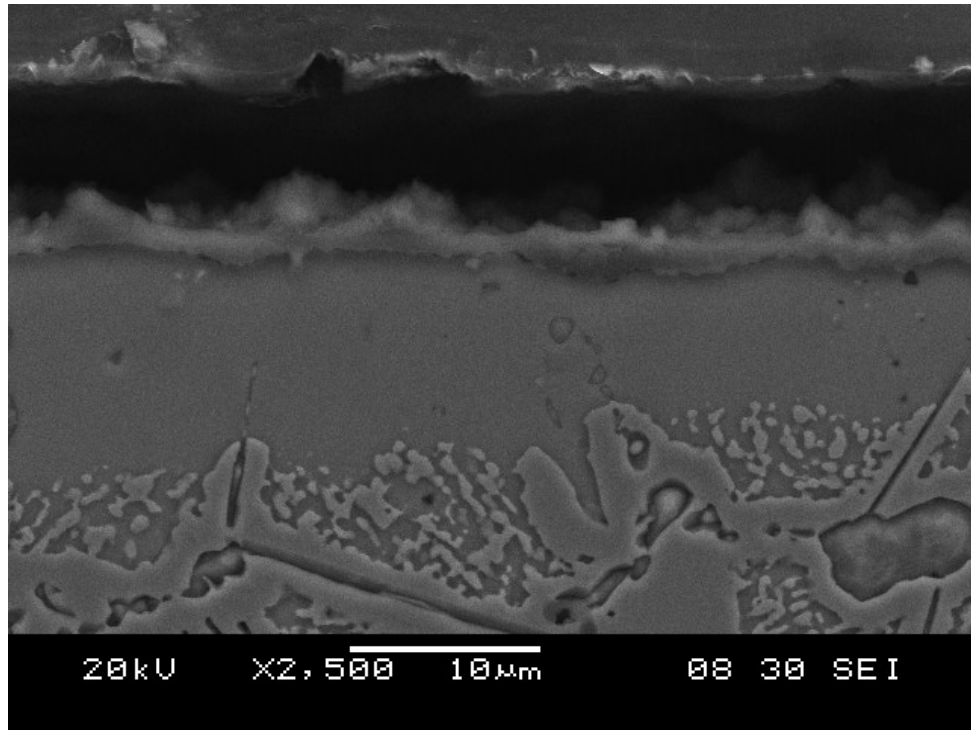


Figure A10 – Micrograph of TAS after 888h oxidation.

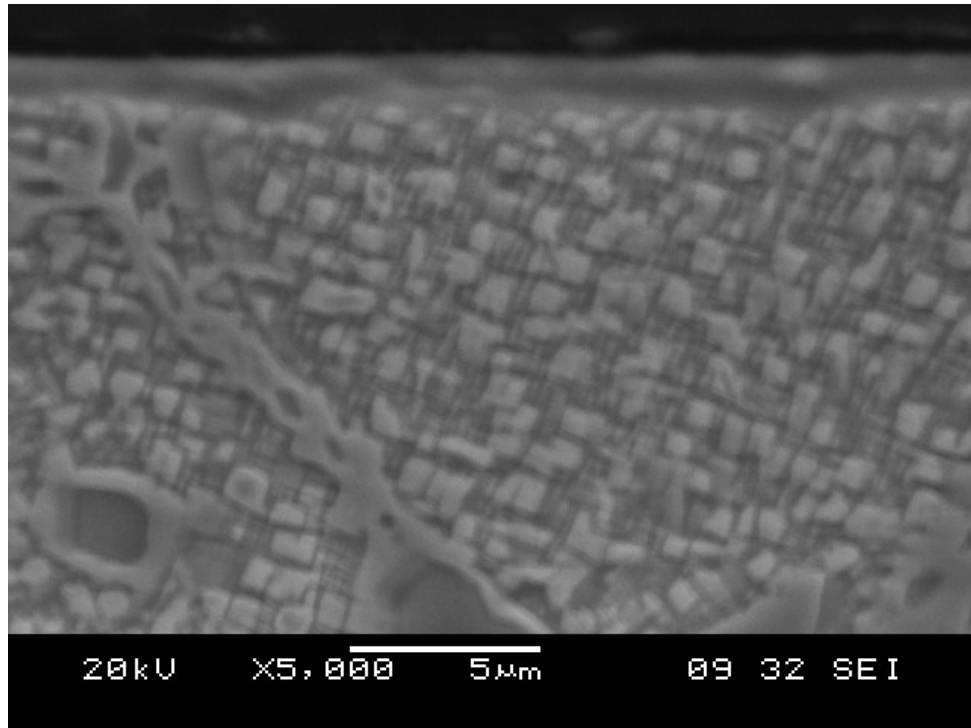


Figure A11 – Micrograph of TAY after 4h oxidation

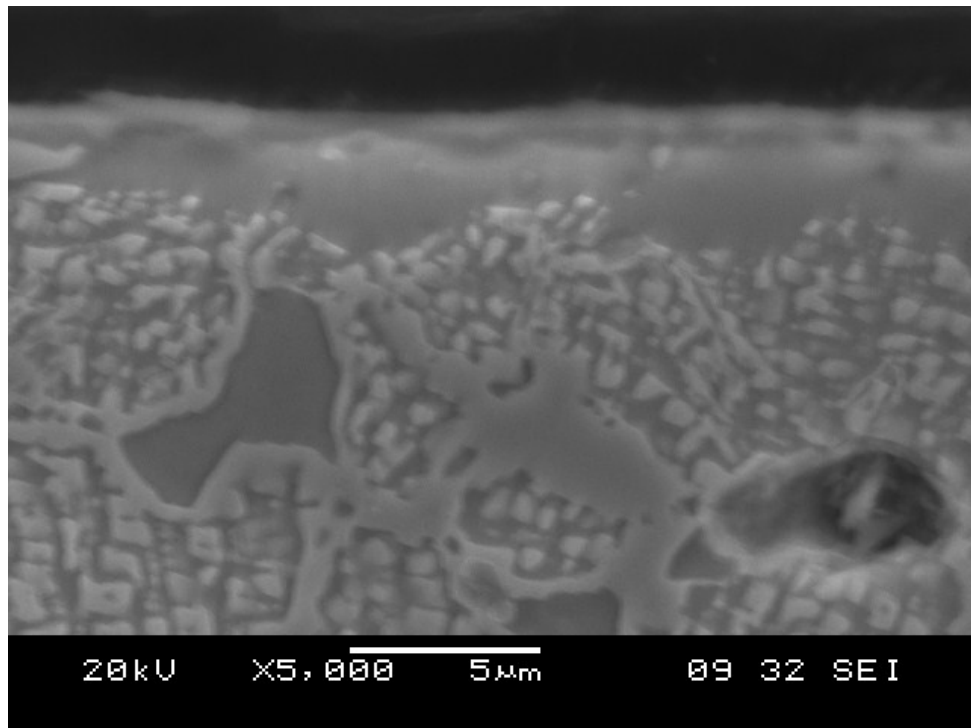


Figure A12- Micrograph of TAY after 12h oxidation

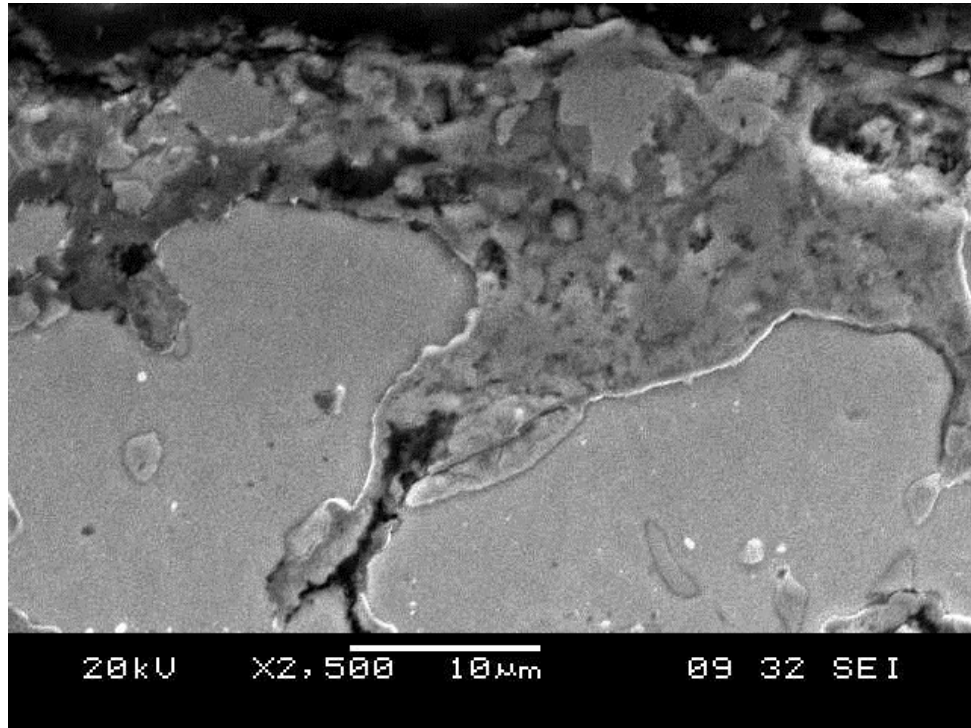


Figure A13 – Micrograph of TAY after 210h oxidation.

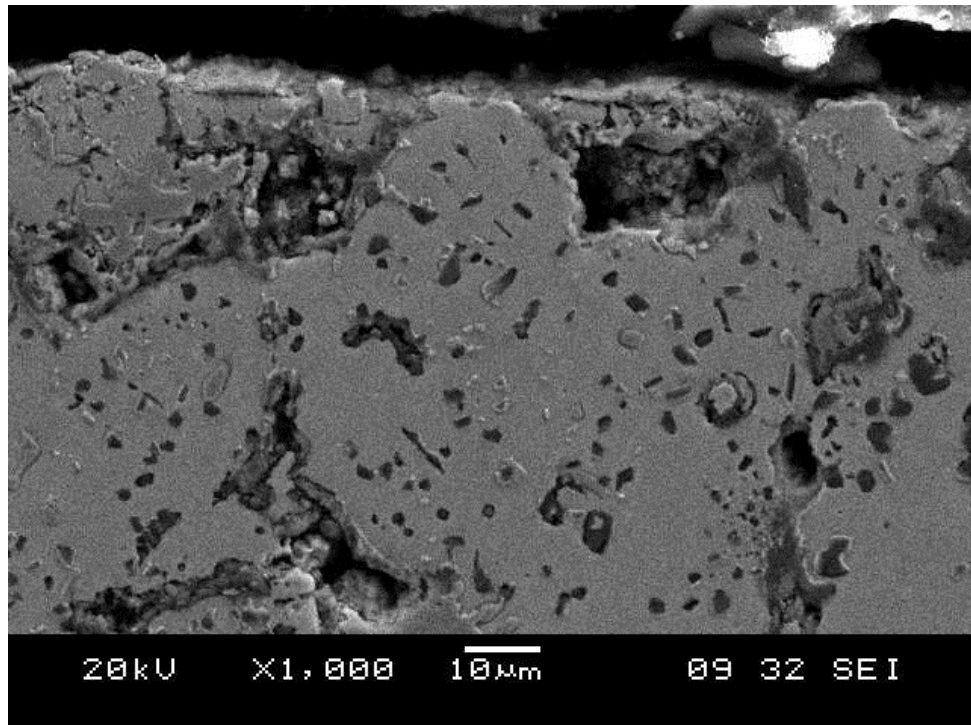


Figure A14 – Micrograph of TAY after 888h oxidation.

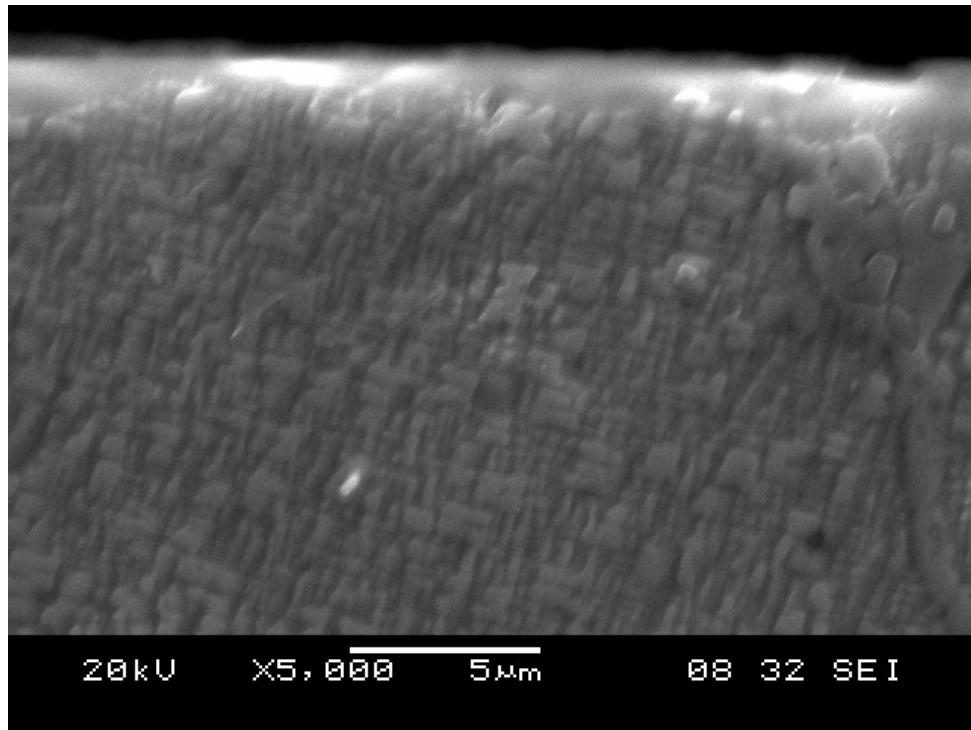


Figure A15 – Micrograph of TAYS after 4h oxidation

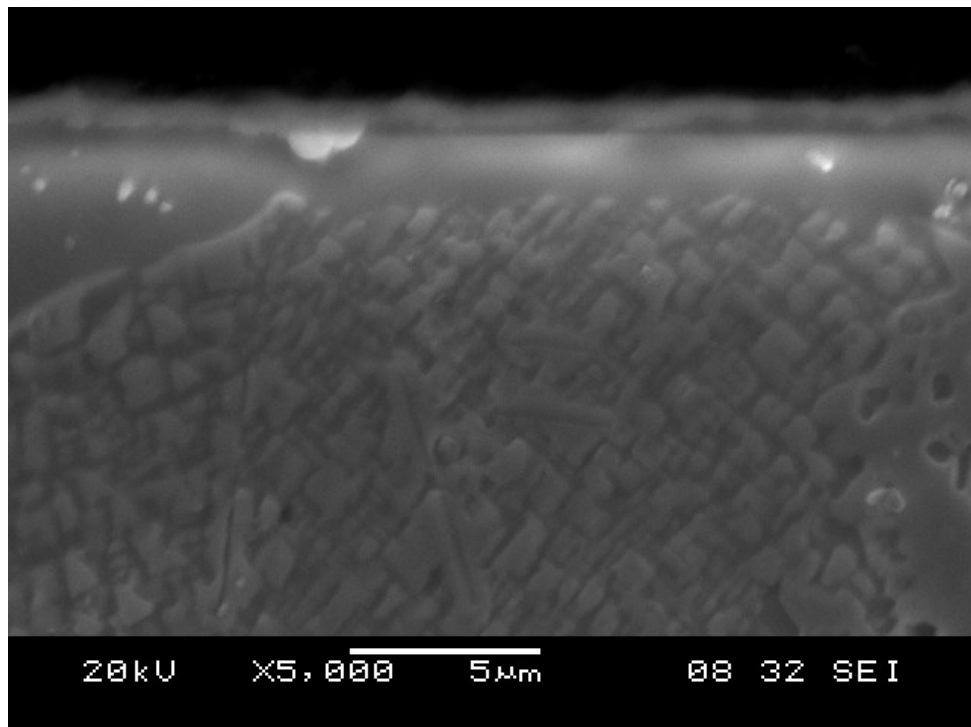


Figure A16 – Micrograph of TAYS after 12h oxidation.

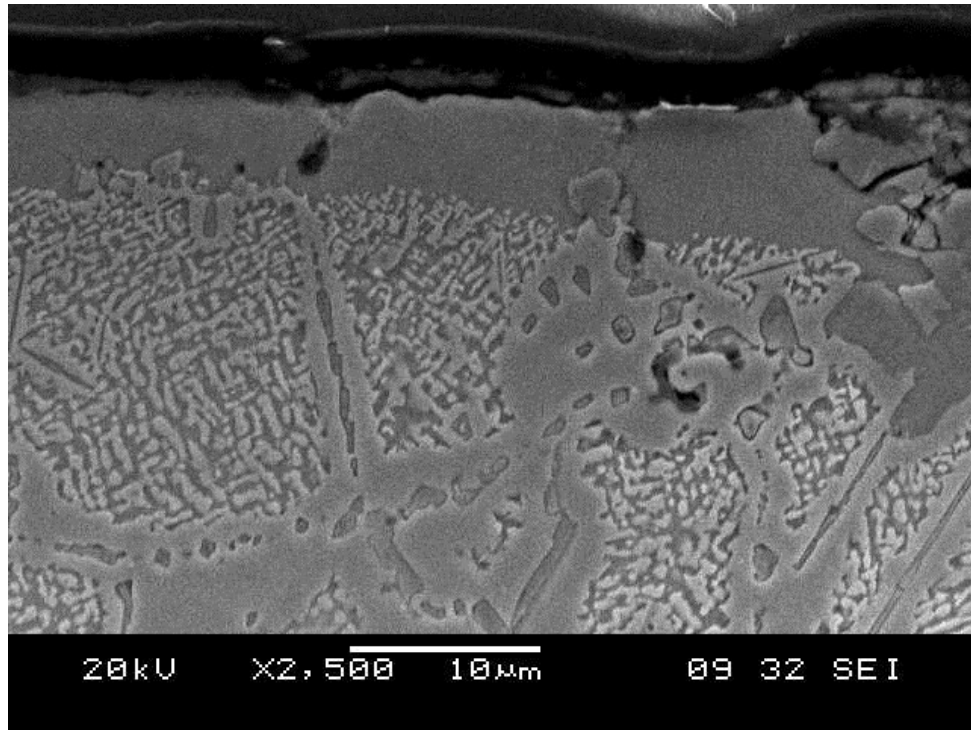


Figure A17 – Micrograph of TAYS after 210h oxidation.

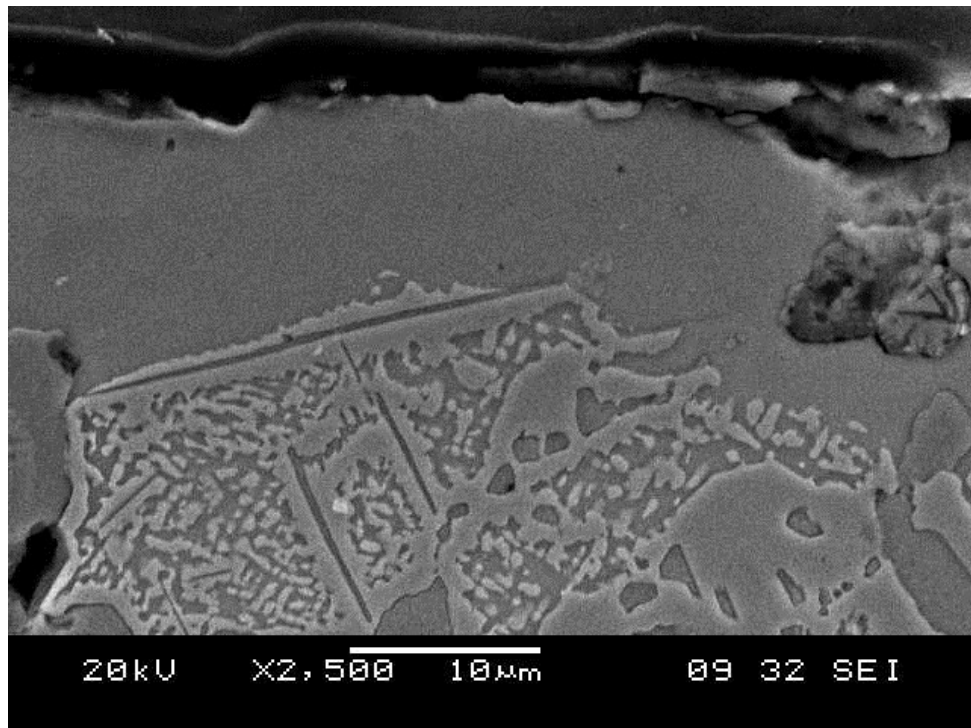
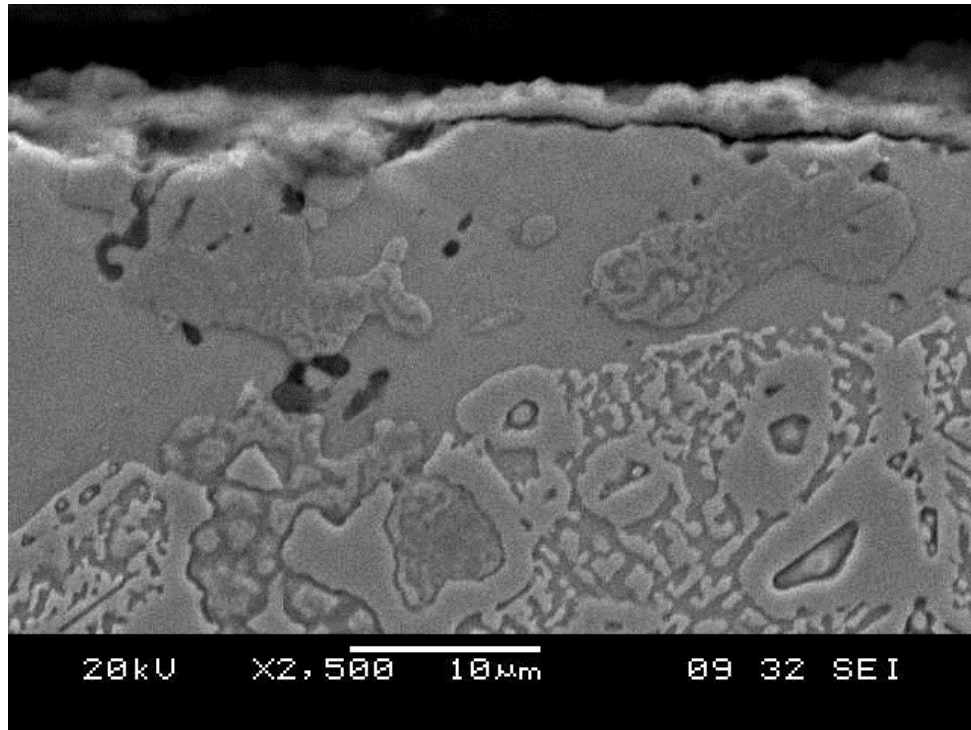


Figure A18 - Micrograph of TAYS after 600h oxidation.



Micrograph A19 – Micrograph of TAYS after 888h oxidation.

The following are XRD spectra taken of samples in the as sintered, Gleebled (pre-heat treated, and Gleebled (post-heat treated) conditions as well as an overlay of post 1h and 1000h oxidation for the TAYS alloy.

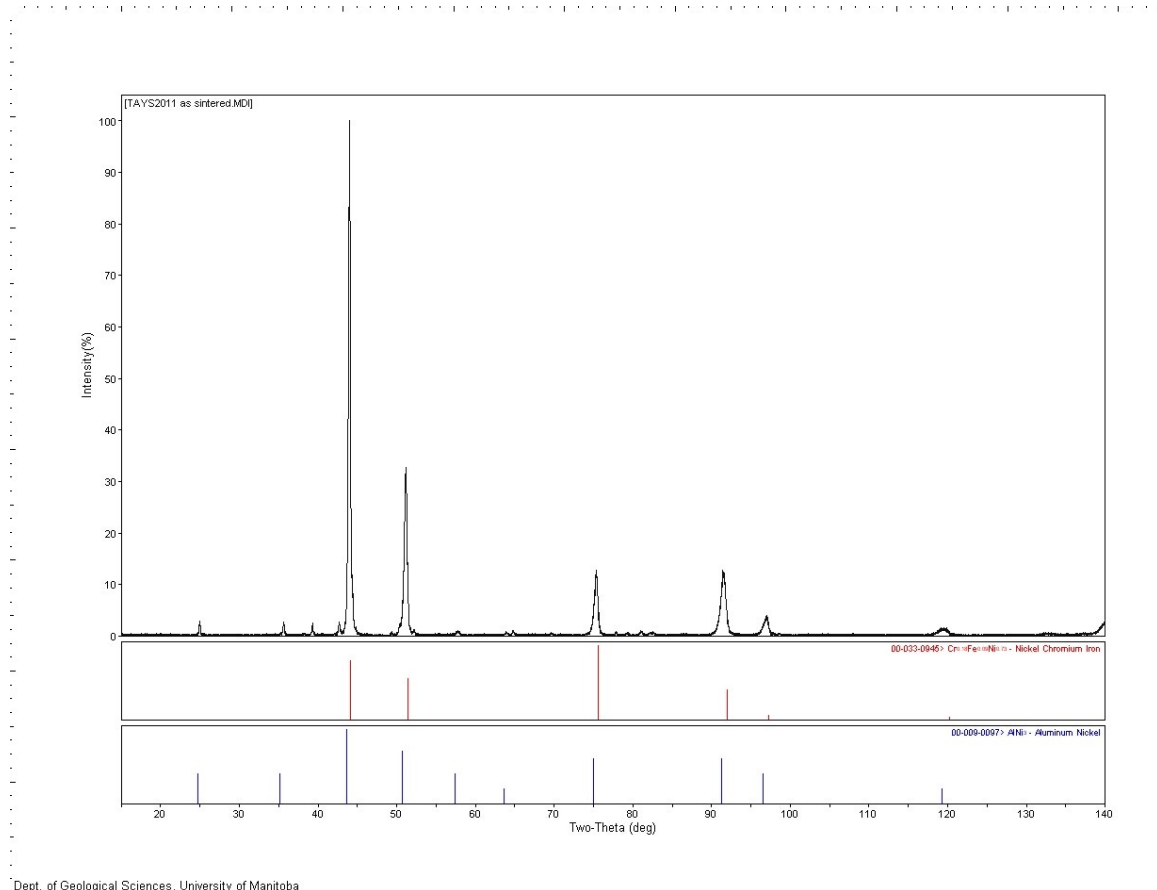


Figure A21 - XRD spectrum for TAYS in the as sintered condition

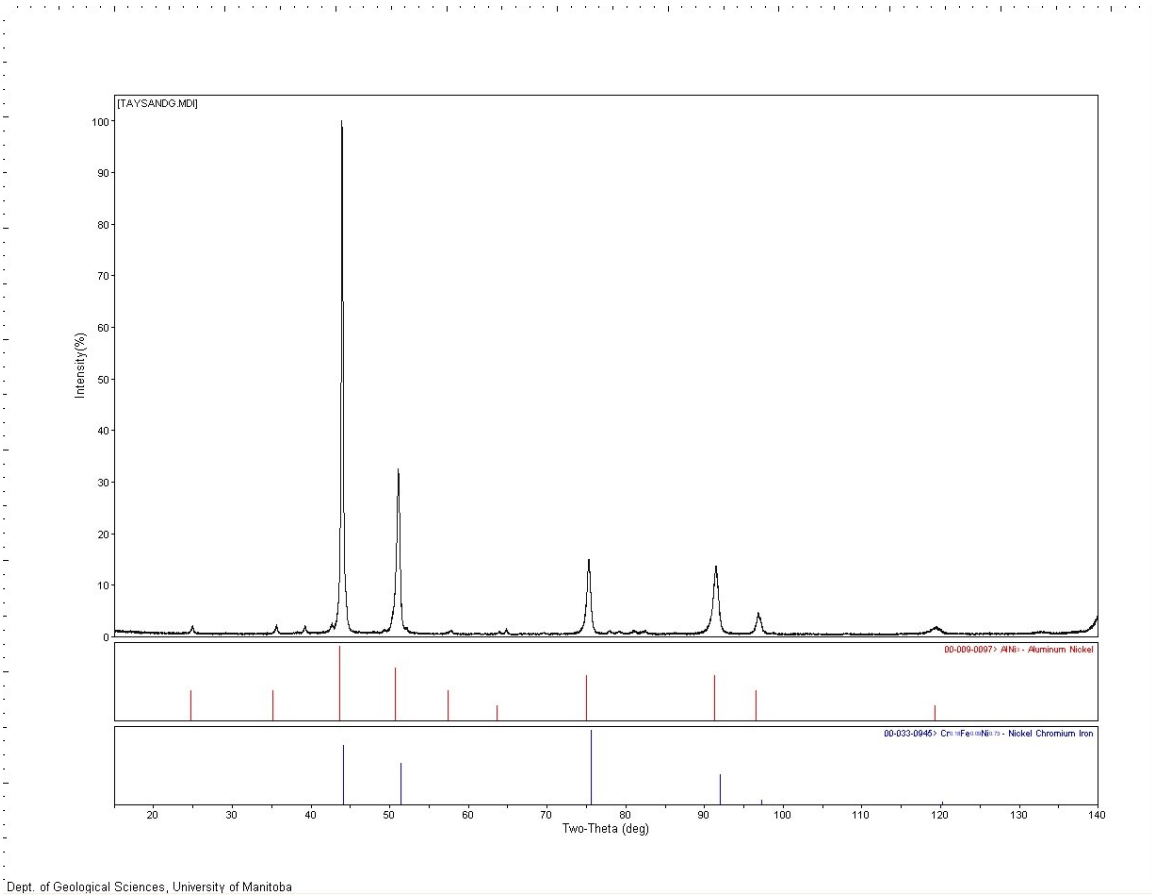


Figure A22- XRD spectrum for TAYS in the Gleeble, pre-heat treated condition.



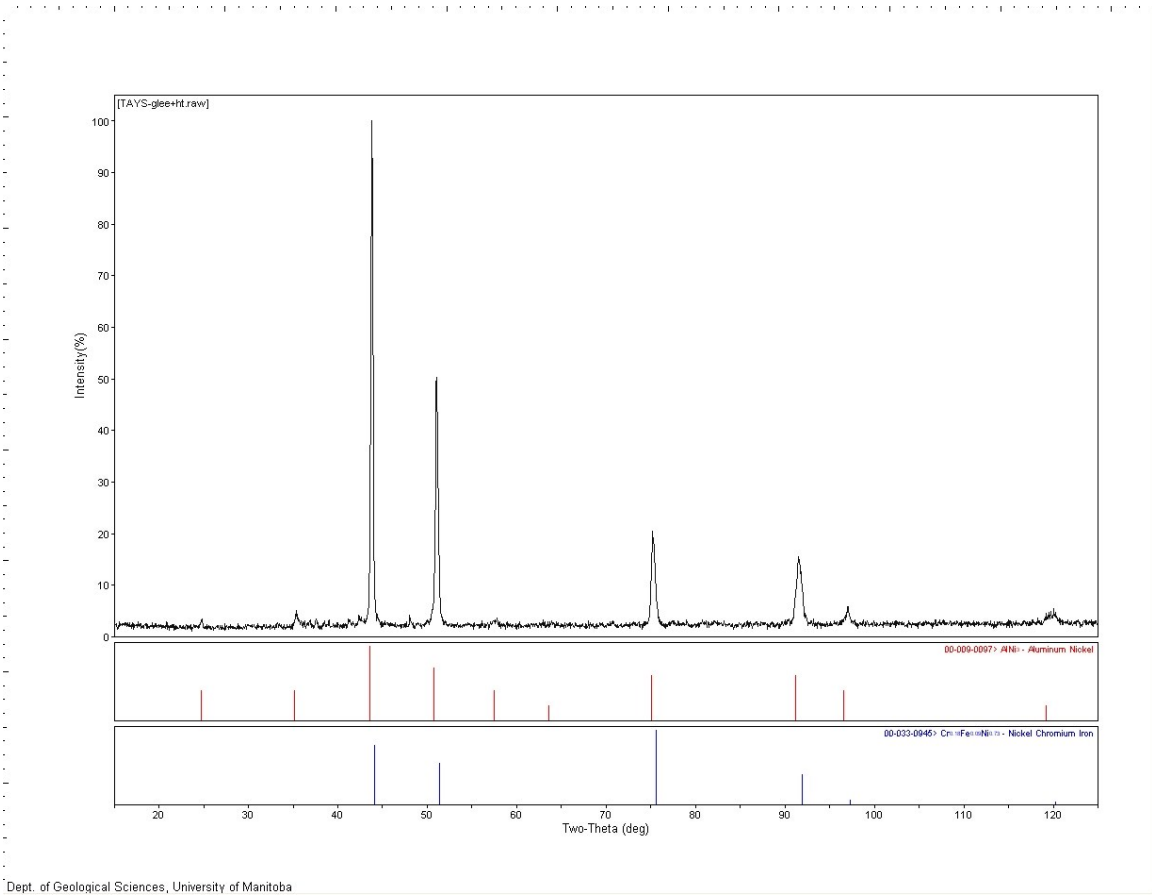


Figure A22- XRD spectrum for TAYS in the Gleebled, post heat treated condition

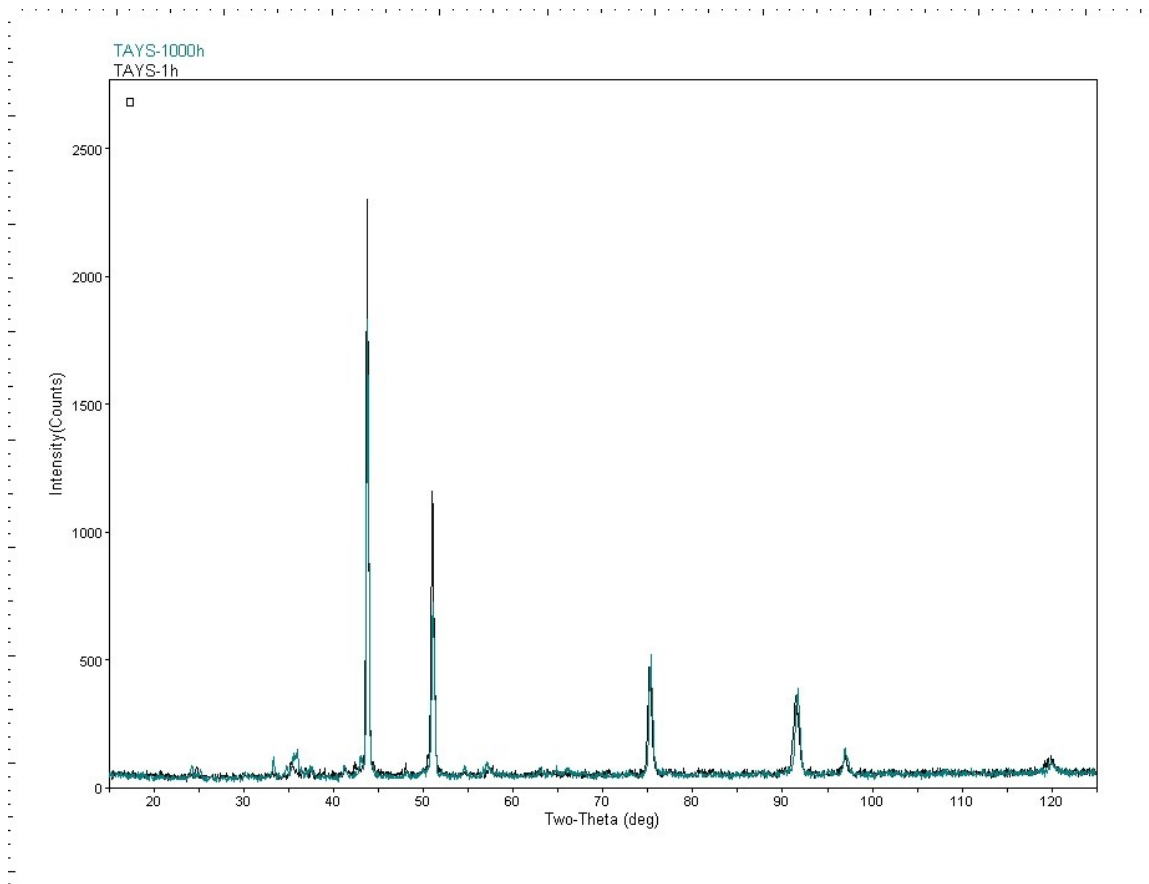


Figure A23 - XRD spectrum for TAYS oxidized for 1h and 1000h overlay

## APPENDIX B

August 13, 2012

Donald Clark Murray  
MAsc Student  
Process Engineering and Applied Science  
(Materials Engineering); Faculty of Engineering  
Dalhousie University  
1 204 998 2972  
dcmurray@dal.ca

Dear Mr. Murray,

With this letter, you are permitted to reprint the 3 figures listed below. The permission is granted for use in the THESIS/DISSERTATION/PRACTICUM titled "On Improving the Oxidation Resistance of a Nickel-Based Superalloy Produced by Powder Metallurgy.

Please give credit similar to as follows:

Source: Powder Metallurgy Science, 2nd Ed., German, Randall M., (1994)  
ISBN 1-878954-42-3 Metal Powder Industries Federation, 105 College Road East,  
Princeton, New Jersey, USA.

Thank you for your continued support of the powder metallurgy and particulate materials industries.

Sincerely,

James P. Adams  
Director, Technical Services

Requested figure

1. Page 101: Figure 3.16 A vertical gas atomizer 2. Page 168: Figure 5.10 A plot of fractional packing density versus composition for bimodal mixtures of large and small spheres 3. Page 245: Figure 7.4 The two sphere sintering model with the development of the interparticle bond during sintering